DESIGN AND CONTROL OF A SOFT ROBOTIC MANIPULATION SYSTEM FOR TRANSORAL LASER MICROSURGERY UNDER MAGNETIC RESONANCE IMAGING

by

Chow, Chun Kit

A thesis submitted in partial fulfillment of the requirements
for the Degree of Master of Philosophy
at The University of Hong Kong.

Aug 2018

Abstract of dissertation entitled

"**Design and Control of a Soft Robotic Manipulation System for Transoral Laser Microsurgery under Magnetic Resonance Imaging**"

Submitted by

CHOW Chun Kit

for the Degree of Master of Philosophy
at The University of Hong Kong
in Aug 2018

Nasopharyngeal cancer is relatively prevalent in Southeastern China such as Hong Kong. Effective treatment for head and neck cancers (HNCs) is of paramount importance. Traditional open incision approach causes trauma to the patient and induces long recovery time, whereas non-surgical chemoradiotherapy is toxic and degrades swallowing function. Therefore, alternative locoregional transoral therapy is vital for curing HNCs with the least post-surgical trauma and side effects. This thesis presents the design, optimization, fabrication and experimental validation of a magnetic resonance (MR) conditional reinforced soft robot (RSR) for transoral laser dissection. A world-first 3D-printed manipulator for MRI-guided laser surgery is fabricated by PolyJet™ printing technology (Stratasys Ltd., U.S.). Multi-printing technology allows seamless application of strain wrapping constraints to enhance robustness and controllability of RSR. Its miniature (Ø13 mm × 100 mm), compliance design enables RSR to operate within a confined oral, nasopharyngeal (ONP) cavity. This five degree-of-freedom (DoF) robotic system has kinematic redundancy to reach the same target via various paths. RSR is powered by a bio-compatible hydraulic fluid to minimize the hysteresis effect. Novel MR-based wireless tracking technique is adopted. Three miniaturized microcircuits are embedded in the patient-specific dental guard, which are tracked under MRI to provide a three-dimensional localization of the robotic system. MR-compatibility test has been done to demonstrate no observable image artifact during simultaneous robot motion. Pre-clinical validation has been conducted for the proposed 3D-printed robotic system to perform laser dissection task under MRI. Path-following tests have been performed in free space with an electromagnetic tracking system to evaluate its maneuverability. Sufficient accuracy and repeatability have been demonstrated for precise laser dissection task with mean errors of 0.1500 ± 0.0835 mm and 0.0446 ± 0.0082 mm respectively.

Word Count: 279 words

Unless the LORD builds the house,

  the builders labor in vain.

Unless the LORD watches over the city,

  the guards stand watch in vain.

<div align="right">(Psalm 127:1)</div>

Declaration

I declare that this dissertation represents my own work, except where the due acknowledgment is made, and that it has not been previously included in a thesis, dissertation or report submitted to this University or to any other institute for a degree, diploma or other qualification.

Signed …………………………………………...

CHOW Chun Kit

Acknowledgments

Along with the journey in my MPhil study, even though there are ups and downs, I still feel grateful that God have bought me grace to overcome all difficulties. Also, I have also gained such a valuable experience. I feel thankful to work and enjoy with researchers in this group. I would like to use this opportunity to also express my gratitude to the people who are supporting and encouraging me until now.

This work would not have started without the idea of Dr. Ka Wai Kwok. His brilliant and novel idea has inspired and motivated me to overcome all the technical barrier and mental impossibilities. He consistently steered me into a right direction and provided opinions whenever I got struck in a dead end. He always tries to pull me out of the problem with constructive solutions.

Also, I would like to thank Ziyan Guo, Ziyang Dong, and Kithang Lee for their valuable experience from their senior Ph.D. pursuit to assist my study. Moreover, I would like to thank my study partners Chimlee Cheung, Tim Lun, and Martin Leong for their companionship on this remarkable journey in my life.

Finally, I must express my very profound gratitude to my parents and my sister for providing me with monetary support and patience during the study period. This accomplishment would not have been possible without their unfailing support and continuous encouragement throughout the study. Thank you.

Marco Chow

Table of Contents

VI

List of Figures

XI

XII

List of Tables

List of Abbreviations

ASTM - American Society for Testing and Materials

CO$_2$ - Carbon dioxide

CRT - Concurrent Chemoradiotherapy

CT - Computed Tomography

CTx - Chemotherapy

cRSR - coarse Reinforced Soft Robot

cVAM - Cyclical Vacuum-Actuated Machine

DM - Digital Materials

DoF - Degree-of-Freedom

EBV - Epstein-Barr virus

EM - Electro-Magnetic

ENT - Ear, Nose, and Throat

EtO - Ethylene Oxide

EUA - Examination-Under-Anesthesia

FDA - Food and Drug Administration

FE - Finite Element

FEA - Finite Element Analysis

FDG - Fluorine-18-fluoro-Deoxy-Glucose

FK - Feyh-Kastenbauer

fMRI - functional Magnetic Resonance Imaging

fRSR - fine Reinforced Soft Robot

FSA - Frozen Section Analysis

FSE - Fast Spin Echo

FSPGR - Fast Spoiled Gradient Echo

GRIN - Gradient-index

GRE - Gradient Echo

HNCs - Head and Neck Cancers

HNSCC - Head and Neck Squamous Cell Carcinoma

HPV - Human Papillomavirus

iMRI - intraoperative Magnetic Resonance Imaging

LAA - Left Atrial Appendage

LARS - Larynx Advanced Retractor System

LITT - Laser-Induced Interstitial Thermotherapy

MR - Magnetic Resonance

MRI - Magnetic Resonance Imaging

MIS - Minimally-Invasive Surgery

NA - Numerical Aperture

NEMA - National Electrical Manufacturer's Association

NN - Neural Network

NOTES - Natural Orifice Transluminal Endoscopic Surgery

NPC - Naso-Pharyngeal Carcinoma

ONP - Oral and Naso-Pharyngeal

PD - Power Density

PET - Positron Emission Tomography

PRFS - Proton Resonance Frequency Shift

RF – Radio-Frequency

RMS - Root Mean Square

RT - Radiotherapy

RTV - Room Temperature Vulcanizing

RSR - Reinforced Soft Robotic

STIFF-FLOP - STIFFness controllable Flexible and Learnable manipulator for surgical Operations

STL – Stereo-Lithographic

SMA - Shape Memory Alloys

SNR - Signal-to-Noise ratio

TES - Transoral Endoscopic Surgery

TEVAR - Thoracic Endo-Vascular Aortic Repair

TIR - Total Internal Reflection

TLM - Transoral Laser Microsurgery

TORS - Transoral Robotic Surgery

UTS - Ultimate Tensile Stress

CHAPTER 1

INTRODUCTION

1.1 MOTIVATION AND OBJECTIVES

HEAD and neck cancers (HNCs) adversely affected more than 4.6 million people and resulted in more than 362,000 death cases around the globe in 2013. In Southeastern Asia such as Hong Kong, nasopharyngeal carcinoma is relatively prevalent, whereas oral, pharynx and larynx cancers are prevalent in the surrounding Asian countries. The traditional surgical open procedure caused trauma to the patient and induced a long recovery time. Therefore, developing an effective curing approach for HNCs is crucial for reducing post-surgical trauma and side effects.

Before 2009, most patients were treated with non-surgical radiotherapy (RT) [1]. RT targets the cancerous cells, but also kills the non-targeting tissues. Radiation toxicity adversely affects the non-cancerous tissue and degrades swallowing function. As a result, locoregional treatment is essential for effective HNCs' curing with least toxicity and post-treatment side effects. After 2009, transoral endoscopic

surgery (TES) arose as a minimally-invasive robotic surgical treatment in the form of transoral laser microsurgery (TLM) and transoral robotic surgery (TORS). Two TORS systems have gained the approval from U.S. Food and Drug Administration (FDA) since 2009. Traditional transoral laser with bulky micromanipulator can only access to the base of tongue. Nowadays, laser delivery methodology of TLM is advanced by the fiber laser technology. For instance, the flexible laser tip can navigate to the oral, nasopharyngeal (ONP) space guided by the TORS system. Meanwhile, TORS demands a large maneuvering workspace in the ONP cavity. As a result, a workspace enhancement is required and achieved by setting up a retraction system. However, this combined surgery induces a heavy dependence on the TORS system. Also, installation of retractor requires extended setup period up to one hour.

Typically, the surgeon performs a frozen section analysis (FSA) intraoperatively to determine the completion of cancerous cell resection. FSA is conducted with a two-level or three-level method concerning the number of cut on the frozen section specimen. During the surgical operation, FSA takes about 10 minutes for microscopic analysis. However, FSA can only evaluate the gross tumor volumes resected, instead of the unresected region in the ONP cavity. Given this, intraoperative imaging tools provide a real-time evaluation of tumor resection. Intraoperative magnetic resonance imaging (MRI) also offers additional MRI aids such as magnetic resonance (MR) thermometry. This thermal tracing technology can visualize the heat affected zone and the dissected depth of the tissue. MR thermometry is crucial in providing thermal feedback to track laser projection spot position during surgery. In this study, I aim to develop an MR-conditional surgical navigation system to manipulate the flexible laser collimator to perform locoregional laser dissection. This research can reduce cancer recurrence by accurately determining the extent of the cancerous dissected. As the current TORS contains ferromagnetic material in motors, they are infeasible to be used under MRI. In this research, I utilize the concept of soft robotics as the actuation modality to navigate and manipulate the flexible laser.

1.2 THESIS ORGANIZATION AND MAIN TECHNICAL CONTRIBUTIONS

The outline of this thesis is as follows. In **Chapter 2**, an overview of the current clinical background of HNCs is provided. Treatment modalities in terms of surgical and non-surgical approaches are compared. Technical challenge of transoral laser surgery is addressed. Various scanning modalities are outlined. The potential application of the MR-conditional robotic system is highlighted.

Chapter 3 evaluates the 3D reconstructed ONP space by cadaveric data and CT/MR images. Customized dental guard is fabricated according to the patient-specific dental features for MRI scan. ONP workspace for both closed-jaw and opened-jaw configuration are evaluated. Optical principles for laser delivery are investigated. Design specification and light converging properties of microlens are analyzed. Absorption efficiencies of various laser emission wavelengths are compared.

Chapter 4 reviews the current research on laser endoscope and soft robotic surgical endoscope. Soft robotic prototype is fabricated by room-temperature-vulcanizing (RTV) molding technique. Strain wrapping reinforcement in the soft robot is investigated. The maneuverability of the reinforced soft robot (RSR) is proved by following specific trajectories in an intracavitary space. The possibility of system miniaturization is examined with the assistant of the three-dimensional (3D) printing technology. Also, limitation of the 3D printing technology is addressed.

Chapter 5 discusses the integration of the overall MR-conditional robotic system. Design criteria of RSRs are optimized and studied by the finite element analysis (FEA) tools. The RSRs performances are evaluated by their robot rigidity and stability. Moreover, the advancement mechanism of the robotic system is designed. Various types of actuation fluids and actuation setups are also compared. Workspace evaluation is performed by the electromagnetic (EM) tracking system. Kinematic parameters of the soft robotic system are estimated.

Chapter 6 covers the control methodology by using a neural network (NN). Accuracy and reliability of RSRs are evaluated. MR-compatibility is evaluated by the signal-to-noise ratio (SNR) as an indication index. Laser dissection task is performed in MRI. Limitation and future work are discussed.

1.3 PUBLICATIONS IN STUDY PERIOD

1) <u>Marco C.K. Chow</u>, Ziyan Guo, Chim Lee Cheung, and Ka-Wai Kwok "*Soft Robotic Manipulator for Intraoperative MRI-guide Transoral Laser Dissection.*", in **Soft Robotics (SoRo)**, 2018 (in preparation)

2) S. Fan, A. Chan, S. Au, M. C.-W. Leong, <u>Marco C.K. Chow</u>, Y.T. Fan, R. Wong, S. Chan, S.K. Ng, A. P. Lee, and Ka-Wai Kwok. "*Personalised anesthesia: three-dimensional printing of facial prosthetic for facial deformity with a difficult airway.*", in **British Journal of Anaesthesia**, 2018.

3) Kit-Hang Lee, Denny K.C. Fu, Martin C.W. Leong, <u>Marco C.K. Chow</u>, Hing-Choi Fu, Kaspar Althoefer, K.Y. Sze, Chung-Kwong Yeung, and Ka-Wai Kwok "*Nonparametric Online Learning for Hyper-Elastic Robotic Control: An Enabling Technique for Effective Endoscopic Navigation.*", in **Soft Robotics (SoRo)**, vol. 4, no. 4, pp. 324-337, 2017.

4) Kit-Hang Lee, Martin C.W. Leong, <u>Marco C.K. Chow</u>, Hing-Choi Fu, Wayne Luk, Kam-Yim Sze, Chung-Kwong Yeung, and Ka-Wai Kwok. "*FEM-based soft robotic control framework for intracavitary navigation.*", in **IEEE International Conference on Real-time Computing and Robotics (RCAR)**, pp. 11-16., 2017
    Best Conference Paper Award

CHAPTER 2

TREATMENT MODALITIES FOR

HEAD AND NECK CANCERS

2.1 INTRODUCTION

HEAD and neck cancers (HNCs) invade all around the globe. HNCs adversely affected more than 4.6 million people and resulted in more than 362,000 death cases in 2013 [2]. Head and neck squamous cell carcinoma (HNSCC) accounted for more than 90% of the HNCs [3]. HNSCC is the 6th most common cancers worldwide and the 3rd most common cancers in developing countries. HNSCC has incidences of more than 30 per 100,000 population in France, in India (oral cancer), and Hong Kong (nasopharyngeal cancer) [3].

HNCs is a general description for a group of cancers in head and neck. It is categorized by its initial anatomic growth site. Typical HNCs' sites are paranasal sinuses, nasal cavity, oral cavity, salivary glands, pharynx, and larynx (**Fig 2.1**). For example, oral cancer describes the growth of cancerous tissue in the salivary gland, the base of tongue, tonsil, and oropharynx. Particularly in Hong Kong, 3.8% of the cancers' occurrence is due to nasopharynx cancer [4]. Also, nasopharynx cancer and other HNCs (such as lip, oral cavity, and pharyngeal cancer) also accounted for the 6th and 10th common cancer among male [4].
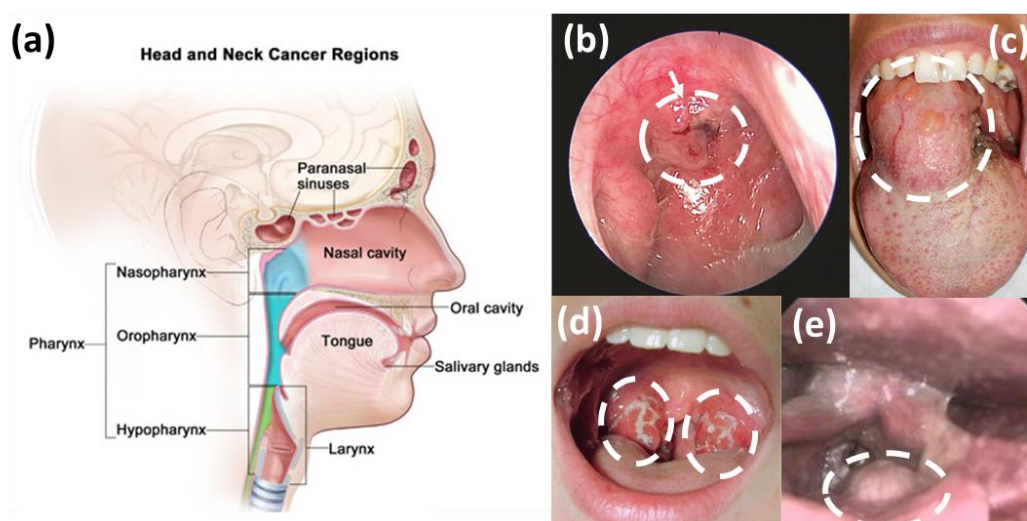
Fig 2.1   HNCs classification by cancer growing site. **(a)** Anatomy of oral, nasopharyngeal (ONP) cavity showing potential cancer growth region. Endoscopic view of four classes of HNCs, namely **(b)** nasopharyngeal cancer in upper nasopharynx, **(c)** oral cancer inside base of tongue, **(d)** pharynx cancer in tonsil wall, and **(e)** larynx cancer near vocal cords. **Image Source: [5], Terese Winslow LLC, and Physician 360**

2.1.1 Global Prevalence of Head and Neck Cancers

International Journal of Cancer categorized HNCs into four primary classes, namely **(i)** oral cancer, **(ii)** nasopharyngeal cancer, **(iii)** larynx cancer, and **(iv)** other pharynx cancers [6]. From the statistics from GLOBOCAN 2012, oral cancer had the highest cancer cases (44%) (**Fig 2.2a**) and the highest cancer death rate (38%) among HNCs worldwide (**Fig 2.2b**) [7]. Oral cancer is a global concern among HNCs. Meanwhile, nasopharyngeal carcinoma is uncommon (i.e., < 1 case per 100,000) in the United States and most other nations. However, it is found that nasopharyngeal cancer is prevalent (i.e., 22 cases per 100,000) in Hong Kong. Given this, the following research will compare the prevalence of HNCs localized in Asia.

Estimated NEW CANCER CASES of HNCs

Oral Cancer
44%

Larynx
23%

Other Pharynx Cancer
21%

Nasopharyngeal
Cancer
12%
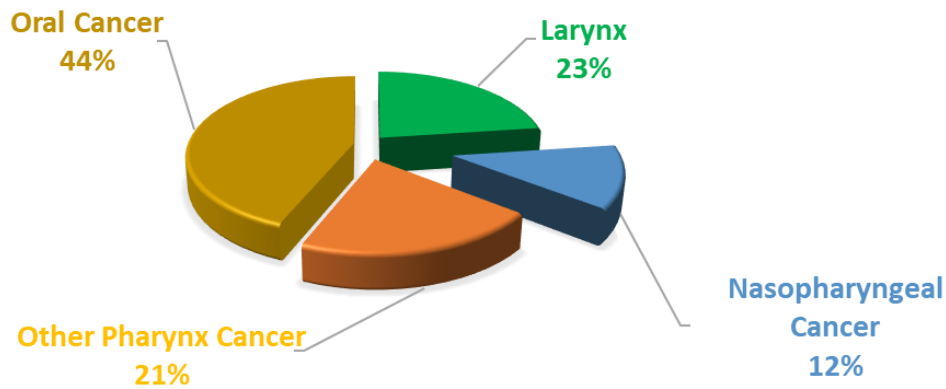
(b)

Estimated CANCER DEATH of HNCs

Oral Cancer
38%

Larynx
22%

Other Pharynx Cancer
26%

Nasopharyngeal
Cancer
14%
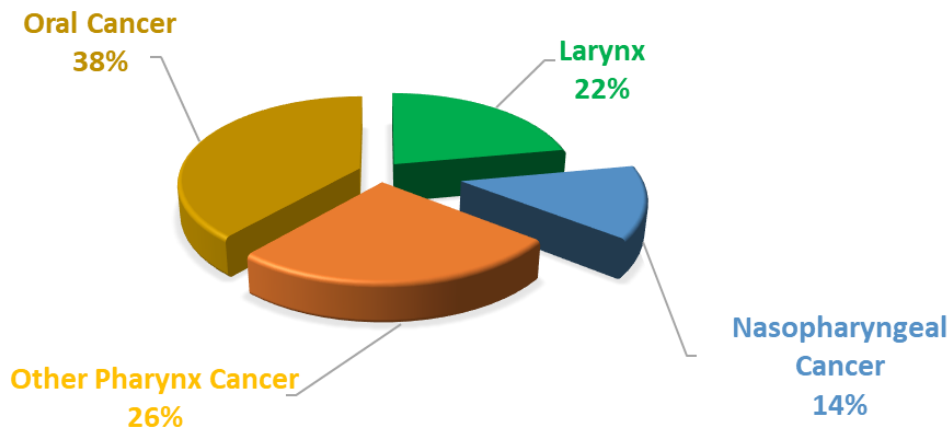
Fig 2.2   Global cancer incidence and death of HNCs in GLOBOCAN 2012. **(a)** Estimated new HNC cases showing the highest cancer incidence for oral cancer (44%). **(b)** Estimated HNC death rate showing the highest cancer death for oral cancer (38%). **Data Source: GLOBOCAN 2012**

According to Cancer Today, the relative incidence rate of the four categorized HNCs in Asia are plotted [8]. **Fig 2.3** shows that nasopharyngeal cancer has a relatively high prevalence in China, but other cancers have not. For instance, nasopharyngeal carcinoma caused comparatively high incidence rates in Eastern Asia including Guangdong and Hong Kong [3, 9]. Contrarily, oral cancer is predominant in Southern Asia countries such as India, Pakistan [10]. To conclude, it is observed that there is a high incidence rate of nasopharyngeal cancer in localized China and oral cancer worldwide. With the high prevalence of oral and

nasopharyngeal cancers, much research needed to be done regarding the etiology and treatment. In **Section 2.1.2**, we will focus on the risk factors of the oral and nasopharyngeal carcinomas.
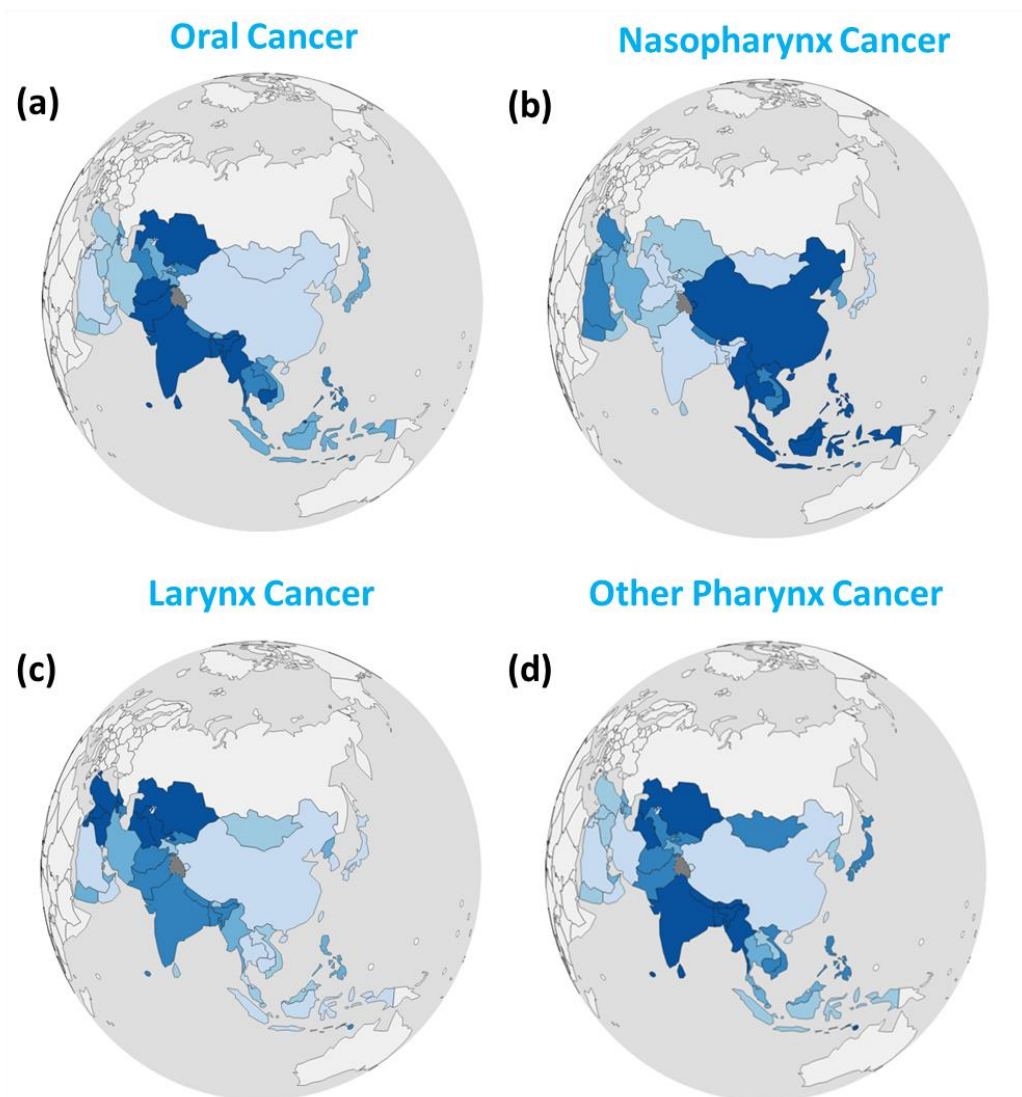
Fig 2.3   Relative prevalence of HNCs in sub-regions of Asia. Age-standardized rates (ASR) incidence cases are listed by four classes of HNCs of: **(a)** oral cancer, **(b)** nasopharynx cancer, **(c)** larynx cancer, and **(d)** other pharynx cancers. Nasopharynx cancer shows a relatively high prevalence in Southeastern Asia. Incidence of oral, larynx and other pharynx cancers are more prevalent in Southern Asia and Central Asia. **Image Source: Cancer Today**

2.1.2 General Risk Factors for HNCs

Risk factors for HNCs are related to three intake habits, namely alcohol, tobacco and chewing tobacco. These habits are three major factors for HNCs [9, 11]. In this section, three intake habits will first be discussed. Then, other virus-associated risk factors will be mentioned.

Over 75% of the diagnosed HNCs are tobacco smokers [12], whereas about 33% of deaths are accounted by alcohol use. It is found that tobacco use alone is the leading cause of HNCs. Worse still, when the use of tobacco is combined with frequent alcohol consumption, two risk factors act as a synergy effect and increase the chance of having HNCs [13, 14]. Tobacco use includes both smoking habit and smokeless tobacco named chewing tobacco. In Southeastern Asia, there is a cultural tradition called "betel quid chewing", which is a carcinogenic habit. This chewing tobacco habit also contributed to the occurrence of oral cancer [9]. Since 1980, the incidence of oral cancer in men has tripled due to "betel quid chewing" in Taiwan and China [15]. Apart from tobacco or alcohol-related factors, diet habit also acted as a risk factor for nasopharyngeal carcinoma (NPC). Studies have reported salted fish, and certain preserved foods increased risks for NPC [16].

Apart from the risk factors by food intake habit, there are also risk factors related to viruses. Oral cancer has a risk factor associated with human papillomavirus (HPV) infection [17]. 80% of oral cancer in the base of tongue were HPV-positive and proved the potential harm of HPV towards oral cancer [18]. It is also found that incidence rates for HPV-related oral cancer were increasing in some European countries, which is believed to be associated with the changing oral sexual behavior in those countries [19]. In contrary, NPC is related to another virus called Epstein-Barr virus (EBV). EBV is linked to the progression of NPC, as the EBV-infected population has increased the risk of NPC occurrence. With numerous risk factors overwhelming the community, effective treatment modality is of paramount importance for curing HNCs. In the upcoming sections, we will discuss the treatment modalities for both surgical and non-surgical.

9

2.2 NON-SURGICAL TREATMENTS FOR HNCS

Before the 21st century, three types of treatment methods were employed to tackle HNCs, namely radiotherapy (RT), chemotherapy (CTx), and open surgery [20]. Deployment of treatment modality is determined by the severity of cancer. The cancer severity is classified by stages and evaluated by the degree of metastasis to the adjacent organs, tissues, and lymphoid nodes. In early stage (T1-T2) of HNCs without metastasis, patients are treated with surgery [21]. However, patients having metastasis or large tumor are often treated with surgical therapy in conjunction with chemoradiation therapy (CRT). In the following review, we will focus the cases without metastasis, mainly in T1/T2 with tumor size of less than 3 cm.

2.2.1 Radiotherapy and Chemotherapy

RT is commonly used for HNCs treatment to control and kill malignant cells by ionizing radiation. Since the 1920s, RT was employed for curing HNCs by the use of X-ray and radium bromide [22]. During World War II in 1942, CTx was invented for lymphoma treatment and suppressed cancer temporarily [23]. After declassification of World War II documents, researchers converged the treatment experiences and developed the first CTx drug to treat cancer [24]. In 1991, CTx was combined with RT to perform concurrent CRT. This combined therapy strategizes for organ preservation to retain speech and swallowing function. CRT provides a substantial and statistical improvement than solely RT or CTx regarding locoregional control and survival rate. However, RT, CTx, and CRT exhibit side effects that affect peripheral non-targeted cells and organs including mucositis, dysphagia, neutropenia, nephrotoxicity, neurotoxicity, ototoxicity, xerostomia, fibrosis, trismus and osteoradionecrosis [25]. These treatment modalities result in inherent morbidity and toxicity after treatment [20]. Also, intensive CRT leaves poor swallowing function to the patient. Patients with intensive CRT treatment need to rely on the gastrostomy tube, even though the organ is preserved [26]. Worse still, resistance RT [27], CTx [28], and also CRT [29] are developing for HNCs. Therefore, alternative locoregional treatment, other than RT, CTx, and CRT, is essential for effective curing of HNCs in the future.

From non-surgical approach to surgical procedures, the origination of treatment modalities are listed in **Fig 2.4**. This timeline shows non-surgical procedure (RT and CTx) started at the 1920s. Even though the development of open surgery was immature in the 20th century, surgical modality began in 1895, which is originated earlier than the non-surgical approaches. With the technological advancement in the development of surgical robot since 2009, transoral robotic surgery (TORS) and transoral laser microsurgery (TLM) were introduced, both of which gained the approval from the U.S. Food and Drug Administration (FDA). From that time, the treatment preference started to shift from the non-surgical therapies back to the surgical approach. The benefits of the latest surgical systems are non-invasiveness to the patient and locoregional tumor resection. In **Section 2.3**, the upsides and downsides of the traditional open surgical approach will be evaluated. Moreover, the advantage and limitations of TORS and TLM will also be discussed.
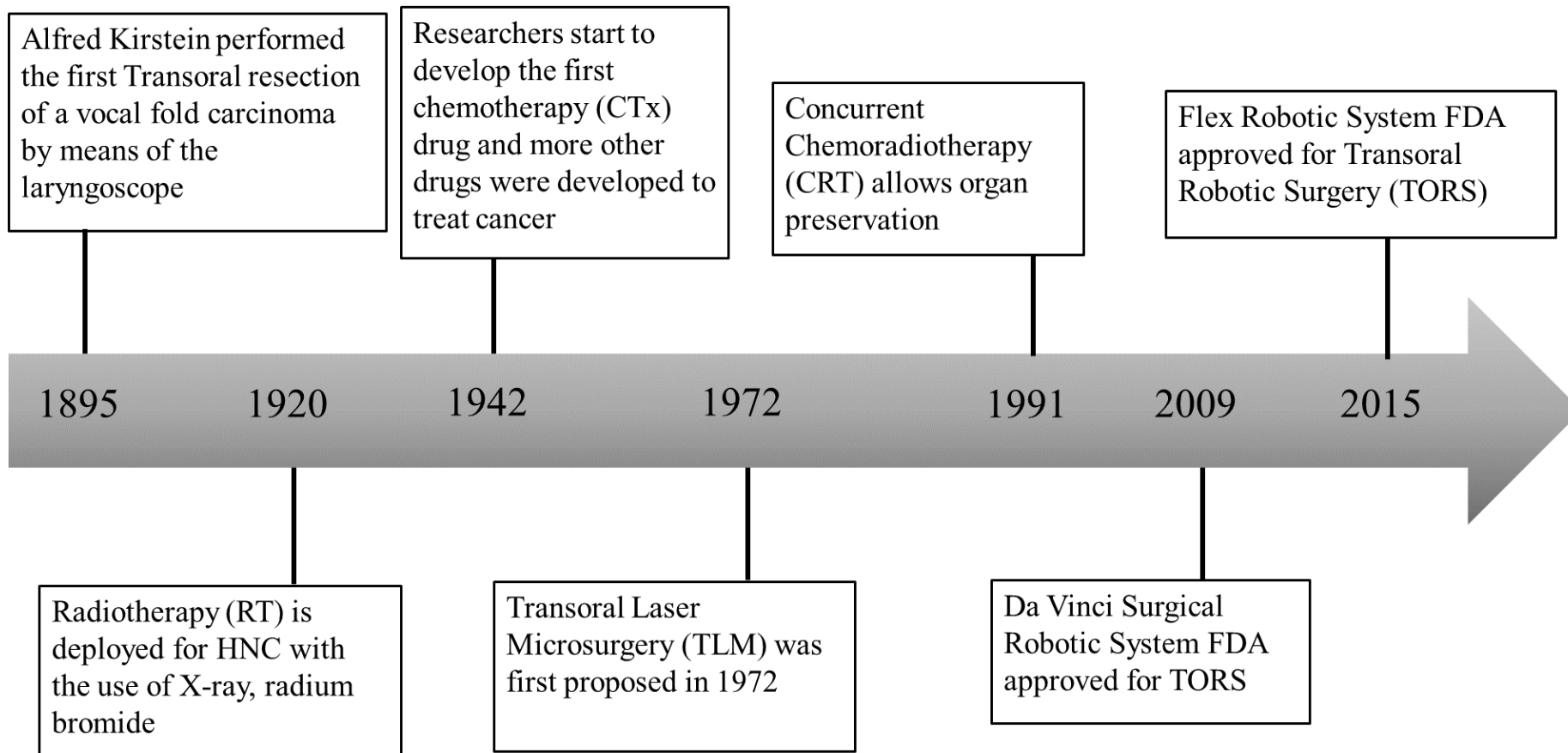
Fig 2.4 Timeline of treatment modalities dealing with HNCs. First transoral treatment started by open surgery in 1895. Invasive open surgery was then replaced by non-surgical treatment of RT, CTx, and CRT. Advancement of TLM and TORS shows adoption of surgical approach after 2009.

2.3 SURGICAL TREATMENTS FOR HNCS

In the 2000s, statistics showed the 5-year survival rate for RT, CRT, and surgery were 43.48%, 54.63% and 63.95% respectively [30]. The highest 5-year survival rate of surgical treatment is observed by comparing to CRT and RT. Therefore, with the advancement of robotic surgical systems, the best option for curing HNCs is to locally remove the tumor by surgery. The genesis of the surgical approaches dated back to 1895. Surgical treatments were started by the open surgery. Before the 20th century, surgeons employed open incision approaches to visualize the tumor and peripheral tissues. For the open procedures, it created a long face or neck incision [31]. In 1906, 132 operations were performed for radical neck dissection (**Fig 2.5a**) [32]. However, long recovery time was induced due to a large incision after surgery. After that, surgical approaches were aimed for a small incision. In addition, natural orifice transluminal endoscopic surgery (NOTES) was developed, which causes minimal invasion to the patient. In 1895, Alfred Kirstein performed the first transoral cancer resection in the vocal fold. He used a self-developed laryngoscope that allows direct vision to larynx [20]. This non-incision approach for diagnosing and curing transoral diseases opened a new page of transoral endoscopic surgery (TES).
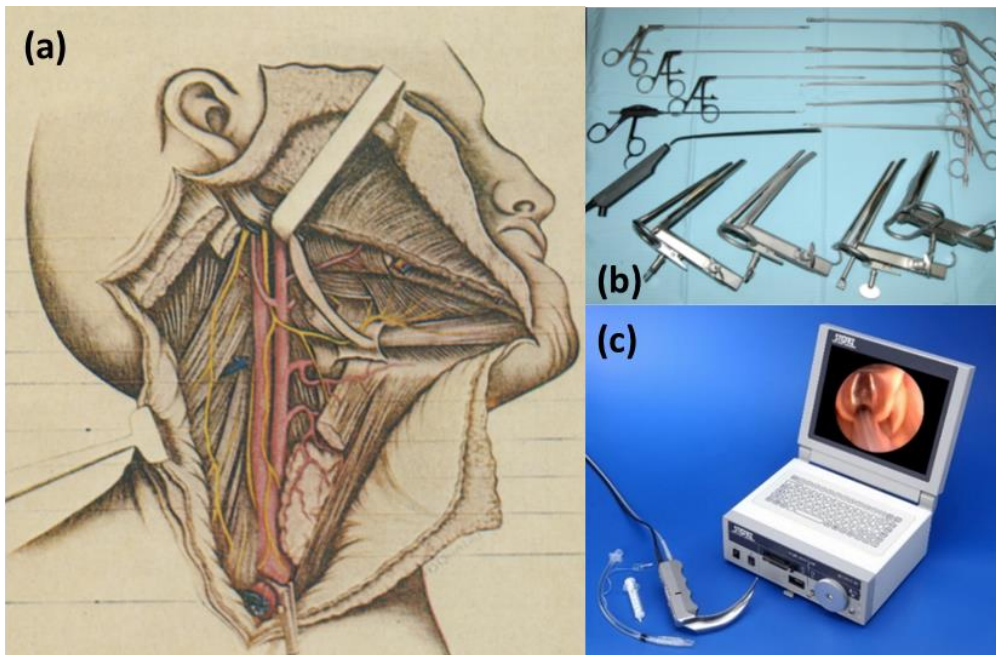
Fig 2.5   Conventional and current surgical approaches for HNCs' curing. **(a)** Radical neck dissection for open approach surgery. Laryngoscopes are used for minimal invasive TES. **(b)** Distending operating laryngoscope of various sizes. **(c)** KARL STORZ video laryngoscope equipped with an endoscopic camera. **Image Source: [33], KARL STORZ Endoscopy Ltd.**

In the early 1900s, laryngoscopy was improved with a bent distending laryngoscope (**Fig 2.5b-c**). Nowadays, TES is not limited to laryngoscopy but also includes TLM and TORS. TES is a minimally-invasive surgery (MIS) without an external incision. Also, TES results in little or no change in speech, appearance and swallowing function. Therefore, TES reduces recovery time, pain level and cancer reoccurrence compared to the traditional open approach. In some cases, TES even eliminates postoperative RT or CTx.

With the emerging technology of carbon dioxide (CO_2) laser for tumor laser surgery, TLM has been widely accepted for HNCs' curing. TLM can create precise margin and depth control by manipulating the microscopic magnification and laser power intensity [21]. TLM enables locoregional dissection without affecting the peripheral tissues. By the acceptance of robotic surgery from the public and U.S. FDA, TORS is also adopted as a kind of TES. TORS improves the quality of life after surgery and decreases cosmetic disfigurement. Both TLM and TORS will be discussed in the following sections, regarding their development histories and current capabilities.

2.3.1 Transoral Laser Microsurgery

In 1972, TLM was pioneered as a treatment approach for laryngeal pathology. Nowadays, TLM is widely adopted for tumor resection in the throat and larynx by its precise margin control and minimal thermal damage. TLM has several advantages over traditional open surgery. For example, TLM can: **(i)** avoid of use for tracheostomy, **(ii)** prevent pharynx cutaneous fistulas, **(iii)** cause lower postoperative morbidity [34], and **(iv)** result in better preservation of swallowing function [35]. After deploying general anesthesia to patients, the laser is guided by micromanipulator enters via the natural orifice to the oropharyngeal [36] and laryngeal space [34, 37]. This minimally-invasive microsurgery is performed without external incisions. Unlike conventional resection approach using scalpels, TLM dissipates radiant energy to the water-contained tissue to vaporize the benign and malignant cells. Moreover, laser dissection approach offers an additional ability of hemostasis than the scalpels. Currently, there are two kinds of thermal dissection

modalities: **(i)** laser-assisted and **(ii)** diathermy-assisted. Research has compared both modalities and found that laser-based dissection is more reliable regarding to the thermal damage and post-surgical trauma [38]. With a controllable thermal power output of laser, the surgeon can input various laser patterns and penetration depths to the TLM medical console, causing the laser procedure to perform automatically.

2.3.1.1 Growth of medical laser for tissue dissection

Advancement in laser technology led to the growth of various laser applications in the late 1990s. Nowadays, there is a wide range of laser usage with high power output ($P > 100$ W), such as material processing, spectroscopy, and even directed-energy weapon. Alternatively, medical laser and dental laser require less energy output ($P < 60$ W) (**Fig 2.6**). The abovementioned lasers are Class IV lasers ($P > 500$ mW) that can cause burning effect or permanent eye damage via direct or indirect beam viewing.
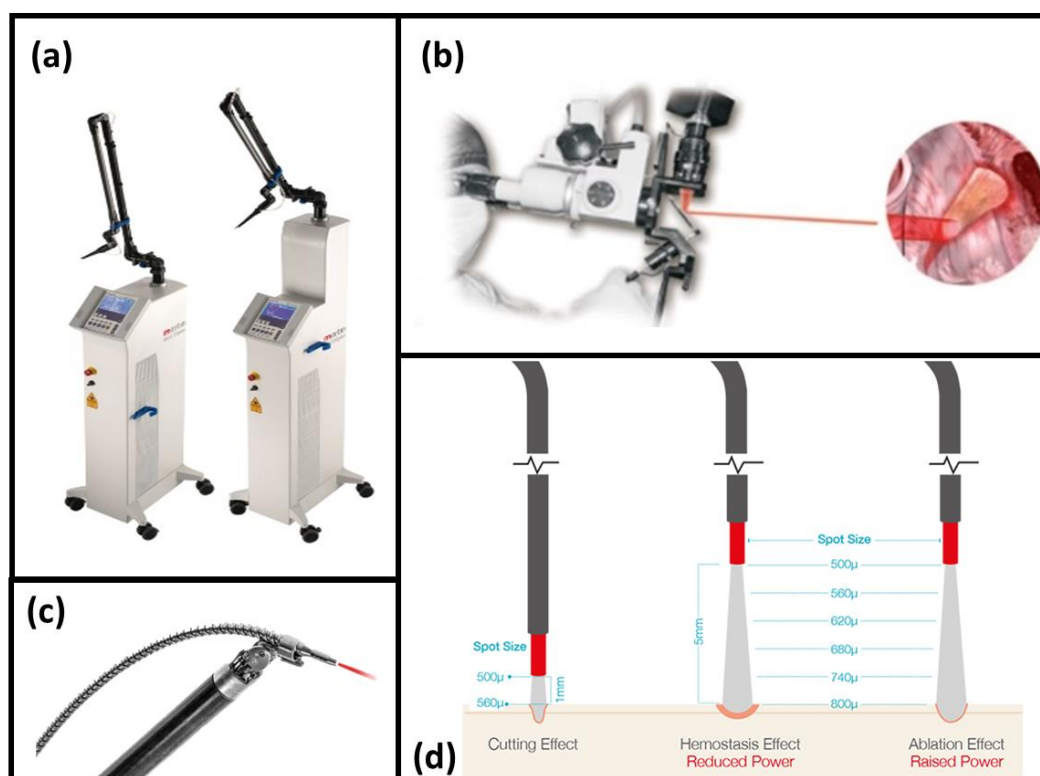
Fig 2.6 Example of transoral medical lasers for tissue dissection: **(a)** MCO 25plus/50plus CO2 lasers manufactured by KLS Martin. **(b)** Laser beam deflected by rigid micromanipulator projecting to cancerous tissues. **(c)** Flexible laser fiber system (AcuPulse 40WG, Lumenis) transmitting laser power with less bulky setup. **(d)** Various distance from tissue resulting in cutting, hemostasis, and ablation effect. **Image Source: Lumenis Ltd.**

Typical dental lasers are gas lasers, dye lasers, and solid-state lasers. They are differed by their active laser medium. Laser targeting task is controlled by the micromanipulator (**Fig 2.6b**), whereas the real-time visual field is captured by an operating microscope. The micromanipulator allows precise tissue dissection with various patterns such as line, circle, square and ellipse. Given that water is homogeneously abundant within human tissues, it is assumed that the target chromophores in the transoral cavity are mainly water. Effective vaporization of water causes dissection of body cell. The most sensitive absorption band of liquid water is ranging from 2 µm to 10 µm (**Fig 2.7**) [39].
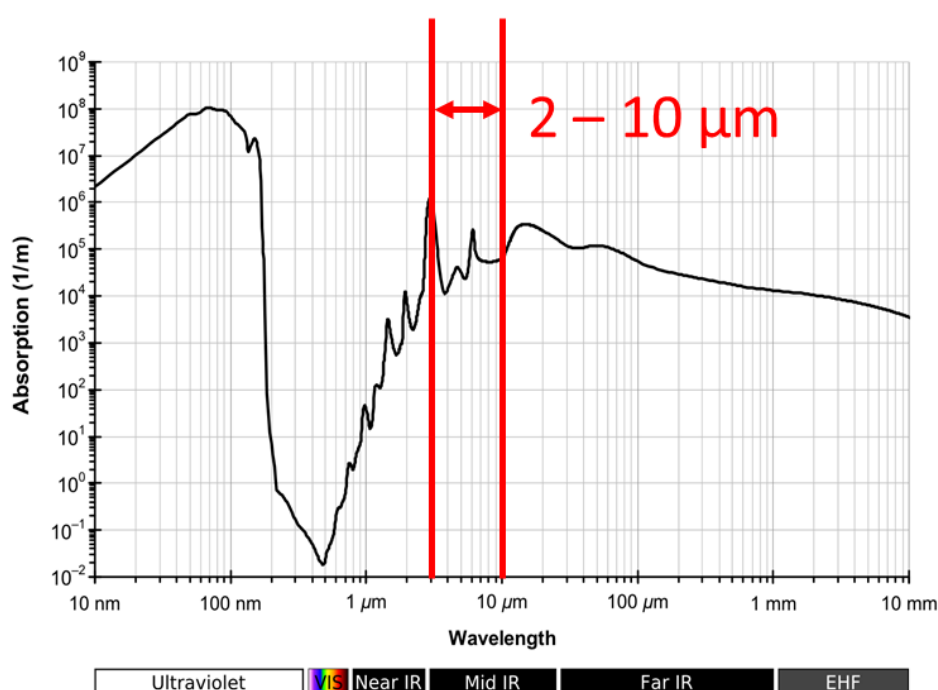
Fig 2.7   Absorption efficiency of liquid water of various wavelengths from ultraviolet (UV) to extremely high frequency (EHF). Sensitive absorption band of infrared (IR) for liquid water appeared in 2 - 10 µm. **Image Source: [39]**

This sensitive band in the water molecule is accounted by three O-H bonding configurations, which are O-H asymmetric stretching (2.662 µm), O-H symmetric stretching (2.734 µm), and H-O-H bending (6.269 µm). As a result, emission wavelengths of the TLM medical lasers are close to the absorption band in liquid water. Commercial laser devices for TLM are listed in **Table 2.1**. For example, thulium laser (Tm:YAG laser, 1.9 µm), holmium laser (Ho:YAG laser, 2.1 µm), and carbon dioxide laser (CO_2 laser, 10.6 µm) have emission wavelengths in a range of 2 µm to 10 µm. In addition, CO_2 laser and thulium laser are commonly adapted

in TLM regarding their hemostasis abilities. Two types of TLM laser are categorized by the means of laser delivery:

(i)   **Type I** – Laser controlled by micromanipulators

(ii)   **Type II** - Flexible laser navigated by robotic systems

Table 2.1   Commercial laser device for transoral surgery, varied by the emission wavelengths and laser power

Product Name	Type of Laser	Detail
Type I - Laser with Micromanipulator		
Digital AcuBlade, Lumenis (Tel Aviv, Israel)	CO_2 laser, 10.6 µm	Laser power: 0 - 60W
SoftScan, KLS Martin (Jacksonville, FL)	CO_2 laser, 10.6 µm	Laser power: 2 - 50 W
HiScan, DEKA Laser (Manchester, NH)	CO_2 laser, 10.6 µm	Laser power: 1 - 50 W
Type II - Flexible Fiber Laser		
AcuPulse 40WG, Lumenis [a] (Tel Aviv, Israel)	CO_2 laser fiber, 10.6 µm	Up to 40 Watt
OmniGuide [b] (Boston, MA)	CO_2 laser fiber, 10.6 µm	Up to 50 Watt
Revolix JR, LISA Laser [b] (USA)	Tm:YAG laser fiber, 1.94 µm	Up to 50 Watt
VersaPulse®, Lumenis (Tel Aviv, Israel)	Ho:YAG laser fiber, 2.1 µm	Up to 60 Watt

Note: [a] Cooperated with **Flex® Robotic System**

[b] Cooperated with **da Vinci® Surgical System**

The CO_2 laser system is widely adopted for TLM for its high efficiency in water extinction. 99% of the absorbed energies are dissipated to vaporize water and tissues. Also, high water absorption efficiency for CO_2 laser also results in limited penetration effect and minimal collateral thermal damages. This helps to protect peripheral tissues from injury, which is essential for the preservation of speech and swallowing function. Type I laser could only reach the base of tongue [40] but not pharynx area. It is due to the hindrance of micromanipulator and disability of laser steering after laser projection. Given this, CO_2 fiber laser [41] is invented to enable CO_2 laser to reach intracavitary area such as pharynx. The CO_2 fiber laser is a hollow-core photonic bandgap optical fiber. Compared to the Type I laser, the flexibility of the Type II laser allows to position the laser tip close to the target cancer tissues. These laser fibers require a navigation system such as an endoscope or a TORS. Type II laser enables to vary the angle of attack near the cancerous target, leading to optimal tissue dissection effect. Traditionally, only the base of tongue could be reached by TLM. With flexible fiber technology, TLM can now reach ONP cavity or even larynx without distending laryngoscope.

Another laser choice is the 2-µm lasers, which are thulium (Tm:YAG) laser and holmium (Ho:YAG) laser. They are deployed when the surgeon determined the site has a high risk of bleeding, as 2-µm lasers have a significant hemostasis effect [42]. Both 2-µm lasers perform precise dissection control as the maximum penetration depth are limited to 500 µm (i.e., 200 µm for thulium laser and 400 µm for holmium laser) [43]. Similar to CO_2 fiber laser, thulium and holmium fiber laser can also deliver laser energy via flexible laser fiber. Fiber lasers for the 2-µm lasers are more versatile to bend through the oropharynx [44] by its low bending radius of 25 mm. Integrating the versatility of flexible laser in TLM and accessibility of TORS, the above-mentioned limitation of system hindrance is overcame. This enables the transoral laser to reach pharynx area or even upper gastrointestinal tract. Two FDA-approved TORS, Flex® Robotic System and the da Vinci® Surgical System will be introduced in **Section 2.3.2**.

2.3.1.2   The requirement for power delivery

Quantification of an appropriate amount of energy is required to optimally induce vaporization on tumor cells with minimal incision diameter. This calculation of laser magnitude is defined by the power density PD. The correlation formula of PD is shown in **Equation 2.1**:

$$PD = \frac{P_{avg}}{A} = \frac{4P_{avg}}{\pi d_{spot}^2} \tag{2.1}$$

where P_{avg} is the average output laser power, d_{spot} is the projected laser spot diameter on the tissue surface, and PD has a unit of W/mm^2. For a constant power output, it shows that increasing target spot diameter d_{spot} will defocus the laser beam and reduce the resulting PD. PD is essential for clinicians to determine an appropriate power output with a specified laser spot diameter. The amount of energy delivered in a pulse duration of t_{exp} is defined as the energy density U (J/mm^2).

$$U = \int_0^{t_{exp}} PD \ s(t)dt \tag{2.2}$$

where $s(t)$ is a function of time representing the delivery pulse sequence. Pulse sequence varies from continuous wave (CW) to pulse-modulated sequence. PD provides a reference for the surgeon with the corresponding laser effect. The level of PD and the corresponding impact on tissues are listed in **Table 2.2**.

Table 2.2   Laser PD with its corresponding tissue effect [45]

Power density (*PD*)	Effect on tissues
0 - 500	Heating
500 - 1,500	Contracture, denaturing
1,500 - 5,000	Ablation (partial vaporization)
5,000 - 20,000	Incision (complete vaporization)
20,000 - 100,000	Rapid deep incision

2.3.2 Transoral Robotic Surgery

TES, such as laryngoscopy and TLM with a micromanipulator, possesses pre-defined curvature and fixed configuration. Contrarily, TORS consists of continuum manipulators that can be bent to perform tumor dissection. TORS enters by the natural orifice (i.e., mouth) to reach beyond the base of tongue, such as nasopharyngeal [46] and para-pharyngeal space [47]. With the mechanical retracting systems, the maneuvering space is maximized for surgical robots. Currently, two transoral surgical robot systems have passed U.S. FDA, which are the da Vinci® Surgical System and Flex® Robotic System.

2.3.2.1   da Vinci® Surgical System

Nowadays, the da Vinci® Surgical System (Intuitive Surgical Inc., Sunnyvale, CA, USA) is being employed in a wide range of surgical procedures (**Fig 2.8a**), such as cardiac, colorectal, thoracic, urologic, gynecologic surgeries. The da Vinci® Surgical System has four robotic arms. Three of these robotic arms manipulate Endowrist surgical instruments, and the remaining arm holds a high-definition endoscopic camera for visualizing 3D anatomy. The da Vinci® S and Si systems have been widely utilized for MIS. In December 2009, the U.S. FDA approved the da Vinci® Surgical Systems for T1/T2 transoral tumor resection [48]. However, the da Vinci® Surgical System consists of rigid links and articulated robotic arms [49]. Therefore, it requires a large maneuvering space for operating the surgical instruments. Given this, a Larynx Advanced Retractor System (LARS) is installed before the surgery. LARS installation includes the retraction of soft palate and stitching of tonsil pillar [50]. This setup process is time-consuming which takes about one hour. Some Type II lasers are integrated into the TORS system to reach intracavitary areas. For example, LISA Laser (thulium laser, USA) and OmniGuide (CO_2 laser, Boston, MA) are Type II fiber lasers guided by the TORS system. This combination of TLM and TORS starts to become a new trend for transoral tumor dissection. However, high setup and operation cost of the da Vinci® Surgical System makes it not readily accessible to all hospital and hence patients.
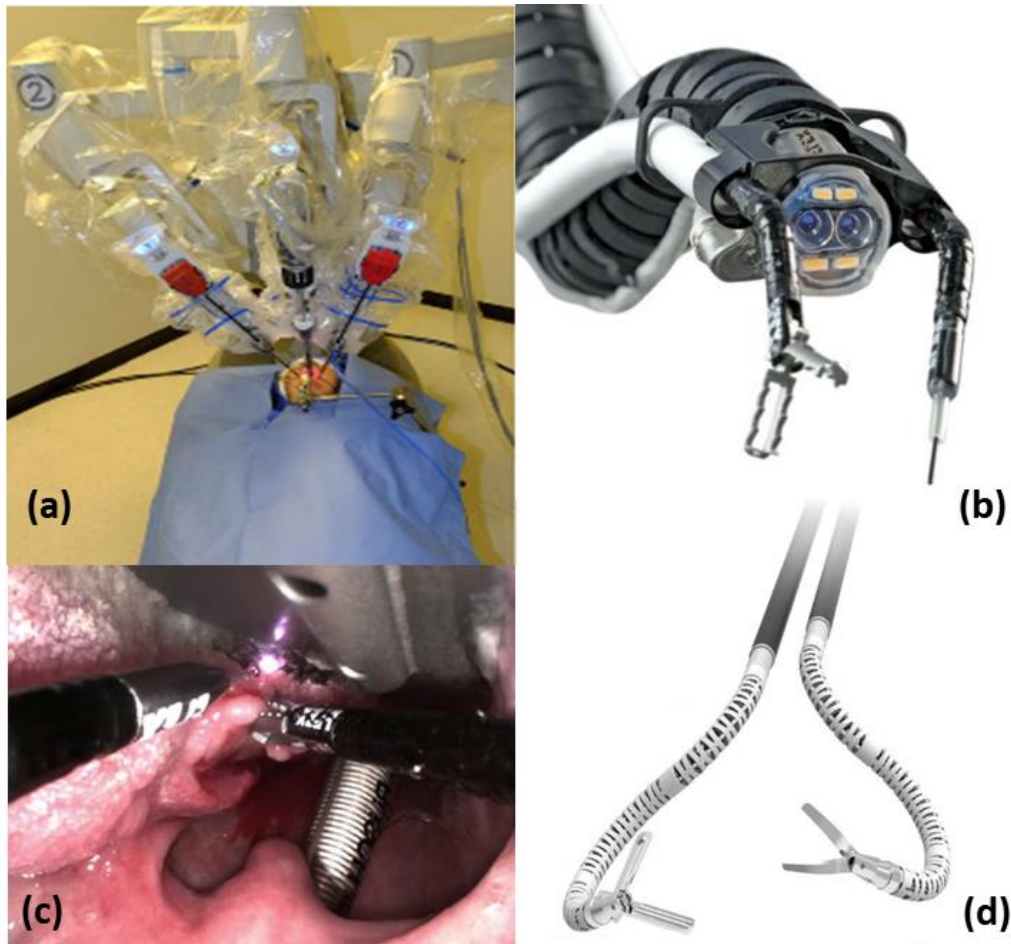
Fig 2.8   Transoral robotic system available in medical market. **(a)** da Vinci® Surgical System with triple 7-DoF robotic arms. **(b)** Flex® Robotic System equipped with video camera, graspers and monopolar cutters at the distal tip. **(c)** Flex® Robotic System performing laser cutting procedure. **(d)** Upcoming TORS system of Titan Medical SPORT surgical system. **Image Source: Intuitive Surgical Inc., Medrobotics® Corporation, Titan Medical Inc.**

2.3.2.2   Flex® Robotic System

In July 2015, Flex® Robotic System (Medrobotics Corp., Raynham, MA, USA) obtained U.S. FDA approval for performing TORS (**Fig 2.8b-c**). Comparing two transoral robotic surgical systems, Flex® Robotic System is composed of a continuum structure rather than rigid links. Also, an additional tactile feedback is installed for Flex® Robotic System over the da Vinci® Surgical System [51]. Flex® Robotic System is equipped with flexible CO_2 laser fiber (AcuPulse 40WG, Lumenis) to perform tissue dissection. This coupling combination of robotic system with TLM enhances the reachable surgical site. It enables the flexible laser to access to the pharynx, hypopharynx, and parts of the larynx.

2.3.2.3   Upcoming TORS system

The setup cost and operating cost for the above-mentioned TORS system is high. For example, the setup cost of the da Vinci® Surgical System is about two million U.S. dollars. As the Type II flexible laser heavily relies on the robotic navigation system, the high cost of TORS will become one of the major hindrances. In view of the high cost of the robotic surgical system, the upcoming TORS systems are aimed to build at low cost. Titan Medical Incorporation, a Canadian-based company, is now developing a single port robotic system called Single Port Orifice Robotic Technology (SPORT) Surgical System (**Fig 2.8d**). Moreover, it is expected to receive U.S. FDA approval and CE Marking by 2019. The SPORT Surgical System has half of the setup cost and one-fourth of the operation cost than the da Vinci® Surgical System. However, the aforementioned robotic systems still cost at least one million U.S. dollars for installation. Therefore, an inexperience robotic navigation system can enhance the accessibility of Type II TLM to more hospitals and accelerates the development of transoral robotic laser surgery in the future.

2.4   DIAGNOSIS AND SCANNING MODALITIES

The discovery of HNCs started by alerting health symptoms such as prolonging sore, pain in jaw or tongue and unusual cell growth in the transoral cavity. Ear, nose, and throat (ENT) doctors will perform a visual examination on the oral cavity, tongue, back of the throat, cheeks, and lymph nodes in the neck. Once the suspicious or abnormal site is located, the doctor will perform a direct biopsy with examination-under-anesthesia (EUA). In EUA, the patients' muscles are relaxed and more accessible to the doctor for taking a biopsy. The removed tissue biopsy will then be examined under a microscope for cancerous cells. Meanwhile, other scanning imaging tests can be performed in parallel to obtain comprehensive information about the location of the cancerous cells.

There are two kinds of imaging modalities, namely (**i**) anatomic imaging and (**ii**) functional imaging. Anatomic imaging modalities for HNCs are ultrasound,

computed tomography (CT) and magnetic resonance imaging (MRI). Ultrasound imaging is radiation-free and provides real-time imaging at high refresh rates (40 Hz). However, it only offers a quick preview of the suspicious site with a low spatial resolution of 3 mm, whereas CT and MRI have a spatial resolution of about 1 mm. Anatomic imaging usually presumes the anatomy is not actively moving and no tissue shifting over time. However, the soft tissues are actually shifting during the scanning process in reality. As a result, there are various techniques to correct the geometric distortion, such as non-rigid registration [52]. Nowadays, CT and MRI have become a reference imaging modality for disease diagnosis. CT scan was first used in 1971. CT images, however, are lack of contrast to show soft tissue structures and tumor extensions. Therefore, CT scan is assisted by an iodine-based contrast agent to identify soft tissues. When scanning HNCs, CT images are degraded by the presence of dental fillings (e.g., amalgam, composite resin). This limits the imaging performance of the oropharyngeal tumors' assessment. In term of tumor distinguishability, MRI is more preferred for its strength in discerning soft tissues by using various sequences. Moreover, MRI scan is lack of ionizing radiation than CT scan and reduces potential harm by exposing the patient to unnecessary radiation.

Functional imaging, also known as metabolic imaging, is a technique for imaging organ and tissue activities. For instance, glucose uptake level is monitored as glucose is a biosynthetic precursor to cancerous cells. Positron emission tomography (PET) scan and functional MRI (fMRI) are examples of functional imaging. These techniques usually have a relatively low spatial resolution of 2 mm. In addition, the lack of anatomical landmarks makes the diagnosis process challenging to analyze. Instead of using CT contrast agents, PET scan uses radioactive fluorine-18-fluorodeoxyglucose (FDG) as an indicator to detect metabolic differences and chemical activity in the body. As the cancer cells tend to divide and grow more rapidly than the healthy cells, they absorb large amounts of the radioactive FDG. By monitoring the radioactivity in PET scan, the metabolic activities are evaluated and the region of the cancerous cell is indicated by the highest metabolic rate. However, PET scan does not provide accurate geometrical

information without reference images or contours, whereas fMRI can combine with preoperative or intraoperative MRI to form a registration reference for a geometrical marking.

2.4.1 Intraoperative MRI-guided Intervention

Among all scanning modalities, CT demonstrates the insufficiency of tissue contrast, whereas PET scan shows the incapability of locating cancer cells without anatomical scans. Co-registration is attempted to overlap functional images with the anatomical images, such as PET/CT scan, and PET/MRI scan. The rationale of combined imaging is to accurately locate and dissect the cancerous tumor to reduce preoperative morbidity. The current intraoperative analysis for transoral surgery is frozen section analysis (FSA), which takes 10 minutes during the operation [53]. Research has been done for online estimation of the laser incision depth based on statistical regression [54]. Intraoperative MRI (iMRI) scan is the best alternative to evaluate resection process, as the MRI scanner provides both anatomic and functional imaging in a single console. Unlike analyzation of the resected specimen by FSA or statistical prediction, iMRI aimed to detect the residual tumors in the body instead of the resected specimen. With the intraoperative imaging, the degree of tumor dissection can be evaluated during the operation. In addition, shifting of transoral soft tissues is unavoidable even though the patient is sedated, but iMRI offers an up-to-date anatomy assessment. The surgeon can optimally resect the cancer cells with a positive margin by the MR-guided images.

2.4.2 MR Thermometry

Apart from offering imaging feedback to the surgeon, MRI also provides a built-in function for thermal therapy monitoring. Based on the temperature-dependent MR parameters, MR thermometry [55-57] provides temperature map for monitoring the overall treatment outcome (**Fig 2.9**). There are six MR-based parameters, namely T_1 relaxation time constant, T_2 relaxation time constant, molecular diffusion coefficient, magnetization transfer, proton density and proton resonance frequency shift (PRFS). The advantages and disadvantages of MR-based parameters are listed and compared in **Table 2.3**.

Table 2.3 Comparison of MR-based parameters for MR thermometry [55]

Method	Characteristics and Remarks	
T_1 relaxation time constant [58]	_Pros:_	• _Readily available imaging sequences_
	Cons:	• _Cannot be applied for fat tissue_
		• _Low temperature sensitivity (1 %/°C)_
		• _Non-linear dependence of T_1 on temperature_
T_2 relaxation time constant [58-60]	_Pros:_	• _High temperature sensitivity (10 %/°C)_
		• _Can be applied for fat tissue_
	Cons:	• _T_2 are shorter than T_1, which makes measurement difficult_
		• _Irreversible signal change at high temperature due to tissue damage_
Diffusion coefficient D_{diff} [61, 62]	_Pros:_	• _Readily available imaging sequences_
	Cons:	• _Low temperature sensitivity (2 %/°C)_
		• _Other factors can change D_{diff}, like temperature-dependent activation energy_
Magnetization transfer [63, 64]	_Pros:_	• _Can be used with other magnetization transfer applications_
	Cons:	• _Non-linear function of tissue is not accurately quantified_
		• _Temperature deduction by magnetization transfer is tissue-dependent_
Proton density [65]	_Pros:_	• _Readily available imaging sequences_
	Cons:	• _Low temperature sensitivity (0.29 %/°C)_
Proton resonance frequency shift (PRFS) [66, 67]	_Pros:_	• _Readily available imaging sequences_
		• _Fast temperature mapping techniques_
	Cons:	• _Cannot be applied for fat tissue_
		• _Low temperature sensitivity (0.01 ppm/°C)_
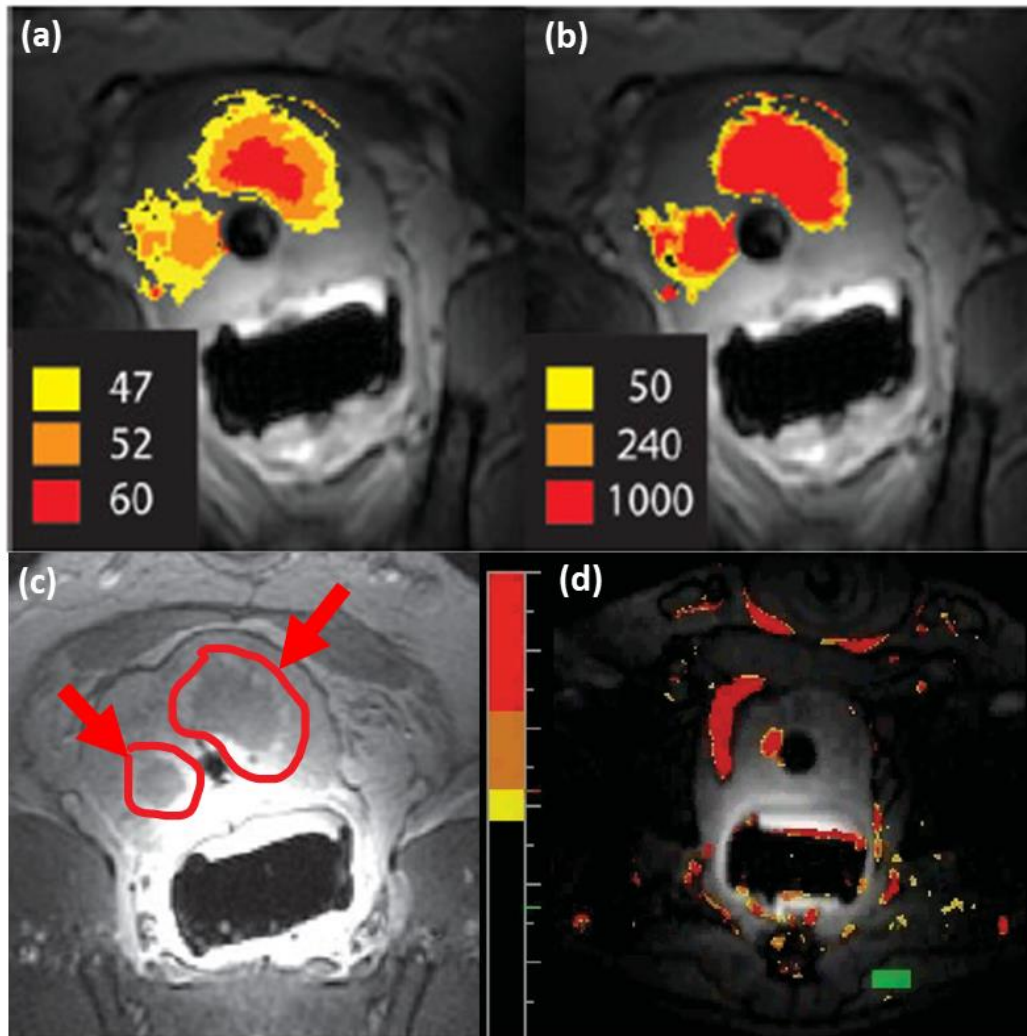
Fig 2.9 MR thermometry used for *in-vivo* canine prostate ablation. MR thermometry (**a**) in maximum temperature and (**b**) in thermal dose map. (**c**) Post-treatment contrast-enhanced image showing ablation trace. (**d**) Mis-registration caused by tissue displacement after ablation. **Image Source: [56]**

MR thermometry is non-ionizing and non-invasive. This MRI built-in function can be subdivided into two regimes, classified by the sensitive temperature region of: (**i**) low temperature hyperthermia (43 - 45°C) and (**ii**) high temperature thermal ablation (50 - 80°C). By utilizing two sensitive sub-regimes, the former low-temperature regimes can aim to provide the targeting position of the aiming laser, whereas the second high-temperature mode can be used to evaluate the thermal affected zone during and after laser surgery. The important rationale of using MR thermometry is to monitor the laser dissection margin and thermal damages to the peripheral tissues. Laser-induced interstitial thermotherapy (LITT) is one of the minimally-invasive MRI treatment [68]. In addition, high-intensity focused ultrasound (HIFU), as one of the FDA-approved cancer treatment, also

assisted by MR thermometry to visualize temperature mapping in the respective surgical region [57]. As a result, By depositing optical energy to the tissue through laser fibers, MR thermometry provided positional information when monitoring the thermal activities [56]. It enhances the accuracy of the surgical intervention by tracking the positional feedback of the laser aiming zone. Therefore, by aiming the laser at the tissue surface with lower *PD*, temperature increase can be indicated by MR thermometry. The computation technology nowadays is not fast enough for a real-time isotropic 3D temperature mapping reconstruction. However, it is still feasible to cover a small 3D volume with multiple slices. For transoral laser surgery, only a few coronal planes are required for capturing a specific volume such as the nasopharyngeal wall. NeuroBlate® System (Monteris Medical, Plymouth, MN) performed MR thermotherapy by employed LITT in neurosurgery [68]. This proved the feasibility of MR thermotherapy for intraoperative laser surgery.

2.4.3 MR-conditional Robot

MRI system provides anatomical structures and also indicates temperature mapping by MR thermometry. The laser projection position can be tracked by integrating both imaging results. Therefore, the compatiblity of the laser robotic platform needs to be ensured. Two MR evaluation tests, namely MR-safety and MR-compatibility test, are essential to ensure no potential risk to the patient and to guarantee the imaging quality of the diagnostic information [69]. In American Society for Testing and Materials (ASTM) F2503-05 published in 2005 [70], MR-safety evaluates the ferromagnetic property, magnetic field interactions, potential harm for thermal injury, and induced electrical currents of the robotic device under MR environment [71], whereas MR-conditional requires MR-safety plus no image artifacts induced in a testing phantom. Image artifacts were evaluated according to the guidelines provided by National Electrical Manufacturer's Association (NEMA) [72]. The MR images corresponding to baseline condition and robot operating were compared. Pixels with an intensity that varied by 30% or above were considered as artifacts by the ASTM-F2119. With multiple advantages of MR thermometry, an MR-conditional robotic system is worth to design and test the feasibility for TLM under MRI.

2.5 CONCLUSION

Nasopharyngeal cancer is relatively prevalent in Southeastern China such as Hong Kong, whereas oral, pharynx, and larynx cancers are prevalent in the surrounding countries. The traditional surgical open approach left an incision on the head or neck, which causes trauma to the patient and induces long recovery time. Even though the non-surgical RT and CTx replaced open surgery in the 1920s, the toxicity of RT and CTx affected the peripheral tissues and degraded swallowing function. As a result, alternative locoregional treatment is essential for effective HNCs' curing with the least side effects and post-surgical trauma. In 2009, TES arose with the FDA-approved surgical system of TORS and TLM. Traditional transoral Type I laser possesses with rigid manipulator and can only access to the base of tongue. However, TLM nowadays has flexible laser technology, such as CO_2 fiber laser and thulium laser. The flexible Type II laser can reach the ONP cavity guided by the transoral robotic system. However, flexible Type II laser heavily relies on the TORS system to navigate the laser collimator. TORS also requires extra maneuvering workspace and thus requires a transoral retraction system that costs setup time of one hour. Therefore, a surgical robotic endoscope that navigates the laser fiber can reduce setup time for the retracting system before surgery.

Sometimes, the surgeon needs to intraoperatively perform FSA to determine the completeness of cancer resection. FSA is accomplished via a two-level or three-level method concerning the number of cut on the frozen section specimen. Microscopic analysis of the resected specimen took about 10 minutes during the operation. Given this, iMRI can be an alternative to predict whether the cancerous tissue is wholly resected during the surgical procedure. MRI evaluates the gross tumor volumes intraoperatively and also offers MR thermometry. MR thermometry can track the pointing direction of the laser collimator and thus provides positional feedback for the robotic control. However, the current existing TORS cannot be used in MR environment due to the ferromagnetic material inside motors. Therefore, an MR-conditional robotic laser system is essential to be developed for locoregional

28

laser dissection under MRI. This robot aims to provide a locoregional treatment for curing HNCs for organ function preservation.

In this study, we aim to develop a minimally-invasive robotic laser system for intracavitary laser therapy. An inexpensive MR-conditional robotic system can alleviate both installation and operation costs. In **Chapter 4**, we will introduce soft robotics as an excellent actuation system to navigate the flexible laser by its agility, compliance. The purpose of this thesis is to address the concept of the MR-conditional soft medical robot for transoral laser surgery under MRI. The objectives of my research study are:

i.   To design a world-first 3D-printed, MR-conditional reinforced soft robot (RSR) for MRI-guided laser surgery.

ii. To optimize the design parameters and analyze the stress distribution of the RSR by using finite element analysis (FEA).

iii. To control the hydraulic-actuated RSR to follow various projection trajectories for accurate laser dissection.

iv. To develop a standard protocol for constructing patient-specific dental anchorage platform for endoscopic insertion.

v.   To validate the feasibility of the proposed 3D-printed robotic system by pre-clinical trial on the *ex-vivo* tissue under MRI.

CHAPTER 3

CUSTOMIZATION OF DENTAL ANCHORAGE PLATFORM AND SPECIFICATION OF SURGICAL LASER

3.1 INTRODUCTION

I N the previous Chapter, the clinical background of the oral, nasopharyngeal (ONP) cancer in the Asia region have been outlined. The treatment modalities and related surgical robotics system for the transoral surgeries have also been categorized. Before designing the surgical robotic system, the environmental constraint of the target surgical site must be first evaluated. In this Chapter, I will determine the size of the transoral cavity by the CT/MR images and cadaveric data in the literature. Also, a patient-specific dental guard is designed to replace the use of a conventional retractor system for a minimal invasion to the patient. Moreover, fiber optics principles will be investigated to evaluate critical parameters of the robotic design.

3.1.1 Problem Formulation

Nasopharyngeal cancer is highlighted explicitly with its high prevalence in Southeast Asia including Hong Kong. In this study, the targeting surgical site is the ONP cavity (**Fig 3.1a**), which is beyond the base of tongue. Two jaw configurations of opened-jaw and closed-jaw of the month strongly affect the anatomy and workspace of the ONP cavity. The figure highlights the ONP cavity in a closed-jaw anatomy. The ONP workspace analysis will start by the closed-jaw configuration, as closed-jaw configuration is commonly available in the shared online DICOM library. Then, the opened-jaw ONP anatomy will be obtained by scanning with the patient-specific dental guard under magnetic resonance imaging (MRI). The design and fabrication of the static anchorage dental guard will discuss in **Section 3.2**.

3.2 STATIC ANCHORAGE PLATFORM FOR ROBOTIC SURGERY

For both transoral robotic surgery (TORS) and transoral laser microsurgery (TLM), the robotic arms or endoscopes enter via the natural orifice. The mouth cavity provides a static anchorage platform and a maneuvering space for the endoscope. However, the natural transoral configuration does not offer sufficient workspace for TORS maneuvering. Therefore, developing a retracting system can increase workspace for transoral surgery. In addition, the retracted transoral anatomy allows accommodation of extra endotracheal tubes, endoscopes, or robotic effector arms.

The first retracting system developed for TORS is called Feyh-Kastenbauer (FK) retractor (Gyrus ACMI, Southborough, Massachusetts). Nowadays, companies develop retractors for their TORS system. For example, Larynx Advanced Retractor System (LARS) (FENTEX medical, Tuttlingen, Germany) (**Fig 3.1b-c**) is developed for the da Vinci® Surgical System, whereas Flex® Surgical Robotic System has also developed Flex® Retractor (**Fig 3.1d**). Both retractors add extra features to the FK retractor. Flex® Retractor offers a curved shape design to fit patients' face. Moreover, convex LARS extends the horizontal framework to increase the visualization field [73] and adds an adjustable tongue blade to cope with a variety of patients.
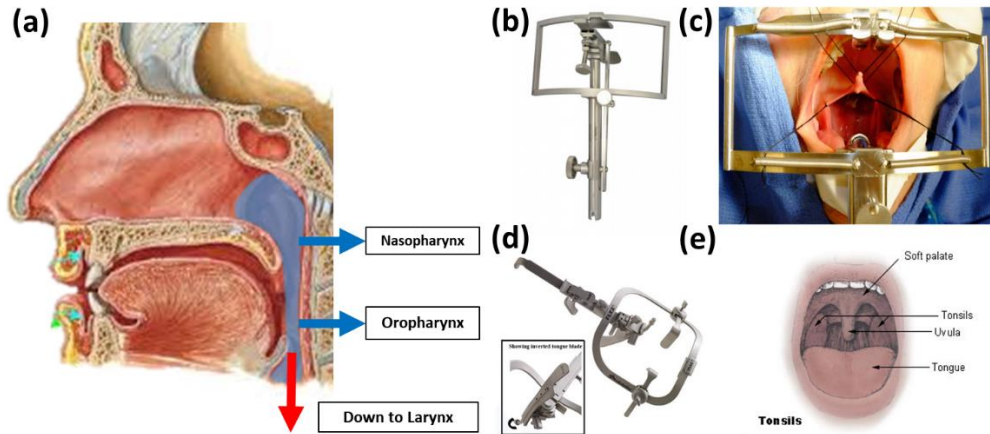
Fig 3.1 **(a)** Oral anatomy in closed-jaw configuration showing ONP cavity (blue) of oropharynx and nasopharynx. Closed-jaw configuration reduced ONP workspace in terms of oral cavity and pharyngeal channel. **(b)** LARS retractor manufactured by FENTEX medical. **(c)** Setup of the retraction system by stitching uvula and tonsils to enlarge visible workspace. **(d)** Flex® Retractor system manufactured by Flex® Surgical Robotic System. **(e)** Anatomy of oral cavity showing landmarks of soft palate, tonsil, and uvula. **Image Source: Intuitive Surgical Inc., Medrobotics® Corporation**

The soft palate and uvula are the major obstacles to the transoral surgery (**Fig 3.1e**). LARS provides unobstructed access to the ONP cavity by stitching and pulling the uvula. After retraction, the overall workspace is enlarged for endoscopic maneuvering. Therefore, anatomical data for the opened-jaw configuration is also essential for the design of the endoscope. Anatomical parameters had been measured in three human cadavers by LARS. The measured anatomical parameters are presented in **Table 3.1**.

Table 3.1 Measurement of oral anatomy of three cadavers after uvula retraction [50]

Measurement	Cadaver 1	Cadaver 2	Cadaver 3
Cadaver Height	163 cm	173 cm	163 cm
Cadaver Weight	39 kg	59 kg	70 kg
Distance from mouth to the uvula	55 mm	55 mm	45 mm
Width between two tonsillar pillars	45 mm	40 mm	40 mm
Distance between uvula and pharyngeal wall	35 mm	35 mm	35 mm

In this study, instead of using TORS retracting systems, we developed a custom-made dental anchorage guard (**Fig 3.2**) for the laser surgery. The dental guard is constructed with the patient-specific dental arches and provides channels for endoscopic insertion. The dental guard is designed to maximize the jaw-opening distance, while minimizing the procedure for uvula stitching. Thus, the dental surgical guard is a minimally-invasive anchorage platform and reduces setup time. This shortens setup time is shifted to the preoperative preparation with oral cavity reconfiguration and dental guard fabrication, which is beyond the surgical time and increase the usage efficiency of the operation theatre.

3.2.1 Fabrication of the Patient-Specific Dental Guard

In view of the lengthy and invasive surgical preparation by LARS, we proposed a custom-made docking module anchoring on the oral cavity called the dental guard. This mechanical module is attached non-invasively and seamlessly on the teeth and dental alveolus. This stabilizes the jaw opening distance for 35 mm and maximizes the maneuvering space for the robot. For instance, the stitching and pulling off the uvula are avoided. Therefore, the dental guard reduces the degree of invasion and significantly accelerates the overall surgical time. The fabrication process will be discussed in this section.

Firstly, the dental impression is obtained by a fast set alginate (GC Aroma Fine Plus®). Maxilla and mandible surfaces (**Fig 3.2a**) for a specific patient are obtained by a 5-minute set alginate. Secondly, A custom dental plaster (ProBase hot acrylic resin) (**Fig 3.2b**) is then cast to form a clone by reverse molding of the fast set alginate. Finally, a dental guard prototype (**Fig 3.2c**) is constructed by the polymethylacrylate accordingly with respect to the dental plaster. Oral cavity workspace created in-between maxilla and mandible can be maximized ($> 25 \times 25 \times 20$ mm^3) by further pressing the tongue downward. This enlargement methodology of the oral workspace can reduce the invasion of the soft palate and uvula.

香港大學圖書館 HKU Libraries

In addition, the dental guard can also be designed by computation modeling. 3D point cloud of the dental maxilla and mandible surfaces are scanned by 3D stereo optical scanner (3M™ True Definition Scanner) (**Fig 3.3a**). With the captured 3D surfaces by optical scanning, the dental guard model possesses with the reconstructed 3D dental impression feature. Rather than direct scanning in patients' mouth, 3D scanning is performed by the dental plaster. This increases the scanning stability and hence scanning accuracy without much motion artifact. Employing 3D scanning on dental impression surfaces (**Fig 3.2c**) for dental guard design can ensure seamless anchorage to the patient teeth (**Fig 3.2d**), thus providing a stable docking and positioning for the robotic system through the oral cavity.
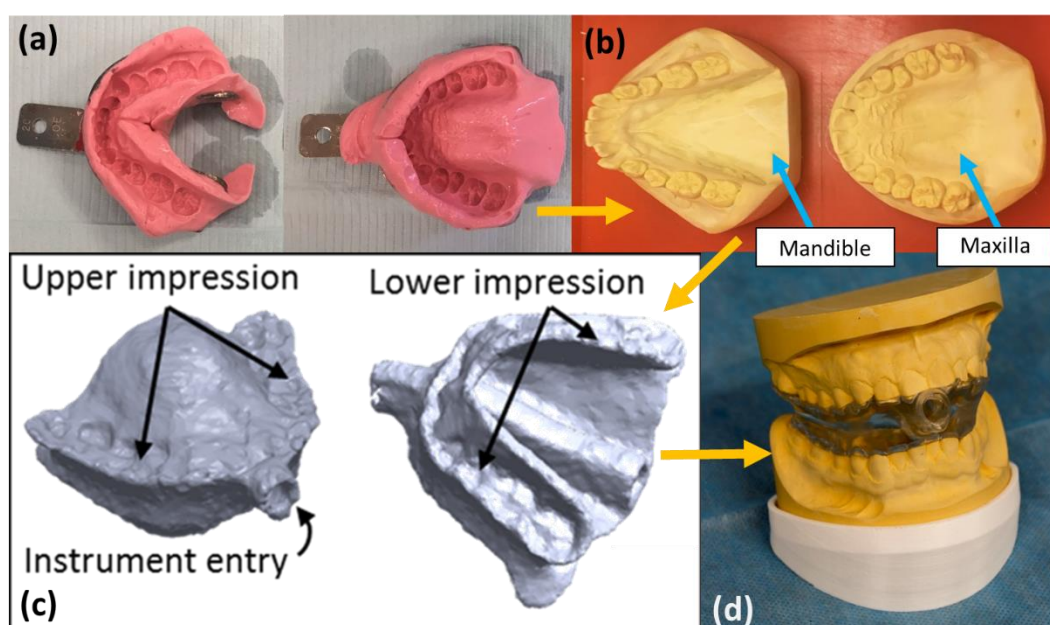
Fig 3.2   Fabrication procedures of dental guard. **(a)** Fast set alginate (pink) capturing patients' dental impressions in mandible and maxilla. **(b)** Reverse dental gypsum molded by alginate dental prints. **(c)** Fabrication of dental guard prototype by bio-compatible acrylic resin. **(d)** Integration of dental guard with the dental gypsum model showing enlargement of open-jaw distance. Dental guard provides sufficient workspace ($> 40 \times 40 \times 20$ mm^3) for transoral surgical interventions.

A fixed open bite distance for the dental guard is modeled as 35 mm (**Fig 3.3b**). This enlarged workspace can accommodate two endoscopic entrances. Also, mechanical interlocks are designed in the endoscopic entrance for robot integration. These complex structures are added in a 3D modeling software (Blender). Moreover, three MRI fiducial markers (**Fig 3.3c**) are allocated non-linearly to act as image registration landmarks. This offers steady frame-of-reference relative to

the robot base in the MR image coordinates. The MRI fiducial markers $(8 \times 4 \times 1 \text{ mm}^3)$ are activated in MRI by using capsulized vitamin E or wireless inductive coupling radiofrequency (RF) microcircuit. The dental guard is fabricated by 3D-printing with bio-compatible material called MED610^{TM} (Stratasys Ltd., U.S.). In addition, the bio-compatible dental guard is tested by putting into the patients' mouth cavity (**Fig 3.3d**). It is proved that the dental guard ensured a stable and static anchorage without backlashing between maxilla and mandible.
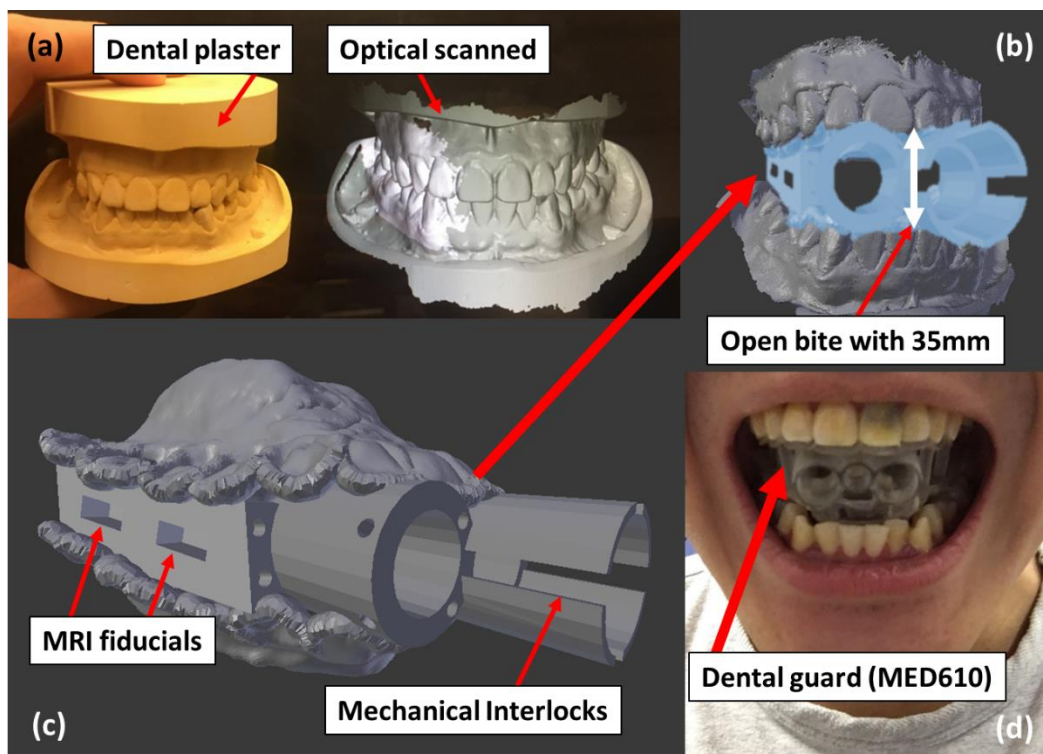
Fig 3.3   **(a)** Precise 3D optical scanning of dental arches captured by 3M™ True Definition Scanner. **(b)** 3D modeling of dental guard with 35 mm opening distance. **(c)** MR-fiducials and instrument channels accommodated inside dental guard. Design of mechanical interlocks enables anchorage of the dental guard to the entire robotic system. **(d)** Custom-made dental guard placing in patients' month for validation. Dental guard is directly 3D-printed by bio-compatible MED610^{TM}.

3.3 WORKSPACE EVALUATION BY 3D MRI RECONSTRUCTION

Instead of estimating the ONP anatomy only by cadaveric data, the overall ONP workspace in closed-jaw configuration needed to be also investigated and reconstructed by using CT/MR images from the online DICOM library (DICOM Library, SOFTNETA). The constraint of the overall surgical scenario can be simulated to evaluate the maneuvering workspace for the surgical robot.

3.3.1 Closed-jaw Configuration from Online DICOM Library

CT/MR images in the closed-jaw configuration are used in the first stage, which only provides information for the ONP cavity. DICOM images are oriented in three principal planes, namely axial, sagittal, and coronal plane. Images are analyzed by a DICOM reconstruction software (InVesalius) and displayed in three principal planes. Body parts are differentiated by various threshold values. By selecting the range of imaging threshold, the corresponding 3D surfaces are generated (**Fig 3.4**). A region of interest is then manually segmented by deleting irrelevant surfaces. For instances, after selecting thresholds for the soft tissue, skin surfaces on patient face are necessary to be removed to obtain the anatomy of ONP cavity (**Fig 3.4d**). The generated 3D surfaces will then be exported to a stereolithographic (STL) file for further processing. After repairing the unclosed contour in the STL file by an editing software (Blender), the anatomy of the nasal cavity, sinuses, and pharyngeal cavity are obtained. However, the closed-jaw configuration only provides approximate constraint for the pharyngeal cavity, but not the oral cavity. Opened-jaw configuration with a retraction system such as LARS or Flex® Retractor is necessary to be acquired to evaluate the transoral scenario. In this research, we employ an MR-conditional dental anchorage system, instead of the conventional retraction system, to avoid invasiveness to the patient. MRI scan is obtained with the dental guard in **Section 3.3.2**.
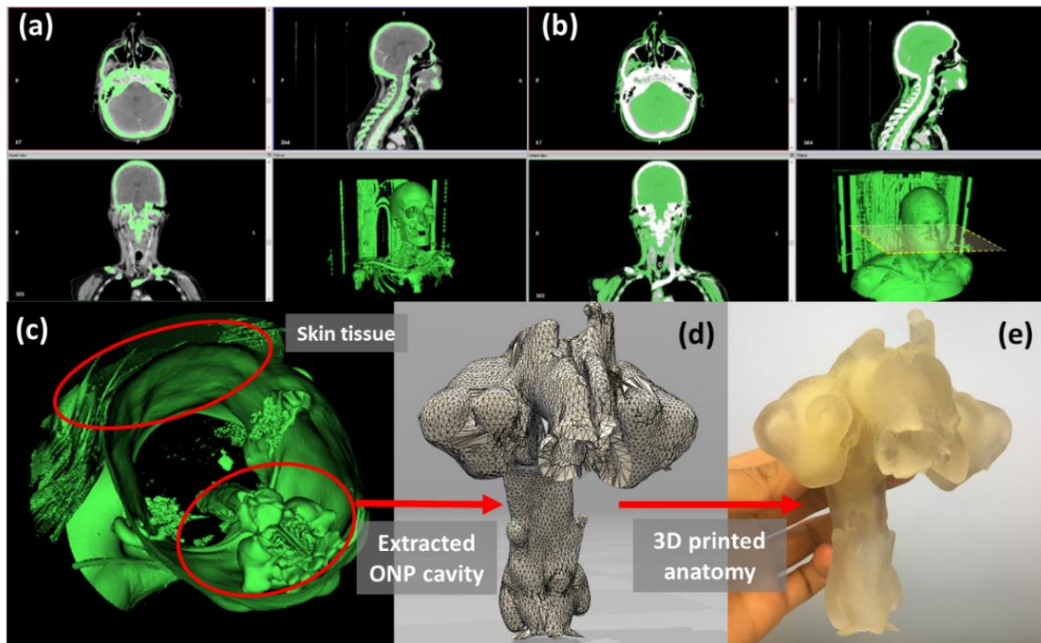
Fig 3.4 Segmentation of ONP anatomy from MRI DICOM. **(a)** Segmentation of high threshold range of 226 to 3071 showing bone structure. **(b)** Segmentation of low threshold range of –718 to –177 showing skin tissues. **(c)** Isometric view of the segmented soft tissue with respect to the transverse plane. **(d)** Extracted ONP surface model converted into stereolithographic (STL) file for dimension evaluation. **(e)** 3D-printed ONP anatomy by MED610^{TM} for illustration.

3.3.2 Opened-jaw Configuration with MRI Scan

In the standard protocol, head and neck scans with closed-jaw configuration are obtained by the radiologist. Therefore, no CT/MR images can be found in the shared online DICOM library with the opened-jaw configuration, not to mention a scanning image with the retracting system. Technically, it is infeasible to have clear CT/MR images with the retracting system that is comprised entirely or partially of metal. Therefore, our research proposes to use an MR-conditional and bio-compatible dental anchorage system with the patient-specific dental feature. With the aforementioned difficulties and unavailability of finding open-source opened-jaw imaging, I proposed to perform an MR imaging with the self-developed dental guard for the opened-jaw configuration. T1-weighted fast spoiled gradient echo (FSPGR) is used as the imaging sequence, which displays detailed anatomic structure and detects embedded lesions (e.g., lymph node lesions) within fat [74]. The extracted ONP space with the oral cavity is modeled as a phantom to evaluate the workspace for the transoral robot. The resultant transoral phantom model in opened-jaw configuration is 3D-printed by AgilusClear30^{TM}, which is an elastomeric material to mimic elasticity of soft tissues in human.
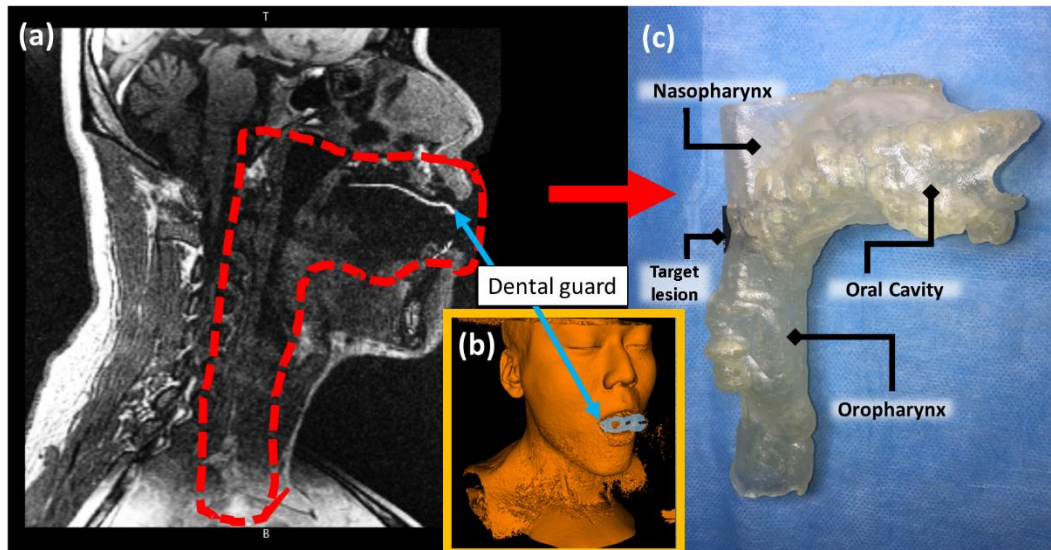
Fig 3.5 **(a)** MR image showing head and neck of patient in the sagittal plane. MRI scan is performed by 3D T1-weighted FSPGR. **(b)** MR reconstructed volume showing custom dental guard in patient's mouth. **(c)** Phantom model of the transoral anatomy including oral cavity, nasopharynx, and oropharynx. Transoral phantom model is 3D-printed by elastomeric AgilusClear30^{TM}.

3.4 SELECTION OF TRANSORAL LASER DISSECTION

For direct rigid laryngoscopy, the retracting system intrusively straightens the neck and reach larynx or vocal cords directly. Our surgical modality, however, deploys a minimally-invasive dental anchorage system. This enables to provide an entrance for the robotic endoscope system to navigate the flexible fibers to bend and reach larynx.

Both closed-jaw and the opened-jaw configurations have provided anatomical information and parameters, such as robot maneuvering workspace and the pathway for the surgery. For instance, with the MR images, we can evaluate the bending curvature in the base of tongue, which is about 40 mm in bending radius. Carbon dioxide (CO_2) laser fiber is not appropriate for our study, as the hollow-core photonic bandgap optical fiber will have a high macrobending loss even with a small specified bending radius of 25 mm. The specification of the laser fiber and bending loss (or attenuation) will be discussed in **Section 3.4.1**.
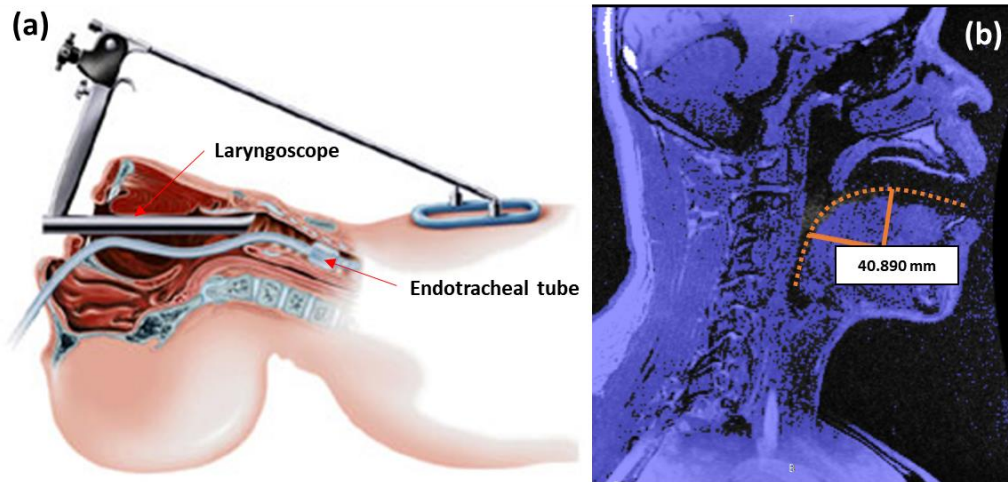
Fig 3.6 **(a)** Direct Laryngoscopy intrusively straightening transoral anatomy. This ensures a clear vision for the surgeon of the larynx and vocal cord. **(b)** Sagittal plane of opened-jaw configuration showing the bending curvature in base of tongue. Bending radius is evaluated as 40.89 mm across the transoral anatomy.

3.4.1 Specifications of Laser Fiber

A laser fiber consists of a circular silica core and two or more fiber cladding clasped to the core. Laser radiation is transmitted through the silica fiber core with the highest refractive index. The silica core is entrapped by primary and secondary cladding layers of lower reflective indices, which serves to confine the light to the fiber center. The overall laser fiber is protected by a buffer layer made of multiple coats of plastic materials. The buffer layer conserves the integrity of the fiber and serves as a shock absorption layer. Some of the laser fibers add metallic sheaths for further physical protection. The standard size for the optical core of the laser fiber is 200 µm (ProFlex LLF), with the primary and secondary cladding included with 240 - 260 µm. Finally, the mechanical protection overlaying buffer costs an overall diameter to 400 µm. Illustration of laser fiber structure is shown in **Fig 3.7a**. The figure shows the step change of the refractive index from the core to the cladding material.
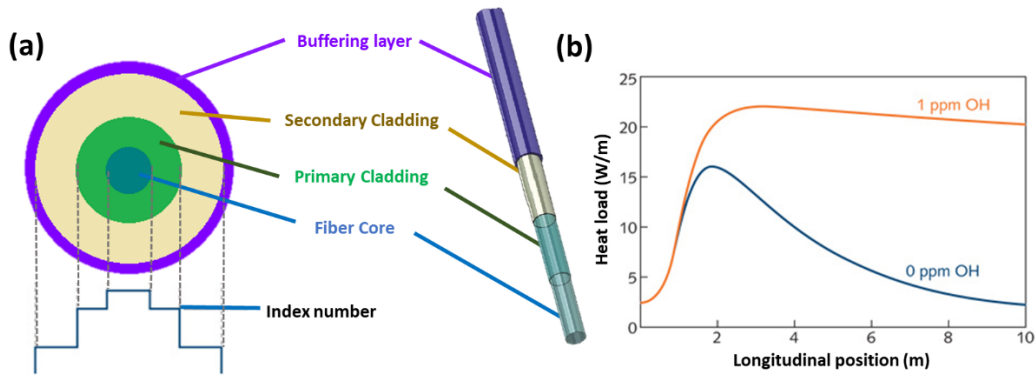
Fig 3.7 Design specifications for optical delivery fiber. **(a)** Cross section of laser fiber showing four medium layers. They are optical core (blue), primary (green) and secondary (yellow) cladding, and the outermost buffer layer (violet). Refractive indices decrease with increasing radial distance from the optical axis. **(b)** Heat load against longitudinal distance of fiber varied by hydroxyl ion (OH⁻) concentration. Two concentrations (0 - 1 ppm) of OH⁻ level are compared. High OH⁻ level indicates higher heat loss. **Image Source: [75, 76].**

Standard laser fiber used silica as the core material. For the transmission of the holmium and thulium lasers, purified silica in low hydroxyl ion (OH⁻) concentration is more favorable to eliminate power loss due to the absorption effect by the OH⁻ ion [77]. Transmission percentage per meter is 97% in low OH⁻ concentration (~1 ppm) fused in silica. **Fig 3.7b** illustrates the heat loss increase with the concentration of the OH⁻ level. Ideal silica fiber with OH⁻ level of 0 ppm causes the lowest energy loss for transmission.

3.4.1.1 Acceptance Angle

Laser beams are created when resonantly pumping a particular wavelength to the laser medium. The resultant laser beams are then collimated into the laser fiber via an up-collimator to reduce light divergence. When the laser beam travels between mediums (e.g., from air to silica), Snell's law gives the relationship of the angle of incidence and angle of refraction:

$$n_i \sin \theta_i = n_r \sin \theta_r \tag{3.1}$$

where n is the refractive index of the medium (1.00 for air, 1.46 for typical silica core), θ_i indicates the incidence angle of the first medium, whereas θ_r indicates the refraction angle of the second medium. Assumed the proximal end of the laser fiber is straight, the maximum divergence angle is defined as the acceptance angle (or "acceptance cone" in three-dimensional space) for laser transmission with

40

minimal bending of the fiber. The acceptance angle is related to the numerical aperture (*NA*) of the optical lens or collimators. The *NA* is the sine of the acceptance angle travel multiplied by the refractive index of the medium. Typical *NA* varies from 0.05 to 0.4 for single mode fiber, which means the acceptance angle ranging from 2.87º to 23.6º. Applying the correlation of *NA* to the case in the optical fiber (**Fig 3.8**) gives the **Equation 3.2**:
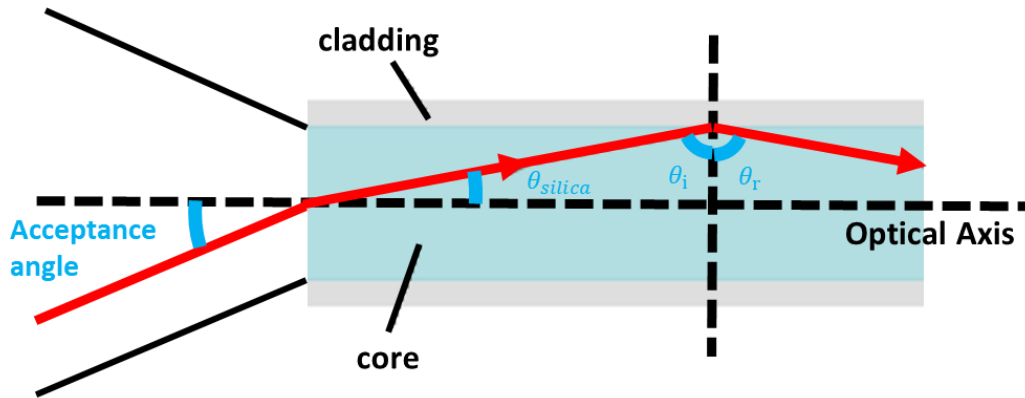
Fig 3.8   Schematic ray diagram showing proximal end of laser fiber. Laser beam is introduced from the pumping laser source with an acceptance angle θ_a. Laser beam is then reflected internally to optical axis with a propagation angle θ_{silica}.

$$NA = n_a \sin \theta_a = n_{silica} \sin \theta_{silica} \tag{3.2}$$

where n_a is the refractive index in the air, n_{silica} is the refractive index in the silica fiber core, θ_a is the acceptance angle from the air medium, and θ_{silica} is the refracted angle inside the silica fiber core. The *NA* of the fiber and laser emission wavelength λ strongly affect the minimum achievable laser spot diameter d_{min}. The relationship is given in **Equation 3.3**:

$$d_{min} \approx \frac{1.22 \times \lambda}{NA} \tag{3.3}$$

The laser spot diameter d_{min} is directly proportional to the emission wavelength λ of doped element. Therefore, laser with lower emission wavelength has a smaller achievable spot diameter due to a smaller diffraction effect. For instance, Tm-doped laser and Ho-doped laser have a smaller minimum achievable laser spot diameter d_{min} than the CO_2 laser.

The cladding material serves as a fail-safe boundary for minimal bending and reflects the laser beam back to the optical axis. Whenever the injected laser beam strikes the core-to-cladding interface, total internal reflection (TIR) will occur when the criteria are satisfied. The concept of TIR is widely adopted and used in long-distance light transmission with a zig-zag pathway. TIR occurs when two criteria are fulfilled, which are:

(i)   Light ray travels from a denser medium to a less dense medium ($n_i > n_r$) and

(ii)   Incidence angle exceeds the critical angle ($\theta_i > \theta_c$).

Therefore, the step decreases of the refractive index ($n_{silica} > n_{clad}$) is a critical criterion for the occurrence of TIR. In **Equation 3.1** given by Snell's law, when the refraction angle is greater than 90°, there will be no refracted ray and the light will be bounced back to the first medium. When the refractive angle becomes 90°, the corresponding incident angle is called the critical angle. The critical angle depends on the refractive indices of core and cladding. The critical angle for laser travel from a denser silica core to a less dense cladding is given by:

$$\sin \theta_c = \frac{n_{clad}}{n_{silica}} \tag{3.4}$$

For $n_{silica} > n_{clad}$ and $\theta_i > \theta_c$, the laser beam will be totally reflected inside the silica core. The refractive angle from the collimated laser beam θ_{silica} is complementary to the critical angle θ_c ($\theta_{silica} + \theta_c = 90°$). Back substituting **Equation 3.4** back to **Equation 3.2** gives a relationship of refractive indices to the *NA*:

$$NA = n_{silica} \sin\left(90° - \theta_{silica}\right) = n_{silica} \cos\theta_{silica}$$

$$NA = n_{silica} \sqrt{1 - \sin^2\theta_{silica}}$$

$$NA = \sqrt{n_{silica}^2 - n_{clad}^2} \tag{3.5}$$

42

3.4.1.2 Divergence Angle

NA not only governs the acceptance angle of the introduced laser but also reflects the divergence angle θ_{div} in the distal end of the optic fiber by the following expression:

$$NA = \sin\theta_{div} = \frac{(r - d_{core})}{\sqrt{(r - d_{core})^2 + d_{proj}^2}}$$

$$d_{spot} = \frac{2L_{proj} \times NA}{1 - NA} + d_{core} \qquad \textbf{(3.6)}$$

where *r* is the radius of the laser spot, d_{spot} is the diameter of the laser spot, d_{core} is the silica fiber core diameter, and L_{proj} is the projection distance from the laser tip. As *NA* is less than 1 (*NA* < 1), the spot diameter d_{spot} increases with *NA*. Therefore, the spot diameter d_{spot} is directly proportional to the projection distance L_{proj} and the numerical aperture *NA*. **Fig 3.9** shows the relationship of the laser spot diameter d_{spot} to the propagation distance L_{proj} and the divergence angle θ_{div} in the distal end. Theoretically, the divergence angle θ_{div} is numerically equal to the acceptance angle θ_a.
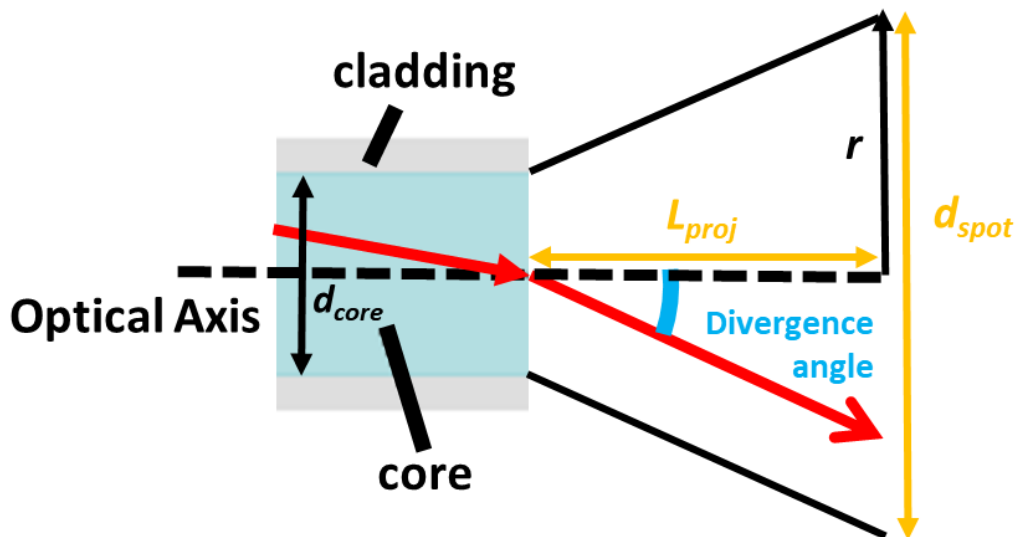
Fig 3.9　　Schematic ray diagram showing distal end of laser fiber without light collimation. Laser beam is departed with a divergence angle. Size of laser spot diameter d_{spot} depends on the divergence angle θ_{div}, fiber diameter d_{core}, and propagation distance L_{proj}.

3.4.1.3 Index Profile and Fiber Mode

Index profile is the distribution of refractive indices across the core and cladding of the fiber. Most laser fiber has a step-index profile in which the silica core has the highest refractive index than the cladding layer. Another kind of laser fiber has a graded-index profile in which the refractive index decreases gradually as a function of radial distance η from the fiber center. Both step-index fiber and graded-index fiber decreases the refractive index from the optical axis to its surface. However, the refractive indices of step-index fiber decrease abruptly in the medium interface, whereas the refractive indices of graded-index fiber decrease parabolically. The index profile function is shown as follow in **Equation 3.7**:

$$n(r) = n_1 \left[1 - \frac{\left(\eta \sqrt{A} \right)^2}{2} \right] \tag{3.7}$$

where $n(r)$ is the refractive index in a function of the radial position η from the optical axis (ranging from $-d_{core}/2$ to $+d_{core}/2$), n_1 is the highest refractive index in the optical axis and $\sqrt{A}$ is the gradient constant responsible for the parabolic profile. The following **Fig 3.10** shows some common types of index profiles for single mode and multimode fibers.
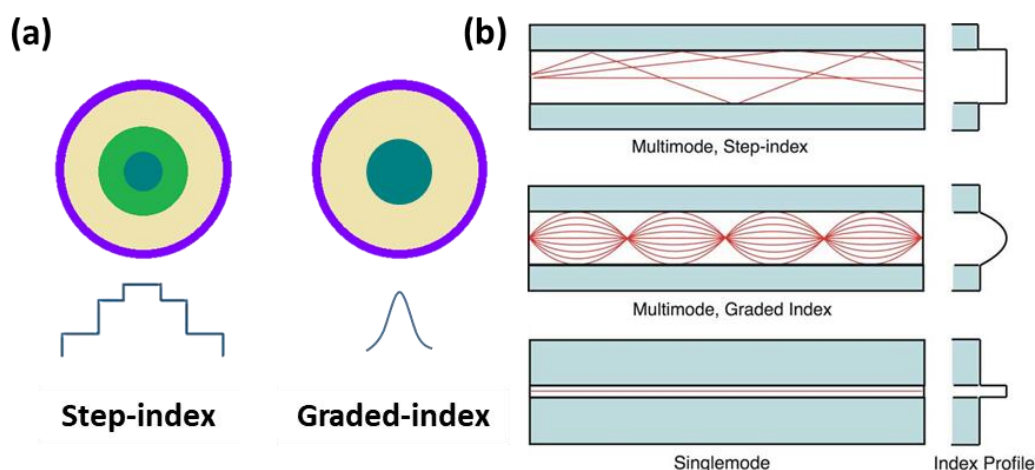
Fig 3.10   **(a)** Step-index and graded-index fiber showing distinct refractive index gradients. Graded-index fiber reduces the effect of modal dispersion. **(b)** Comparison of laser delivery pathway between single-mode and multi-mode. Multi-mode fiber transmits light rays with various incident angles, causing various combinations of ray travel path called modes.

There are two types of optical fiber, which are: **(i)** single-mode fiber and **(ii)** multi-mode fiber. Fiber mode describes light rays traveling with various

incident angles, causing various combinations of ray travel path called modes. For single-mode fiber, it carries the lowest order of mode as 0. Multi-mode fiber carries the higher order of modes. The number of modes depends on the fiber diameter d_{core}, fiber *NA,* and laser emission wavelength λ. For step-index multimode fiber, the number of modes N_{mode} is approximated in **Equation 3.8**:

$$N_{mode} = 0.5 \left(\frac{\pi d_{core} \times NA}{\lambda} \right)^2 \tag{3.8}$$

This formula only gives an approximate mode and does not work for fibers carrying a few modes. Single-mode fiber carries only one mode which travels in a straight line at the center of the core. Single-mode fiber has the smallest core diameter of about 10 µm. Meanwhile, multi-mode fiber has a relatively high core diameter of about 50 µm (Graded-index) and about 100 µm (Step-index). Fibers carry more than one mode at a specific light wavelength are called multimode fibers. Rays propagate in the fiber continuously only if they hit the core-cladding interface at an incident angle greater than the critical angle ($\theta_i > \theta_c$), which TIR occurs. For signal processing and propagation, graded-index fiber is more favorable as it reduces model dispersion. Reduction in model dispersion results in a coherent output signal for communication. In contrary, step-index fiber is low cost as it is easy to be fabricated. In our research, a laser fiber is used for power delivery means instead of signal transmission or communication. Therefore, the signal coherence is not required, as it will not affect the amount of energy transferred or *PD* of the laser spot. As a result, step-index fiber is chosen for this research for a low-cost robotic laser system.

3.4.1.4 Attenuation

Attenuation in laser fiber is a transmission power loss during light propagation. Attenuation in silica is very low as compared to another transmission medium such as copper and coaxial cable. Attenuation relates to the laser emission wavelength and fiber geometry. The power decays exponentially with traveling distance due to two types of power losses, namely **(i)** intrinsic fiber loss and **(ii)** macrobending loss. The intrinsic loss is governed by the absorption and scattering effects by the

transmission medium. The absorption and scattering effects are demonstrated along wavelengths of 700 - 1700 nm in **Fig 3.11a**. The scattering effect is dominant at shorter wavelengths and decays with wavelengths, whereas the absorption effect is significantly high in two specific wavelengths peaked at 1075 nm and 1400 nm. The intrinsic loss also includes the fiber coupling loss in the up-collimator to the laser fiber. Other than the constant intrinsic loss, macrobending loss is another major cause of attenuation. Macrobending loss occurs when the fiber is bent more than the critical radius relative to the fiber diameter, causing the condition of TIR fails [78]. For instance, when the incident angle no longer greater than the critical angle for TIR, the propagating ray will mostly be refracted in the boundary between the two media, causing cladding penetration and power loss shown in **Fig 3.11b**.
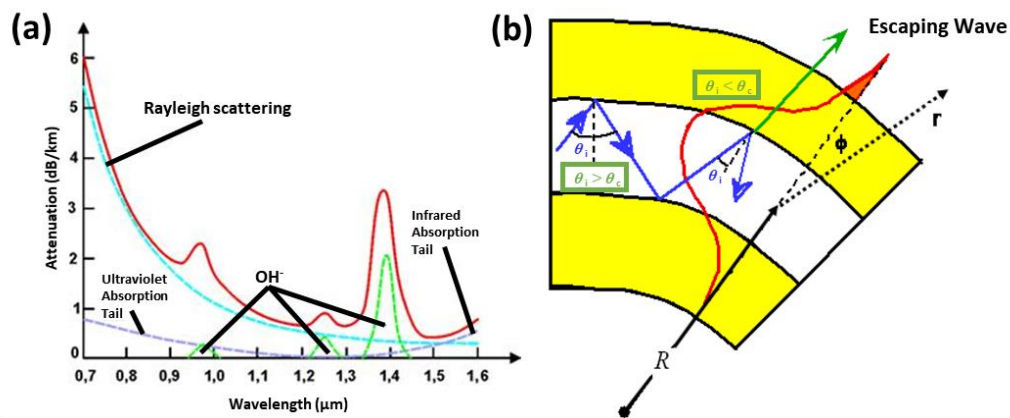
Fig 3.11 Attenuation in laser fiber causing transmission power loss during propagation. **(a)** Attenuation in laser fiber (red) for various transmission wavelengths. Major attenuation of laser fiber caused by Rayleigh scattering (cyan) and OH⁻ absorption (green). **(b)** Macrobend loss of laser fiber in bent configuration showing the path of escaping wave. Laser beam is escaped by refraction called when TIR criterion is not fulfilled (i.e., $\theta_i < \theta_c$). **Image Source: [79], INVOCOM**

3.4.2 Convergence of Laser beam

In **Equation 3.3** and **Equation 3.6**, the distal end of the laser fiber is assumed to be a blunt-tip fiber without light collimation. In this case, the laser beam will depart naturally with a divergence angle θ_{div}, which is numerically identical to the acceptance angle θ_a. For example, the laser spot diameter for 2-µm laser delivered by a 0.22 *NA*, 200 µm laser fiber is 11.48 mm with a projection distance L_{proj} of 20 mm given by **Equation 3.6**. The dominant factor for large spot diameter is due to scattering characteristics of the 2-µm laser. A focusing lens is necessary for collimating light into the optical fiber from the laser pumping source. Commercially

46

available laser fibers are specially engineered in the distal end to converge the resultant laser beam into a tiny laser spot to enhance *PD*. However, the cost of light convergence is the increase of laser tip diameter. Tip diameter strongly affects design parameters of the robotic steering system and should keep minimal for system miniaturization. In this section, we shall discuss three kinds of the microlens and their light converging properties. Diverging and converging microlens with different optical power will be investigated. The first approach is to add a distal microlens to the laser fiber end. There are two kinds of the microlens for laser fiber, which are converging and diverging lens. An example of the distal diverging microlens is Model FD1 (Frontal Light Distributor, Medlight) with 2 mm overall diameter and 10 mm rigid length (**Fig 3.12**). However, this device has a large divergence angle of 17.4° and is mainly used for photodynamic therapy to enhance the laser coverage area. Therefore, the required *NA* of the laser fiber depends strongly on the therapeutic application. For TLM, the laser spot diameter should keep minimal to reduce heat affected zone to the tissue and increase *PD* for specific tissue effect.
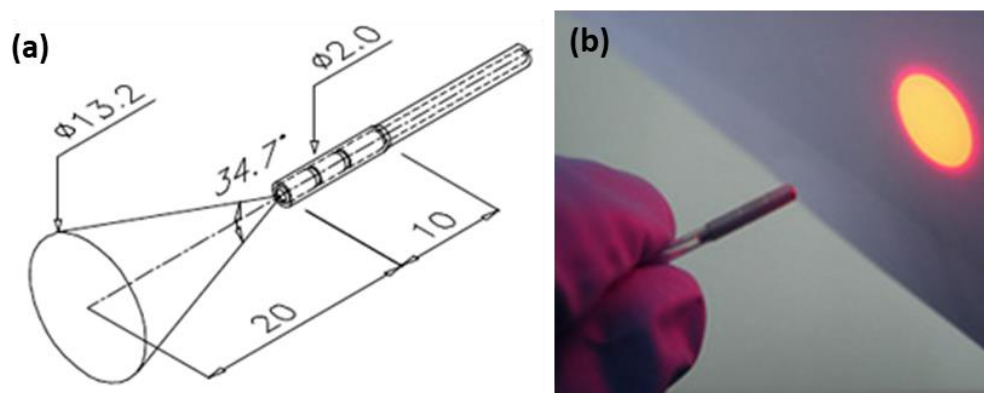
Fig 3.12   Diverging microlens system coupled to fiber distal end: **(a)** schematic diagram of diverging microlens system showing large projection spot size of 13.2 mm. Enlarged laser spot is caused by diverging property of the microlens with divergence angle of 17.4°. **(b)** Divergence microlens magnifying projection diameter of red-light spot. Increasing laser coverage area accelerates treatment time for photodynamic therapy. **Image Source: Frontal Light Distributor, Medlight**

With the specification of minimal spot diameter, converging microlens is required in this study. There are two approaches in the market, namely, miniature ball-tip and gradient-index (GRIN) lens. We shall discuss in terms of their optical power and converging effect. In addition, the rigid length for the light collimation is also proposed to keep minimal. One of the light-converging lenses is the miniaturized ball-tip microlens. Ball-tip fibers are used in laser lithotripsy introduced in 2016.

Ball-tip fibers from Boston Scientific (Flexiva TracTip 200, Massachusetts) has an overall diameter of 170 µm with minimal bending radius of 5 mm. The ball-tip is 300 µm in diameter, which is the largest dimension over the fiber. The minimum laser spot diameter is approximately 25 µm at a distance of 2 mm from the ball-tip [80]. The ball-tip laser probe is single-use and disposable, as the ball-tip will be burnt and degraded after the surgery shown in **Fig 3.13**.
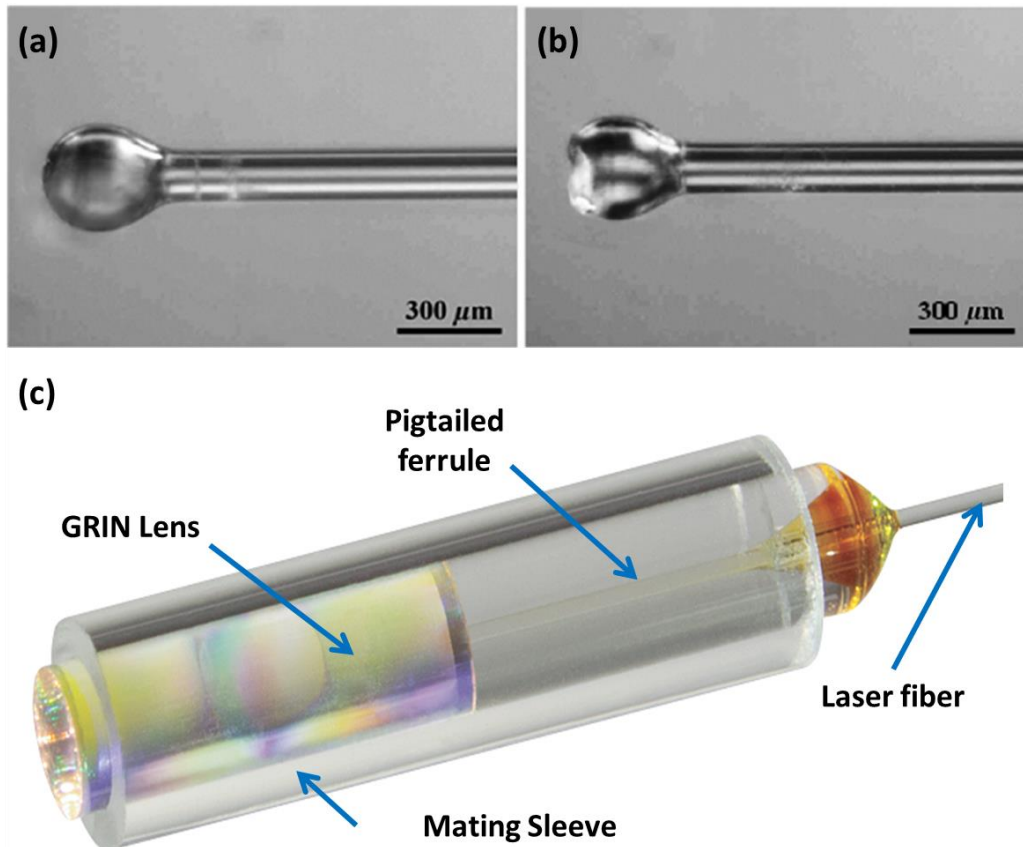
Fig 3.13   Converging microlens with various optical powers. **(a)** Ball-tip microlens with high optical power for kidney stone ablation. **(b)** Ball-tip microlens after ablation showing burnt microlens tip. **(c)** Structure of pigtailed GRIN lens encapsulated by mating sleeve. **Image Source: [80] and THORLABS Inc.**

Another type of converging lens is the GRIN lens. GRIN lens is designed to cater for a narrow band of wavelengths. Commercially, the wavelength is normally specified in a range from 600 nm to 1550 nm. The typical diameters of the GRIN lens are 1.8 mm and 2.8 mm with the mating sleeve (SMPF0215-FC, THORLABS) shown in **Fig 3.13c**. In a 10 mm rigid collimator, half of the rigid section is used for coupling the laser from the fiber to GRIN lens via pigtailed ferrule adapter. For multi-mode GRIN collimator in THORLABS, the fiber *NA* is 0.275 ± 0.015, which means the beam divergence angle of 15.96º without light collimation. However, beam divergence is reduced to less than 1.0º when coupled to GRIN lens.

Two kinds of converging microlens were evaluated by giving an 808-nm red-colored laser for visible-aid. A control test is performed with the free-end optical fiber with 0.22 *NA*. The selection of laser with a suitable ablation wavelength for head and neck cancers (HNCs) will be discussed in the **Section 3.4.3**. GRIN lens (HTOC-SM-808 Chongqing Hotfiber Technology) is purchased with specific design wavelengths for 808-nm (**Fig 3.14a**).

The ball-tip microlens, free-end fiber, and GRIN lens are placed in parallel to compare the light departuring effect (**Fig 3.14c**). Ball-tip microlens has the highest optical converging power. The light ray is intercepted in the near distance in 2 mm, causing the highest *PD* near the ball-tip. Beyond which, the light started to diverge after the interception point and caused lowing in *PD* with propagation distances. The control free-end fiber showed an angle of divergence of 13° in the air. Lastly, the GRIN lens showed a nearly parallel laser beam with an angle of divergence of less than 1°. In the case of the ball-tip microlens and free-end optical fiber, it illustrated that the scattering effect of light, which is not propagated in a pure straight line but some of the light rays curved outward.
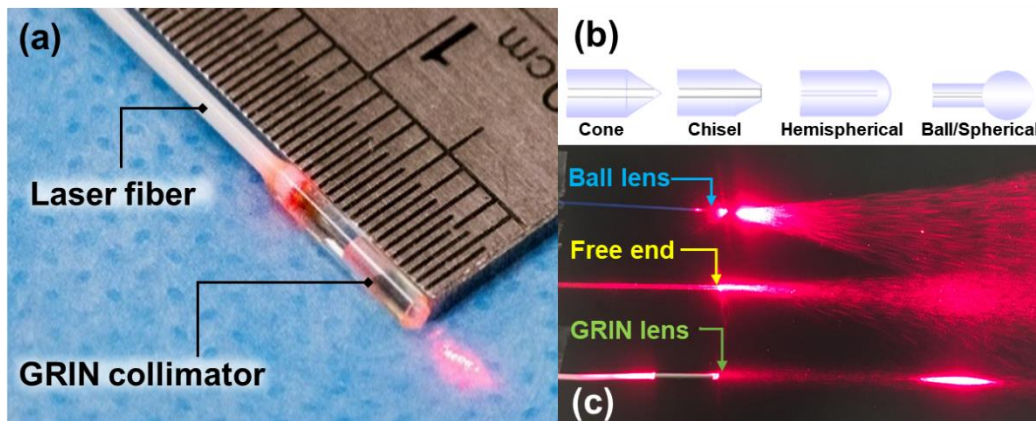
Fig 3.14 **(a)** GRIN lens (HTOC-SM-808 Chongqing Hotfiber Technology) pigtailed with laser fiber. Laser fiber has inner and outer diameter of 105 mm and 125 mm respectively. **(b)** Fiber tip modification differentiated by cone, chisel, hemispherical and ball shape. **(c)** Comparison between GRIN lens and ball lens. Free-end laser fiber is treated as a control setup with maximum divergence angle. GRIN lens shows relatively parallel beam compared with ball lens and free-end laser fiber.

Due to a high *PD* or high heat density in the frontal space (2 mm) of the ball-tip microlens, both tissue and microlens are vaporized. As a result, the ball-tip laser fiber is advertised as single-use and disposable due to its short lifespan. In this research, we aimed to have a mid-ranged laser with controllable intensity. It can establish a stable output *PD* for laser safety, minimizes the heat affected zone on the tissue and retains the microlens after surgery. In our study, the GRIN lens is more favorable.

3.4.3 Selection of Laser Wavelength

The choice of an appropriate emission wavelength of the laser depends on the interactive target chromophore, which affects the laser performance such as hemostasis property. In **Section 2.3.1.1**, only water has been investigated as the target chromophore as water is responsible for the most constitution in human. In this section, other target chromophores presented in the human body will be discussed. Apart from water, there are also blood, lipid, and melanin on the body surface. Selection of laser wavelengths depends significantly on the localized anatomy for the surgery, and all of the above substances are present in the ONP space. **Fig 3.15a** shows the characteristic peak representing the absorption coefficient for various target chromophore in human tissue. Data shows the optical absorption coefficient of water is generally lower than another absorption chromophore, with a magnitude of 1 - 100 cm^{-1} in 1200 - 1800 nm. Contrarily, fat, melanin, and hemoglobin have a higher absorption coefficient compared to water. In **Fig 3.15b**, it shows the normalized characteristic peak representing the optimal wavelength for each laser effect on human tissue. This shows the peak of melanin, hemoglobin, and fat appear at 200 nm, 420 nm, 930 nm respectively. The general ear, nose, and throat (ENT) laser mainly focused on the absorption of water. The damage is not specific to the cancerous cell. The laser dissection in ONP cavity aimed to avoid damage to the nervous system. Therefore, the selective laser targeting the cancerous cell is preferable for the TLM operation.
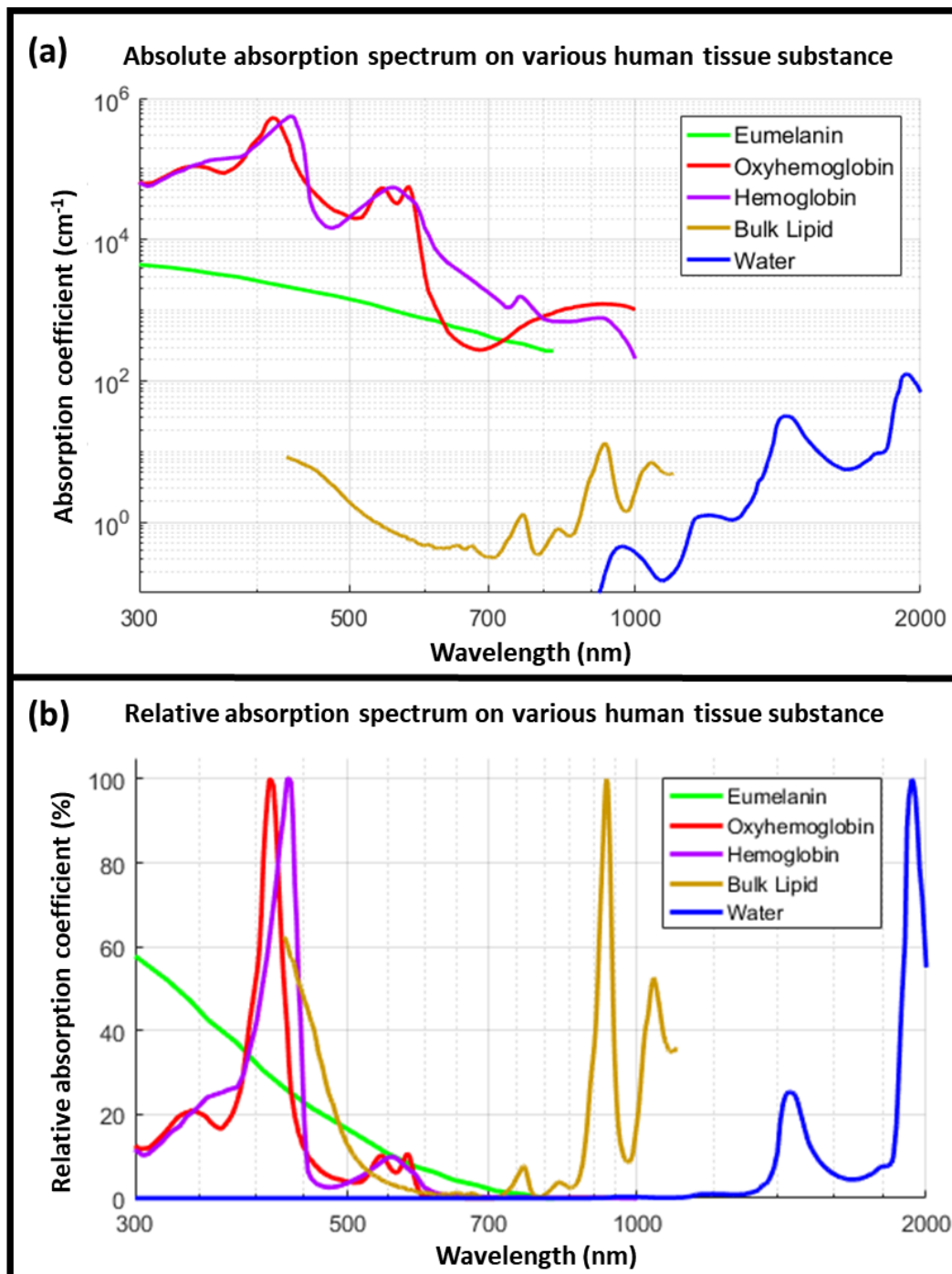
Fig 3.15 **(a)** Absolute absorption spectrum of various human tissue substances. Low absorption coefficients of water and lipid are measured with less than 100 cm^{-1}. **(b)** Relative absorption spectrum of various human tissue substances. Peaks of melanin, hemoglobin, lipid, and water are 200 nm, 420 nm, 930 nm, 1900 nm respectively.

A malignant tumor is an abnormal cell growth with high dependence on angiogenesis [81]. In the cancer cell multiplication process, a vascular blood network is built to supply nutrients and oxygen. As a result, the tumor region is a blood-rich area with a high absorption efficiency in a range of blue to violet

(300 nm to 600 nm). Research has been done for blue laser [82] with curing-unit for radiant heat treatments with power output of 700 mW. However, in the current ENT medical laser market, blue laser with high output power is not readily available. In **Section 3.4.4**, we will test some of the commercial medical lasers and evaluate their tissue effect with various wavelengths.

3.4.4 Tissue Dissection Test of Medical Lasers

As the testing protocol in this study will only perform in the *ex-vivo* tissues, which contains little blood content. Therefore, laser with wavelengths within the water absorption spectrum are selected. In this section, three types of lasers are tested, namely **(i)** 808-nm red laser (LASEVER, China), **(ii)** 980-nm KTP laser (WOLF, A.R.C. Laser, Germany), and **(iii)** 1470-nm infrared laser (WOLF, A.R.C. Laser, Germany). The non-visible medical lasers (i.e., 980-nm and 1470-nm lasers) are equipped with a green aiming beam for visual indication. The laser effect tests were performed on the *ex-vivo* pig tongue tissue. The laser dissection test on *ex-vivo* tissue is evaluated by three major criteria, which are: **(i)** degree of carbonization, **(ii)** dissection depth, and **(iii)** dissection width. 808-nm laboratory laser has a maximum power of 3.6 W, we used continuous wave (CW) mode to perform laser dissection. As the absorption effect of 808-nm laser on the *ex-vivo* tissue is not effective, prolonged exposure to high energy laser caused low incision depth but large dissection width of 2.3 mm (**Fig 3.16a**). The occurrence of carbonization and heat spread is due to inefficiency for tissue vaporization. The absorbed energy is then transferred to the peripheral tissues, causing high-temperature carbonization effect. As a result, a given thermal relaxation time is recommended with a laser pulse sequence instead of using CW. In **Fig 3.16b-c**, 980-nm and 1470-nm laser have also been tested. The result showed a little carbonization by 980-nm laser. 1470-nm laser even demonstrated much less carbonization. It is explained by the effectiveness of laser energy conversion for water vaporization. The incision depth in 1470-nm is also shallower than 980-nm. Normally, the penetration effect is more superficial in longer wavelengths, causing a deeper incision depth. However, this increasing trend stopped in the far IR spectrum (CO_2 laser), due to its high affinity for water [83]. It implied the 1470-nm laser has effectively vaporized the water and

the remaining new tissue surface are white in color as minimal heat transfer (or carbonization) to the peripheral tissues.

In conclusion for the laser selection, both 808-nm, 980-nm, and 1470-nm lasers are feasible for observable laser ablation. In addition, the tissue response is effective for the 1470-nm, which is closer to the water absorption peak beyond 2 µm. The 1470-nm laser is more favorable for the laboratory-based research experiment with little blood or hemoglobin in the testing tissue and phantom. Latest released new blue laser with higher power with 10 W (TrueBlue, A.R.C. Laser, Germany) is favorable to perform selective laser surgery in the future cases in the surgical scenario.
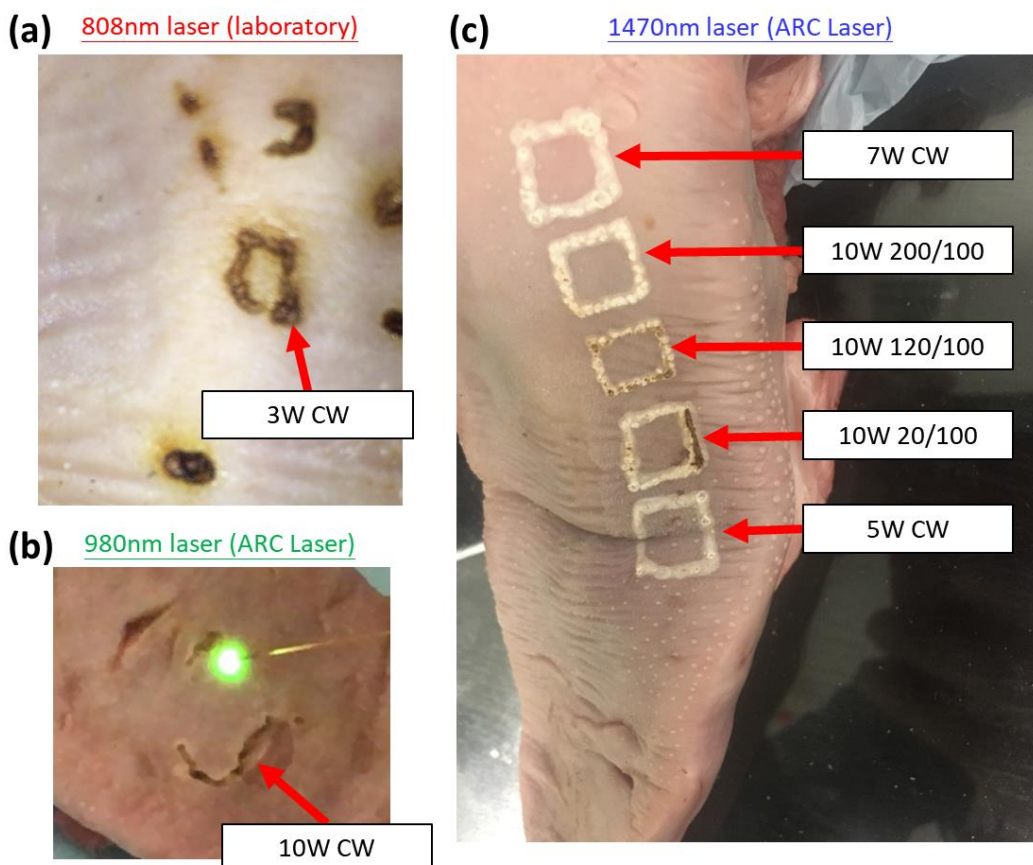
Fig 3.16   Laser test on *ex-vivo* pig tissue by three types of lasers. **(a)** 808-nm CW 3.6 W laser ablating dissection trace showing low incision depth and large dissection width. This implies low vaporization efficiency on the tissue by 808-nm laser. **(b)** 980-nm CW 10 W laser ablating thinner dissection width as compared to 808-nm laser. **(c)** 1470-nm CW 10 W laser showing minimal carbonization effect. Minimum heat is transferred to the peripheral tissues implying high vaporization efficiency. Modulated pulse sequences are also tested with 1470-nm test with duty cycle of 66%, 55%, and 17%. Higher duty cycle shows lower carbonization effect.

3.5 CONCLUSION

In this Chapter, a patient-specific dental guard is designed to replace the use of a conventional retractor system for minimal invasion to the patient. Dental guard stabilizes the jaw opening distance for 35 mm and maximizes the maneuvering space for the robot. The surgical constraint of the target ONP site is also evaluated by CT/MR images for both closed-jaw and opened-jaw configurations. A bending radius of 40mm is observed in an opened-jaw configuration. As a result, step-index multimode fiber is selected and coupled with a GRIN lens for laser dissection with projection distance for 10 - 20 mm. 808-nm, 980-nm, and 1470-nm laser are tested and proved to be feasible for laser testing on *ex-vivo* tissues.

<div align="right">

CHAPTER 4

</div>

<div align="right">

DESIGN AND OPTIMIZATION OF
SOFT ENDOSCOPIC LASER MANIPULATOR

</div>

4.1 INTRODUCTION

H AVING the static anchorage platform, a soft robotic system is designed for endoscopic navigation. The purpose of this Chapter is to introduce a soft robotic system that guides the laser fiber to dissect the cancer tumor. The navigating soft robotic actuator consists of hyperelastic material that can morphologically deform to steer the laser collimator to a designated target. In this Chapter, the feasibility of the soft robotic endoscopic is investigated. The first soft robotic prototype is fabricated by room-temperature-vulcanizing (RTV) silicone rubber molding. Overall size of the endoscopic prototype will be further miniaturized. The effect of strain wrapping in the soft robotic system is simulated through finite element analysis (FEA). Also, maneuverability is proved by a path following task in an intracavitary space.

4.1.1 Robot Endoscope for Laser Surgery

Conventional robotics composed of a rigid structure with a limited degree-of-freedom (DoF). They are controlled by integrated motors, which are vulnerable to water, heat, or uncertain damages. Research on the continuum robot has been done to enhance the robot dexterity by pre-curving concentric tubes in constant curvature [84-86]. Alternatively, soft robotics is a newly emerging concept. Recent advancement in soft robotics has attracted much research attention. The soft robot is composed of hyperplastic materials such as silicone rubber, latex, or resin. The end-effector of soft robot is free of electronic component, waterproof, heat-resistive and most importantly MR-safe. Compared to conventional robots, soft robotics can interact with humans in a safer manner and is compliant to any mechanical impact. Soft robotics was originated by the bio-inspired robot [87-94]. The inherent flexibility of a soft robot possesses with infinite DoFs theoretically and facilitates to work in a dynamic or unstructured environment. With the flexibility of the elastomeric material, soft robot enables many applications with safe human-robot interaction. Minimally-invasive surgery (MIS) can be one of the typical examples [95-97]. Taking references of recent endoscopic laser research, Renevier [98] suggested a rectangular column robot with a dimension of $11 \times 9 \times 42$ mm^3. This FP7 European funded medical robot is called MICRORALP (μRALP). μRALP aimed for intuitive and flexible endoluminal endoscopy (**Fig 4.1**). μRALP consists of a mirror pan-tilt system actuated by linear piezoelectric motors (squiggle motors) with a 6 mm stroke length. The square mirror is electrodeposited with a thin (0.2 mm) gold layer. The coupling mirror system has a maximum angular deflection of 45º. When the mirror is placed at 20 mm apart from the targeting tissue with a 30º mirror tilting angle, it provides a scanning area of 20×20 mm^2 on the tissue. The accuracy performance is evaluated by a path-following spiral test with a root-mean-square (RMS) error of 88 μm. The integration of miniature linear piezoelectric motors ($2.8 \times 2.8 \times 6$ mm^3) is critical for deflecting the light ray in a small scale (< 15 mm). Even though they deployed laser fiber in the study, but the robot was still intrinsically rigid in a cuboid shape and vulnerable to water due to the presence of piezoelectric motor.
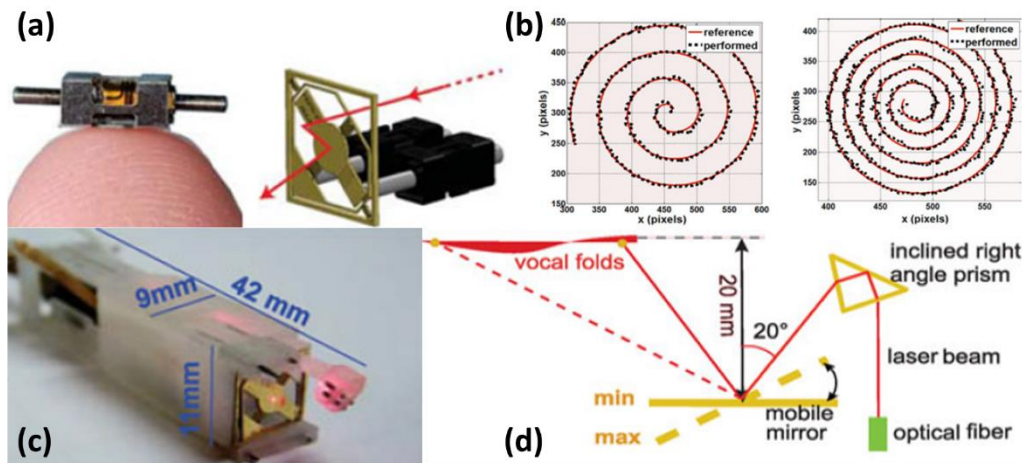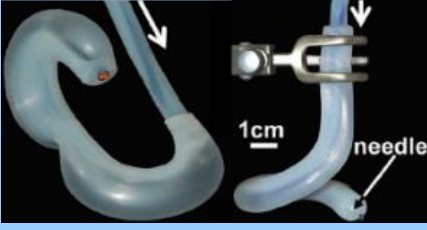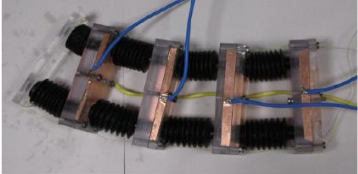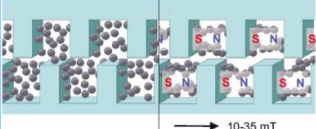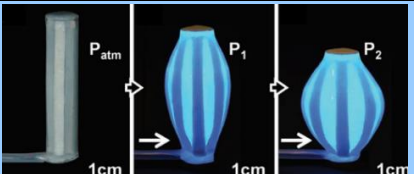
Fig 4.1   µRALP system developed for endoscopic transoral laser surgery. **(a)** Miniaturized squiggle motor assembled with gold-electrodeposited mirror. **(b)** Performance evaluation test by path following task in spiral shape with a speed of 2.25 pixels/s. **(c)** Prototype of µRALP system ($11 \times 9 \times 42$ mm^3) integrated with optical laser fiber. **(d)** Kinematic model of µRALP projecting laser beam onto the vocal folds.

4.1.2 Recent Works in Soft Robotics

The soft robots are controlled by tendon-driven or fluidic actuation. Some research has been done with the combustion of premixed methane/oxygen [99]. Rather than articulate and bend in fixed reference joint, soft robots change their forms by elastic deformation to perform various functions, such as bending, twisting, elongation, and retraction (McKibben actuator) [100]. The challenge for the soft robot is the robustness of the manipulator. Soft robot without reinforcement feature results in low controllability and accuracy. For example, cyclical vacuum-actuated machine (cVAM) (**Fig 4.2**) could only perform a simple bending and stirring action, but not a precise actuation for end-effector control [101, 102]. Soft rotary actuator is also improved by an origami shell reinforcement for enhanced maximum pressure and output torque [103]. Fiber reinforcement [104-106] and paper reinforcement [107] approaches are used to improve the robustness of soft robotics. Controllable stiffness has also been done for soft robots by granular jamming [108, 109], electrorheological fluid (ER fluid) [110], dielectric [111] and shape memory alloys (SMA) [92]. Stiffness control mechanics can be achieved by varying pressure, electrometric field, and temperature. Various actuation methods of the soft robotic devices are sorted in **Table 4.1** by their fluid types and reinforcement modality.

57

Table 4.1 List of soft robotic actuators with three major actuation methods

Device	Actuation Modalities	Detail / Performance
Fluidic Actuators without reinforcement		
Robotic Tentacles with three pneumatic chambers [112]	Pneumatic actuation	
Soft robots with a pneumatic network (Pneu-net) [113]	Pneumatic actuation	
Tripedal Pneu-nets with a tripedal configuration [99]	Methane/Oxygen gas combustion	
Continuum arm with ER valves controlling segments flexibility [110]	Tendon-driven, Electro-rheological (ER) fluids	
Tunable stiffness in the chamber with ribbons surface [114]	Magneto-rheological fluid	
Fluidic Actuators with fiber/paper reinforcement		
Fiber-reinforced soft bending actuator [104]	Pneumatic actuation, Fiber strain wrapping	
Fiber reinforced elastomer enclosures (FREEs) [106]	Pneumatic actuation, Fiber strain wrapping	
Composite/paper reinforced elastomer [107]	Pneumatic actuation, Paper strain wrapping	

Fluidic Actuators with granular jamming

Universal robotic gripper [109]	Vacuum Pressure	
Jammable Manipulator [108]	Vacuum Pressure, Tendon-driven	
Jamming Skin Enabled Locomotion (JSEL) [115]	Vacuum Pressure, Pneumatic actuation	
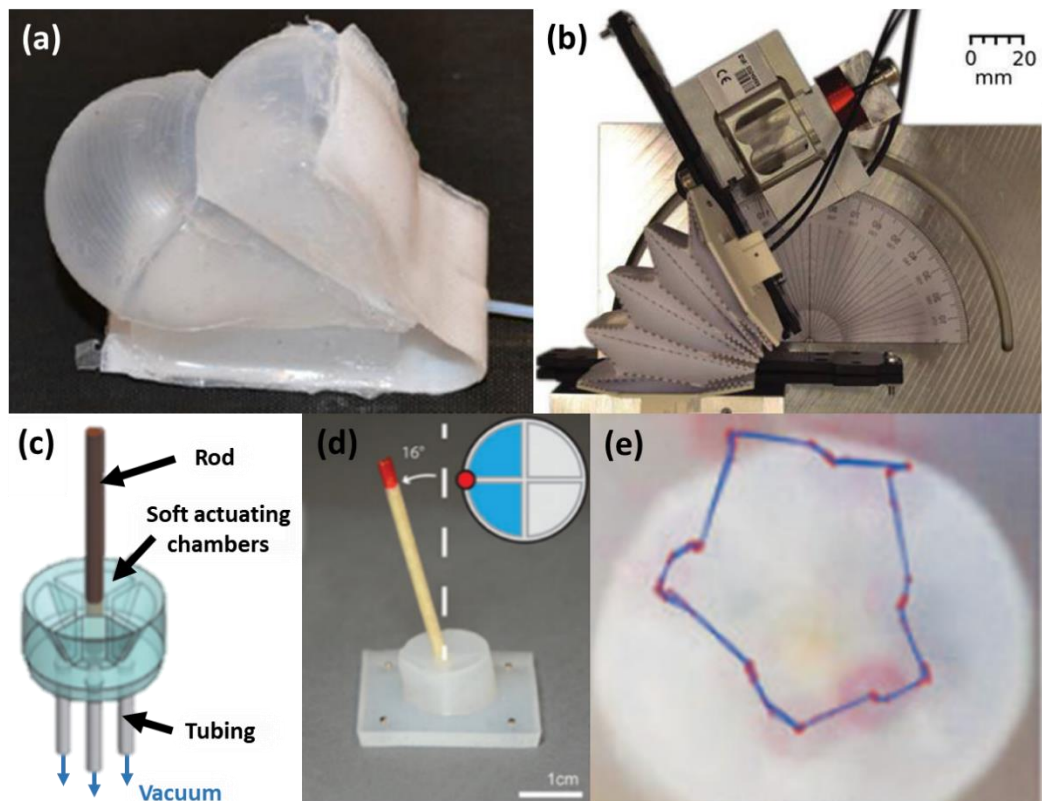
Fig 4.2 **(a)** Soft pneumatic actuators (SPA) made of silicone rubber actuating in 25 kPa. **(b)** Rotary SPA with origami shell reinforcement actuating in 45 kPa. **(c)** Cyclical vacuum-actuated machine (cVAM) actuated by negative pressure. **(d)** Steering rod deflecting with 16° bending angle. **(e)** Movement of tip position with five actuation chambers in 10 steps. **Image Source: [101-103]**

4.2 POTENTIAL FOR SOFT MEDICAL ROBOT FOR SURGICAL USAGE

In the 20th century, MIS started to replace traditional open surgery, which revolutionizes the treatment modality in the operative medicine. Advancements in the MIS technique outweigh the shortcomings of open surgery by reducing trauma and enhancing cosmetic effects. With the dexterity and flexibility of soft robotics, their strength will again revolutionize the MIS scenario. Newly emerging surgical soft medical robotics systems have opened a new era of MIS. For example, STIFF-FLOP and Endotics® are a soft robotic surgical system which opens a new page of natural orifice transluminal endoscopic surgery (NOTES). Both soft medical robots have pushed their limit in reducing their overall diameter down to 18 mm.

4.2.1 STIFF-FLOP

One of the surgical examples of soft robotic system is STIFF-FLOP, which is "STIFFness controllable Flexible and Learnable manipulator for surgical OPerations" (**Fig 4.3**). STIFF-FLOP [96, 116] enables interaction with soft organs by changing its stiffness with granular jamming. The first single-port soft robotic surgery had been performed in human on Oct 2015. Even the size of STIFF-FLOP is reducing from 25 mm to 15 mm, the diameter is still undesirable to be used in the confined space such as oral, nasopharyngeal (ONP) cavity.
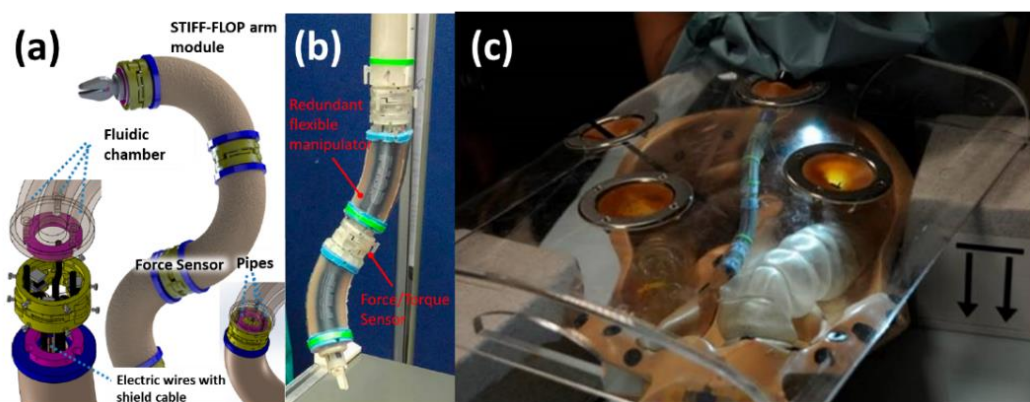
Fig 4.3   Example of surgical soft robotic system. **(a)** STIFFness controllable Flexible and Learnable manipulator for surgical OPerations (STIFF-FLOP) arm wiring with shield cables and fluidic chambers. **(b)** STIFF-FLOP integrated with force/torque sensors. **(c)** Two segments of STIFF-FLOP maneuvering inside abdominal stimulator. **Image Source: [117], STIFF-FLOP**

Despite large in scale for STIFF-FLOP, strain-wrapping reinforcement enables a potential breakthrough for soft robotics regarding accuracy and robustness. The reinforcement approaches are applied to the **(i)** individual chamber with helical thread constraint [118] and **(ii)** overall bellow constraint on the outside [119].

4.2.2 Endotics® System

The soft robotic endoscope also has a potential application on colonoscopy [120] with its compliance and dexterity to interact with human intestines. Endotics® system [121, 122] is a new robotic device composed of a working channel with a biopsy instrument (**Fig 4.4**). It is employed as a pilot study for early detection of colonic polyps. It is another example of surgical robotics system by using soft robotic technology. With the intrinsic properties of the soft robot, the surgery is basically sedation-free and is a safe procedure. Endotics® system offers an endoscopic camera with illuminations. The diameter of the Endotics® system is 18 mm. It is only desirable for colonoscopy but not in ONP cavity. Miniaturization of the soft robotic system needs to be further investigated.
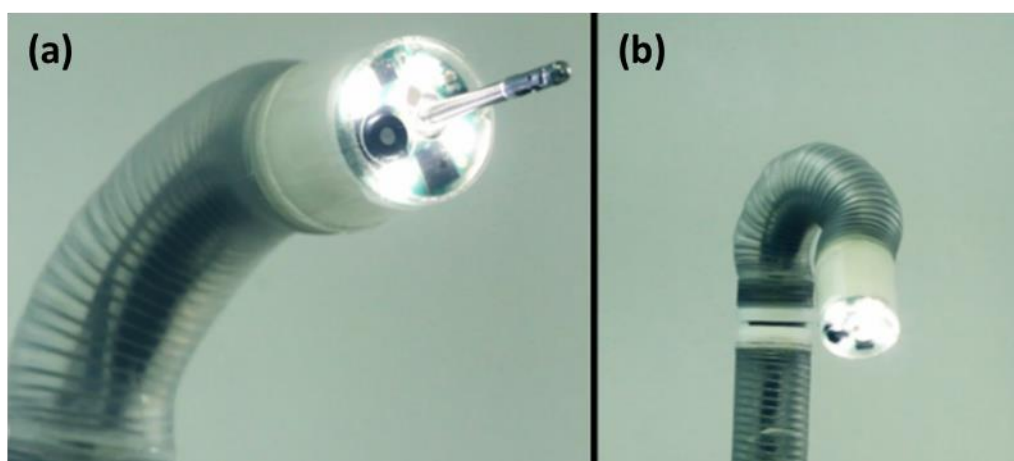
Fig 4.4   Endotics® soft robotic system equipped with LED and endoscopic camera. **(a)** Endotics® bent with integrated biopsy forceps. **(b)** Endotics® system achieved a maximum bending of 180°. **Image Source: Endotics® System**

4.2.3 Prototype of Soft Robotic Endoscope

Emerging technology of soft medical robot enables a new era for surgical robotics. The size of STIFF-FLOP and Endotics® have kept in a range of 15 mm to 25 mm in terms of their diameter. In this section, a soft robot made of RTV silicone rubber (Ecoflex® 0050, Smooth-on Inc.) is designed within 15 mm and fabricated to evaluate the proposed framework for endoscopic navigation. The soft robot endoscope will be further miniaturized in **Section 4.4**.

The soft robot comprises three cylindrical inflatable chambers. Each chamber is wrapped by a helical Kevlar string layer with a pitch of 1 mm. This fiber constrained structure is first proposed by Suzumori [123, 124], in which the helical constraint enforces axial expansion of inflatable chambers. The anisotropic behavior generates an effective elongation and bending moment when subject to pressure input. Three fluidic chambers can be individually actuated by air or other fluids, facilitating a panoramic workspace with a bending angle of more than 150º. The slender robot configuration with 13 mm in outer diameter and 93 mm in length are also compatible with conventional colonoscopes. Fabrication of the soft robot prototype involves three major phases:

- **(i)** **Phase I:** Three cylindrical air chambers are cast with RTV silicone rubber (Ecoflex® 0050) in the inner molds.
- **(ii)** **Phase II:** Kevlar strings are wrapped densely in a single helical structure along each soft chamber.
- **(iii)** **Phase III:** Additional layers of RTV silicone rubber (Ecoflex® 0050) are cast to house the three inflatable chambers into one. This layer also fixes the strings from dislocation.

4.3 FINITE ELEMENT ANALYSIS (FEA) OF SOFT ROBOTIC MANIPULATOR

In this research, hyperelastic materials are utilized for fabricating soft robotic. Hyperelastic material with an elongation at break of more than 200% are selected to be used as the composition material for the extension chambers. This hyperelastic material is made of silicone rubber and thus MR-safe, as it is chemically inert and metallic-free. Hyperelastic models from other literature are used to formulate the mathematical model in FEA.

4.3.1 Design of Soft Robotic Endoscope by FEA

Research has been done on the FEA for the soft robots [125, 126]. Characterization of material is required before simulation. Among all choices of materials, RTV silicone rubber is commonly used in soft robotic research. Literatures has investigated a best-fit model to formulate the hyperelastic model for the silicone rubber (Ecoflex® Series, Smooth-On, Inc.). Best fit models for Ecoflex® 0030 and Ecoflex® 0050 have been evaluated [127]. For Ecoflex® 0030, the best constitutive model is proved to be the Yeoh model with reduced polynomial model (N = 3), with parameter values of $C_{10} = 5.072 \times 10^{-3}$, $C_{20} = -0.331 \times 10^{-3}$, and $C_{30} = -0.015 \times 10^{-3}$. Moreover, the best constitutive model for Ecoflex® 0050 is proved to be Ogden model (N = 3), with parameter values of $\alpha_1 = 1.55$, $\alpha_2 = 7.86$, $\alpha_3 = -1.91$, $\mu_1 = 107.9 \times 10^{-3}$, $\mu_2 = 21.47 \times 10^{-6}$, and $\mu_3 = -87.1 \times 10^{-3}$. The units for C_n and μ_n are MPa and α_n are dimensionless. The characteristic curve of six hyperelastic models are plotted by stress-stretch curves (**Fig 4.5**) [128, 129], where stretch λ is defined by the ratio between the true length l and the natural length L_0 of the elastomer. Therefore, stretch has a relationship with strain ε of:

$$\lambda = \varepsilon + 1 \tag{4.1}$$
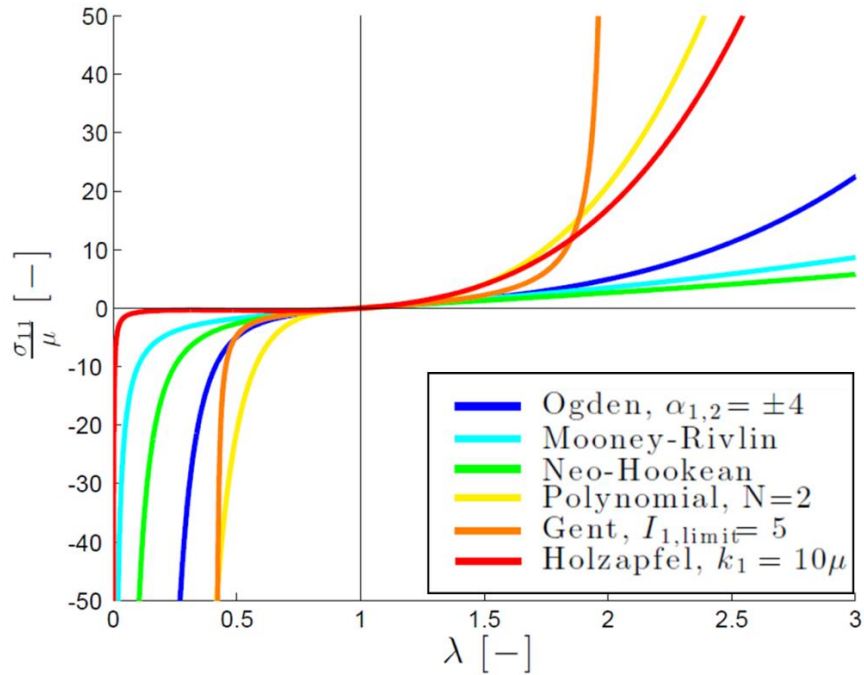
Fig 4.5   Uniaxial tension/compression characteristic stress-stretch curve for six hyperelastic models. Six hyperelastic models, namely Ogden, Mooney-Rivilin, Neo-Hookean, Polynomial, Gent, and Holzapfel model, are plotted with a same slope at $\lambda = 1$ for all models. **Image Source: [130]**

In this research, Ecoflex® 0050 is employed to fabricate the soft robotic manipulator consists of three inflatable chambers (**Fig 4.6**). Each chamber is constrained by strain wrapping approach in a transversal plane. Strain wrapping technique helps to attain anisotropic expansion along axial direction upon chamber pressurization. A full paranoiac motion can be achieved by regulating the inflation pressure of each chamber. The soft manipulator is actuated by three separable power-screw fluidic cylinders with volumetric control. A volumetric control system with pressure feedback is implemented for the setup. During the experiment, various pressure combination of three individual chambers are actuated, and soft manipulator is driven to the designated position. The comparison of the simulation results and the real model are presented in **Fig 4.7**.
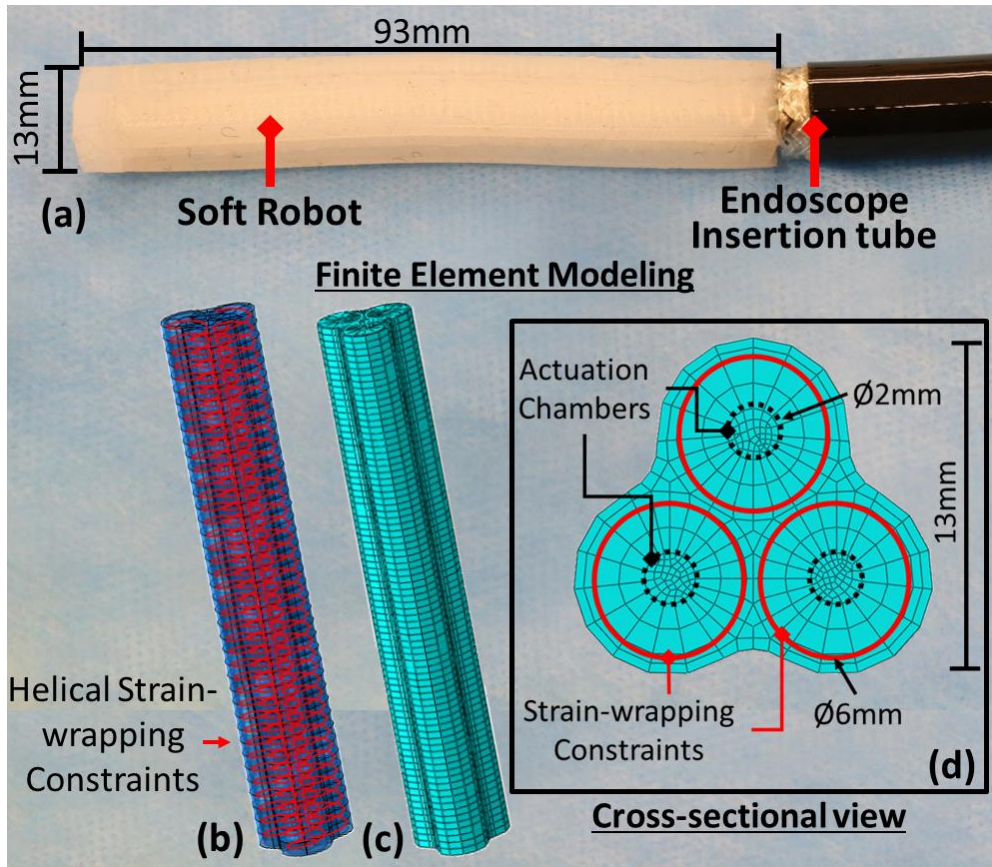
Fig 4.6 **(a)** Soft endoscope prototype made of silicone rubber. Prototype assembled with endoscopic insertion tube shows comparable diameter to conventional endoscope. **(b)** CAD/CAM Abaqus model of soft manipulator with strain wrapping. Anisotropic expansion is implemented by applying individual helical constraints. Strain wrapping constraints are modeled as linear trusses. **(c)** Finite element (FE) model tessellated with 12,000 linear hexahedron elements. A total of 2,214 truss elements are defined to emulate the effect of strain wrapping constraint. **(d)** Cross-sectional area tessellated by hexahedron meshing. Soft endoscope prototype has an overall diameter of 13 mm.
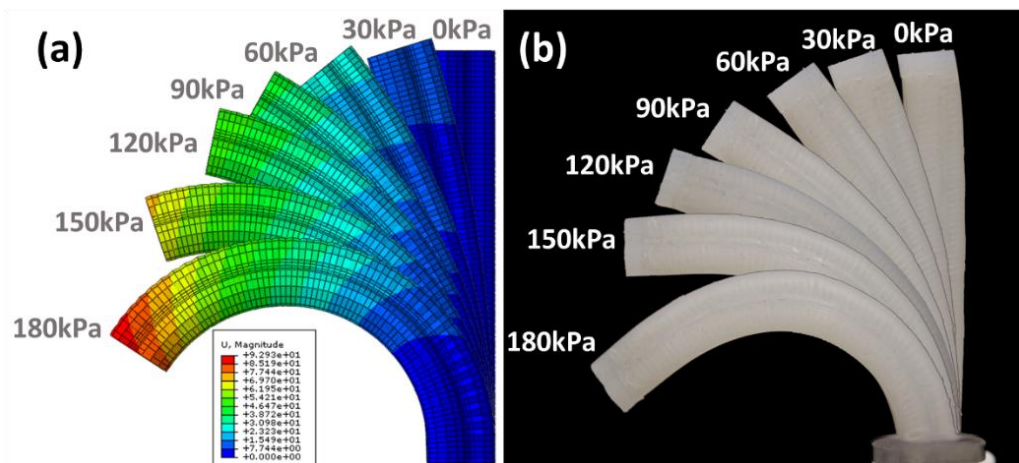
Fig 4.7 Comparison of bending characteristics between FE model and actual prototype. **(a)** FE simulation of single chamber inflation with seven pressurization levels with 30 kPa interval. **(b)** Actual deformation characteristics exhibiting similar configurations under corresponding pressure levels.
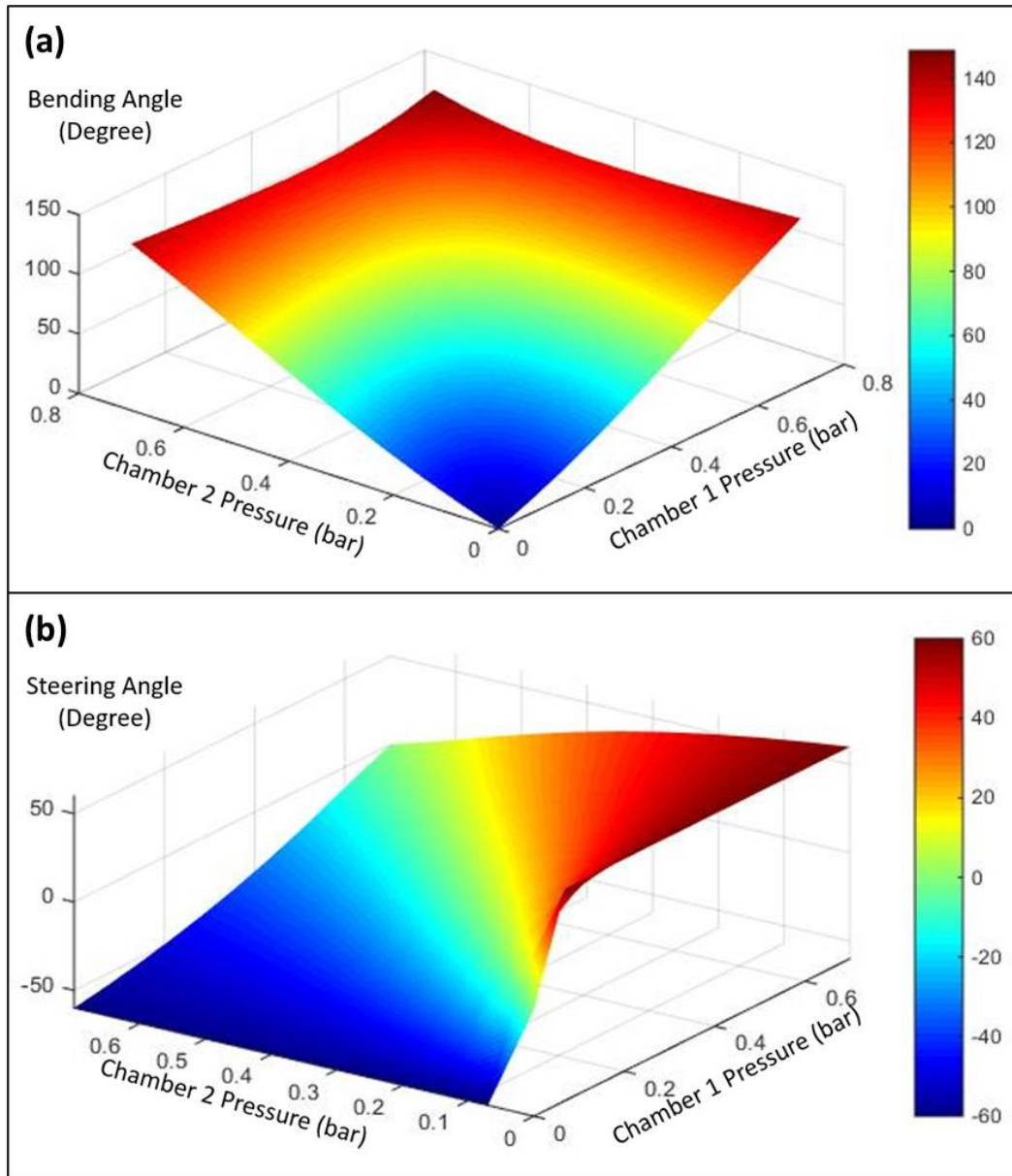
Fig 4.8   Predicted kinematic model of soft robotic prototype by FEA. Simulated pressures are applied to two adjacent chambers. **(a)** Bending angles and **(b)** steering angles are determined by FEA and illustrated by a color map.

Results of finite element (FE) simulation shows the bending angles and steering angles upon inflation are presented in **Fig 4.8**. Actuation effect of each individual chamber is complementary to the combined effect of other two. As the three-chambered model is rotationally symmetric, the sample points for the determination of the kinematics in the whole paranoiac workspace can be collected by FE simulation of inflating two actuation chambers only. The positions and normal directions of the end-effector are recorded by electromagnetic (EM) tracking markers (**Fig 4.9**). The current position of the soft manipulator end-effector is used for the Jacobian estimation. The soft manipulator traces the trajectory in virtual

camera perspective by controlling the actuation pressures. During the experiment, we validated the robotic projection tip to follow the proposed trajectory with an RMS error of less than 6 mm on the projection surface.
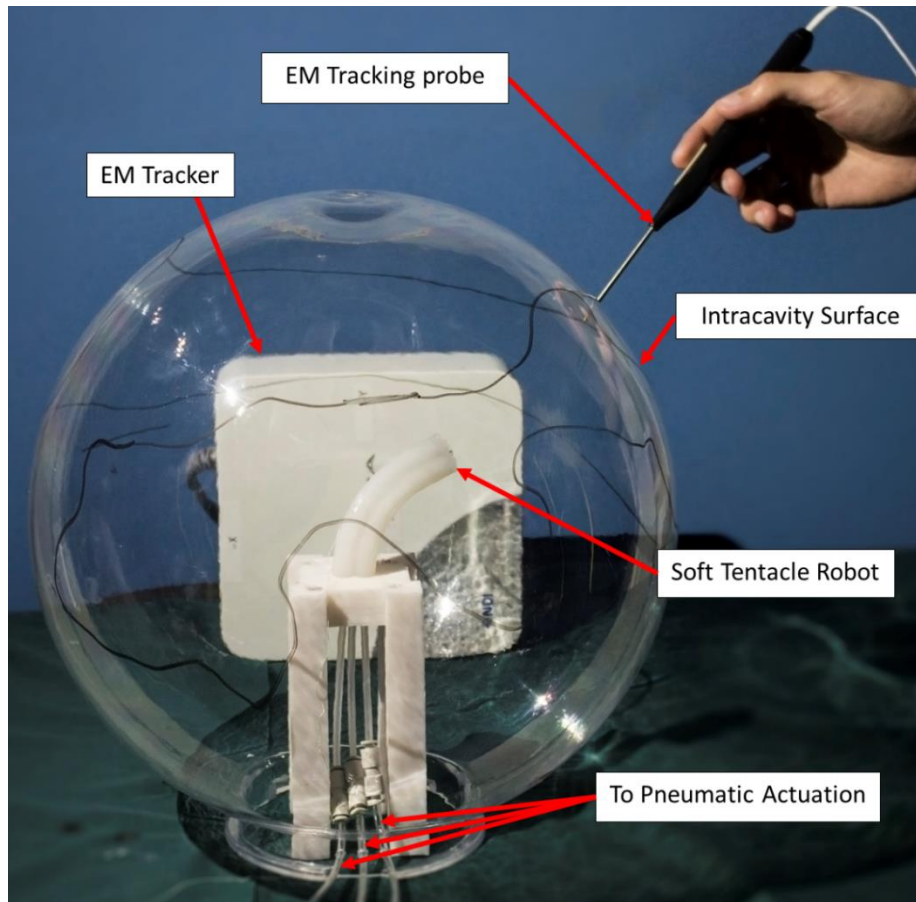
Fig 4.9   Spherical intracavity scenario for endoscopic navigation experiment. Soft tentacle robot is controlled by applying differential pressures to three fluidic chambers. Desired trajectory is pre-registered on the intracavity surface (transparent sphere shell) by using an EM tracking probe. End-effector position is monitored by the same EM position tracking system to validate trajectory tracking accuracy.

4.3.2 Evaluation of Soft Robotic Endoscope

In this Chapter, I have proved the feasibility of soft robotic manipulator with strain wrapping reinforcement and gained high accuracy with RMS error of 6 mm. Even though this prototype has reduced to 13 mm in diameter, which is smaller than STIFF-FLOP and Endotics®, it does not possess of any instrument channel. In addition, the overall length of the manipulator is lengthy (93 mm). As a result, in **Section 4.4**, the possibility of miniaturization for the soft robotic manipulator will be further discussed and investigated to reduce the overall length of the bending actuator down to 40 mm. With the advantages of strain wrapping reinforcement, new miniaturized soft robotic design gains higher controllability and robustness.

4.4 MINIATURIZATION OF SOFT ROBOTIC ENDOSCOPIC LASER MANIPULATOR

With the success prototyping of the soft robotic endoscopic for intracavity navigation, I proposed to further miniaturize the endoscopic design by another fabrication modality, which is additive manufacturing. In addition, the dexterous soft robotics design with two modules of STIFF-FLOP significantly enhanced the coverage workspace [131]. As a result, a modular soft robotic laser manipulator with two segments is proposed. Unlike STIFF-FLOP, our two segments design has specialized functions for each part, which govern the macroscopic steering and microscopic laser fine-bending. In the following section, I proposed the miniaturization of two reinforced soft robot (RSR) actuators with coarse steering (cRSR) and fine bending (fRSR). In addition, a working channel is reserved for the laser collimator and laser fiber to accommodate. The kinematic actuation workspace of the overall robotic system is tested and evaluated.

4.4.1 Prototype of Reinforced Soft Robots (RSRs)

A cRSR prototype is fabricated with a shortened length of 30 mm by RTV molding of silicone rubber (**Fig 4.10a**). The result shows that the robot workspace requires 20 mm in lateral distance for bending angle of 45°, this range is within the maximum retracted width between two tonsillar pillars. However, further miniaturization is required on this design for a better robot maneuvering. It is found that RTV molding and overall strain wrapping cost a lot of design workspace. Another fabrication modality with high spatial efficiency to pack the reinforcement layer onto the elastomeric chamber is required for the miniaturization. Three-dimensional (3D) printing is one of the options to achieve the abovementioned objective by applying multiple printing materials into a single model. The fRSR prototype is designed with a fluidic actuated pan-tilt mechanism (**Fig 4.10b**) with references on the laser scanning system and pivot mechanisms [132-134]. The laser collimator is embedded inside the fRSR and is steered by pressurizing fluidic chambers in the semi-spherical actuation system. The fRSR is designed with the following parameters (**Fig 4.10**) shown in **Table 4.2**.
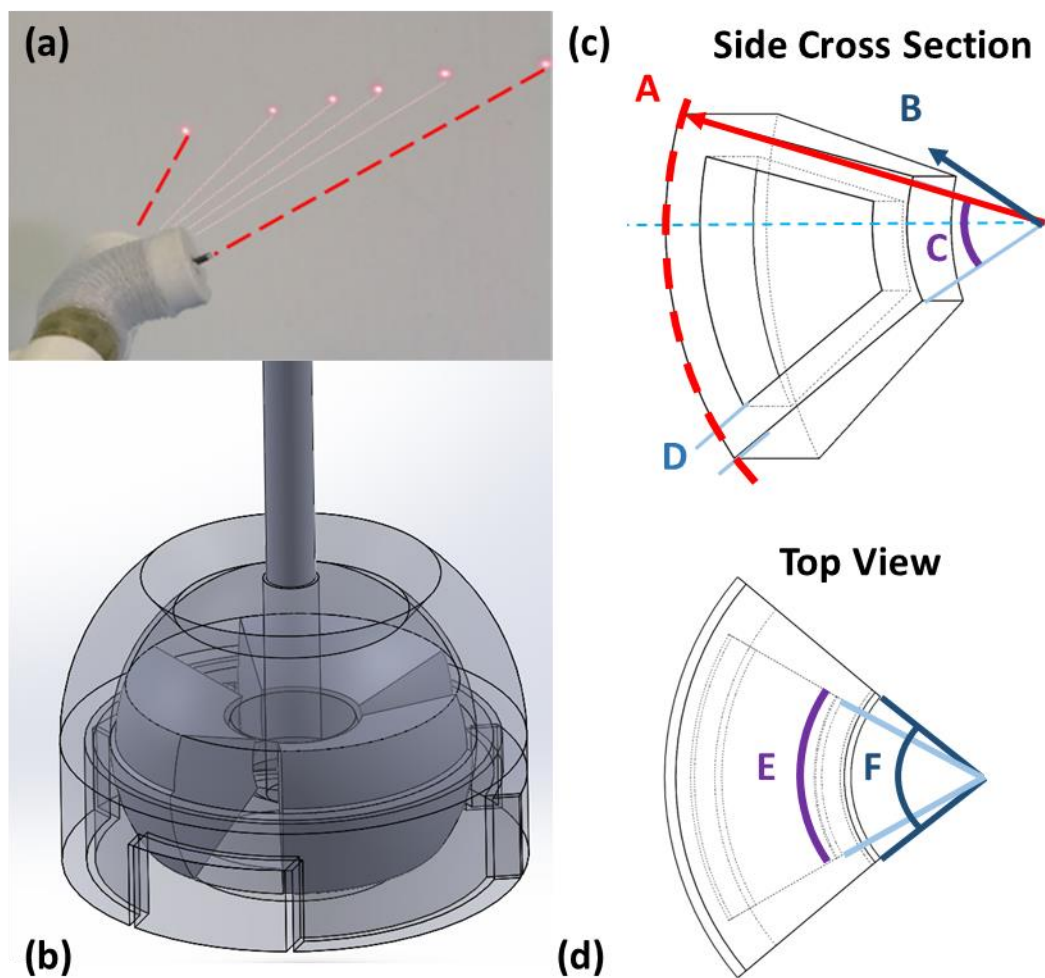
Fig 4.10 Miniaturized reinforced soft robot (RSR) prototypes. **(a)** cRSR actuator with ø = 14.26 mm steering laser collimator and emitting a low-intensity parallel beam. **(b)** fRSR actuator with soft fluidic pivoted mechanisms. **(c)** Side view and **(d)** Top view of fRSR showing design parameters of fluidic chamber.

Table 4.2 Design parameters for the elastomeric chambers for fRSR prototype

Coding	Chamber Parameters	Detail
A	Outer Diameter	6 mm
B	Inner Diameter	2 mm
C	Vertical Rotary Angle	50º
D	Thickness	0.3 mm
E	Horizontal Inner Sweep angle	40º
F	Horizontal Outer Sweep angle	60º

4.4.2 Role of Three-Dimensional Printing (3D Printing)

Three-dimensional (3D) printing can be utilized as a technique to mimic patient-specific models with biologically accurate material for realistic procedural planning and simulation. For example, 3D printing recreates the anatomical structure of the patients' left atrial appendage (LAA). By using 3D-printed simulated LAA for procedural planning, an optimal watchman size for specific patient occlusion is evaluated. In addition, 3D printing can also be used in thoracic endovascular aortic repair (TEVAR). By installing sensitive pressure sensors along the 3D printed aortic wall, we can estimate the deformation during the deployment of the aortic metallic stent. Last but not least, 3D printing can also be used for the surgical procedure, such as a dental fixture in oral and maxillofacial that is used to perform surgery with patient-specific apparatus. Other than procedural planning and simulation, 3D printing can assist to print molds for casting silicone rubber-based actuators (e.g., Ecoflex®, Dragon Skin®, and Elasosil®). 3D printing can also directly fabricate the soft robotic prototype using multi-material printing technology. Most of the research fabricated soft robotic device by silicone molding, whereas a few research deployed 3D printing to directly build the soft robot [135-137]. Direct 3D printing accelerates the rapid prototyping process and enables to produce a more complex robotic structure and reduces fabrication difficulty. With the advanced technology of digital printing by Stratasys (Objet 350, Connex3, Stratasys), it enables to construct a hybrid hard and soft robotic system. The hybrid body can be composed with the elastomer (TangoBlackPlus™ and AgilusClear30™) and stiffer material with the same mechanical properties (VeroClear™ and MED610™) for strain wrapping reinforcement.

Unlike current transoral robotic system (TORS), direct 3D printed surgical robotic system is fabricated with low setup cost and is aimed to be disposable. The surgical device is printed with MED610™, which designs to be bio-compatible (prEN ISO 10993-1:2017) with short-term mucosal-membrane contact of up to 24 hours. This reduces the complication of preparation process which also involves ethylene oxide (EtO) sterilization. According to the datasheet, the printed robotic system can be steam sterilized at 132 °C in four minutes by an autoclave cleaning system.

4.4.3 Material Selection for Soft Robot Fabrication

Existing laboratory-based technologies for soft robot fabrication are silicone rubber molding and direct 3D printing. Apart from the hyperelastic models fitted for silicone rubbers, the hyperelastic characteristics of the 3D printed elastomers also need to be tested and evaluated. In this section, tensile tests will be performed to determine the elastic modulus and the material properties.
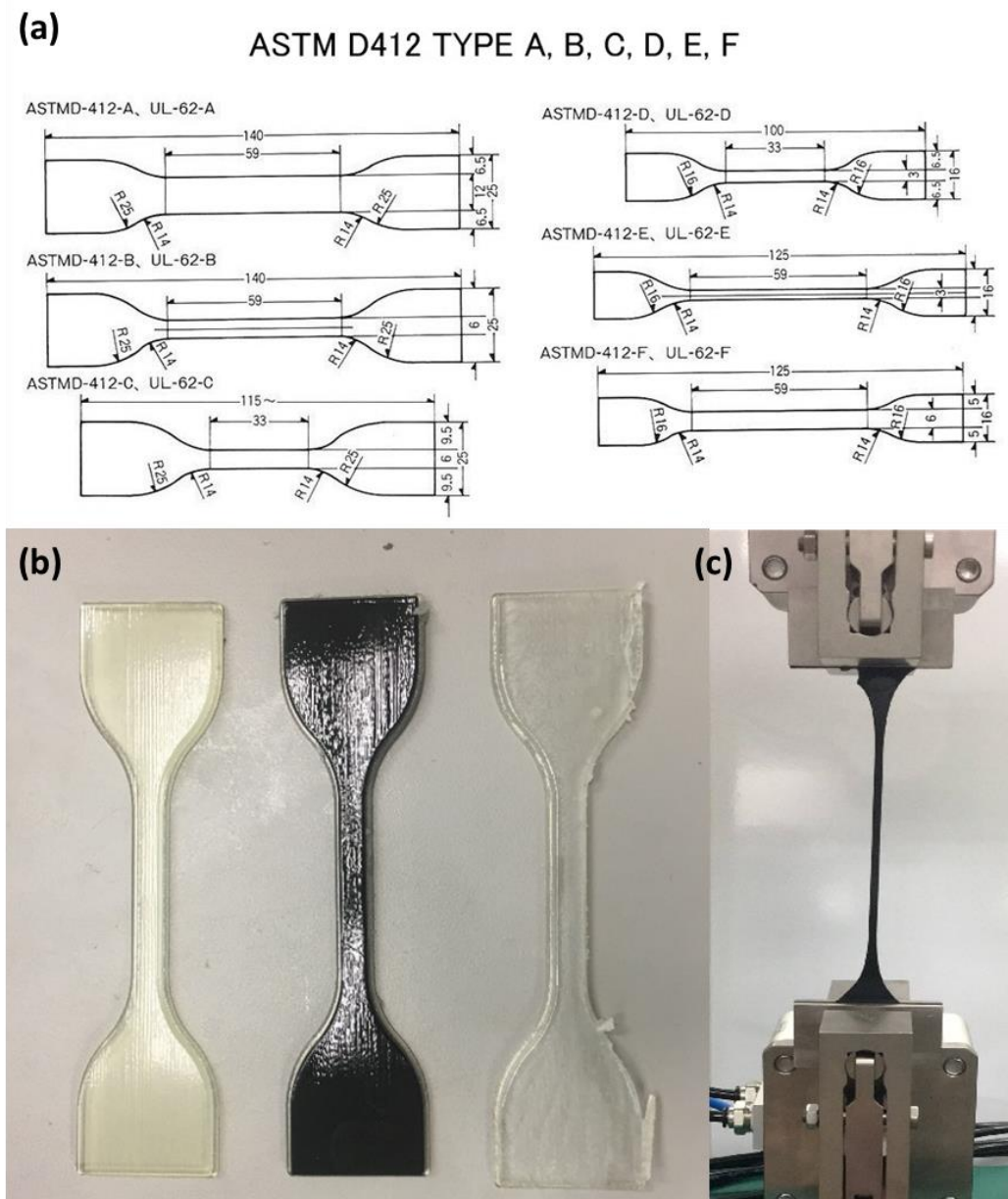
Fig 4.11   ASTM D412 standard for testing vulcanized rubber and thermoplastic elastomers. **(a)** Six types of dumbbell shape specimen in ASTM D412 standard are shown with their corresponding dimensions. **(b)** 3D-printed dumbbell-shaped specimens of AgilusClear30™ (left), TangoBlackPlus™ (middle), and MED610™ (right). **(c)** Uniaxial tensile test for TangoBlackPlus™ with 150% elongation before breakage.

Standard testing procedure for rubber-like elastomer is American Society for Testing and Materials (ASTM) D412. In ASTM D412 standard, there are types of six dumbbell shapes (**Fig 4.11a**) for vulcanized rubber and thermoplastic elastomer testing [138]. In this study, a Type C dumbbell is employed for the uniaxial tensile test. Type C dumbbell-shaped specimens were printed to perform tensile tests. Available primary printing material from the Connex 3 are VeroClear[TM], TangoBlackPlus[TM], and AgilusClear30[TM] (**Fig 4.11b**). Tensile tests are performed with three primary printing materials (**Fig 4.11c**) and compared with Ecoflex[®]. Tensile test results of three elastomeric materials are plotted (**Fig 4.12**). The results show the elongation at break is the highest for Ecoflex[®] 0050 with 420%, continued by AgilusClear30[TM] and TangoBlackPlus[TM] with 310% and 240% respectively. Despite shorter elongation at break compared to Ecoflex[®] 0050, AgilusClear30[TM] exhibits a higher ultimate tensile stress (> 1.5 MPa) and also better in tearing strength, whereas TangoBlackPlus[TM] shows the lowest ultimate tensile stress (< 0.7 MPa) and elongation at break ($< 300\%$) among three hyperelastic materials.
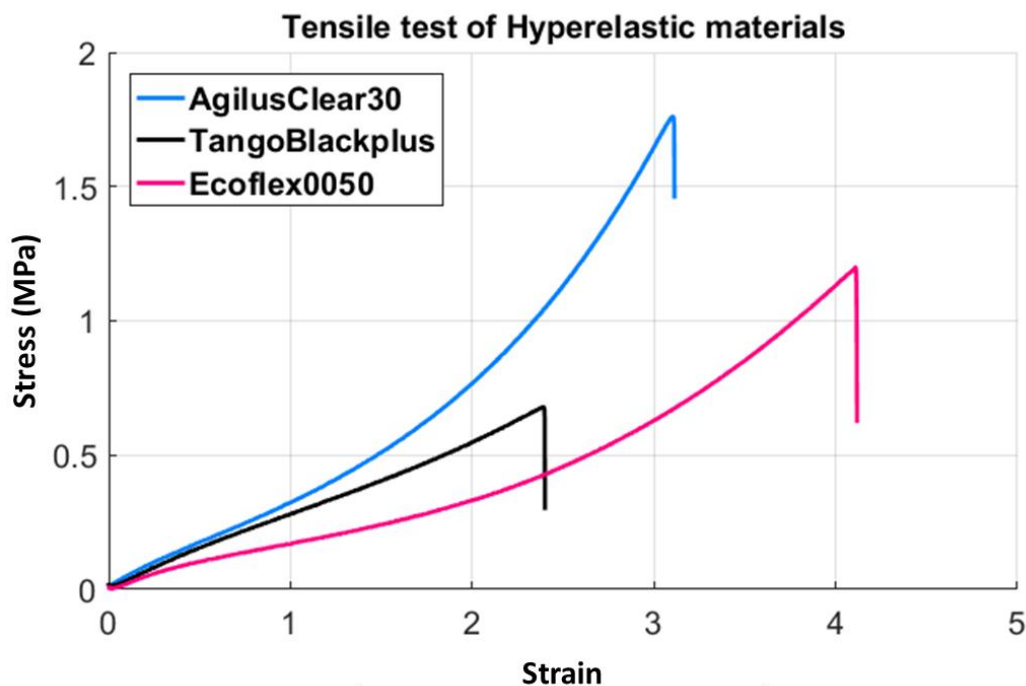
Fig 4.12   Tensile test results of three hyperelastic materials, namely AgilusClear30[TM], TangoBlackPlus[TM], and Ecoflex[®] 0050. Highest ultimate tensile stress is evaluated for AgilusClear30[TM] (1.75 MPa) with high elongation at break ($> 300\%$).

In addition to the primary printing material, Connex 3 also offers an additional technology by combining photopolymers in specific concentrations called digital materials (DM). For instance, the printing selections available are more than three choices, but also with the intermediates between two primary materials.
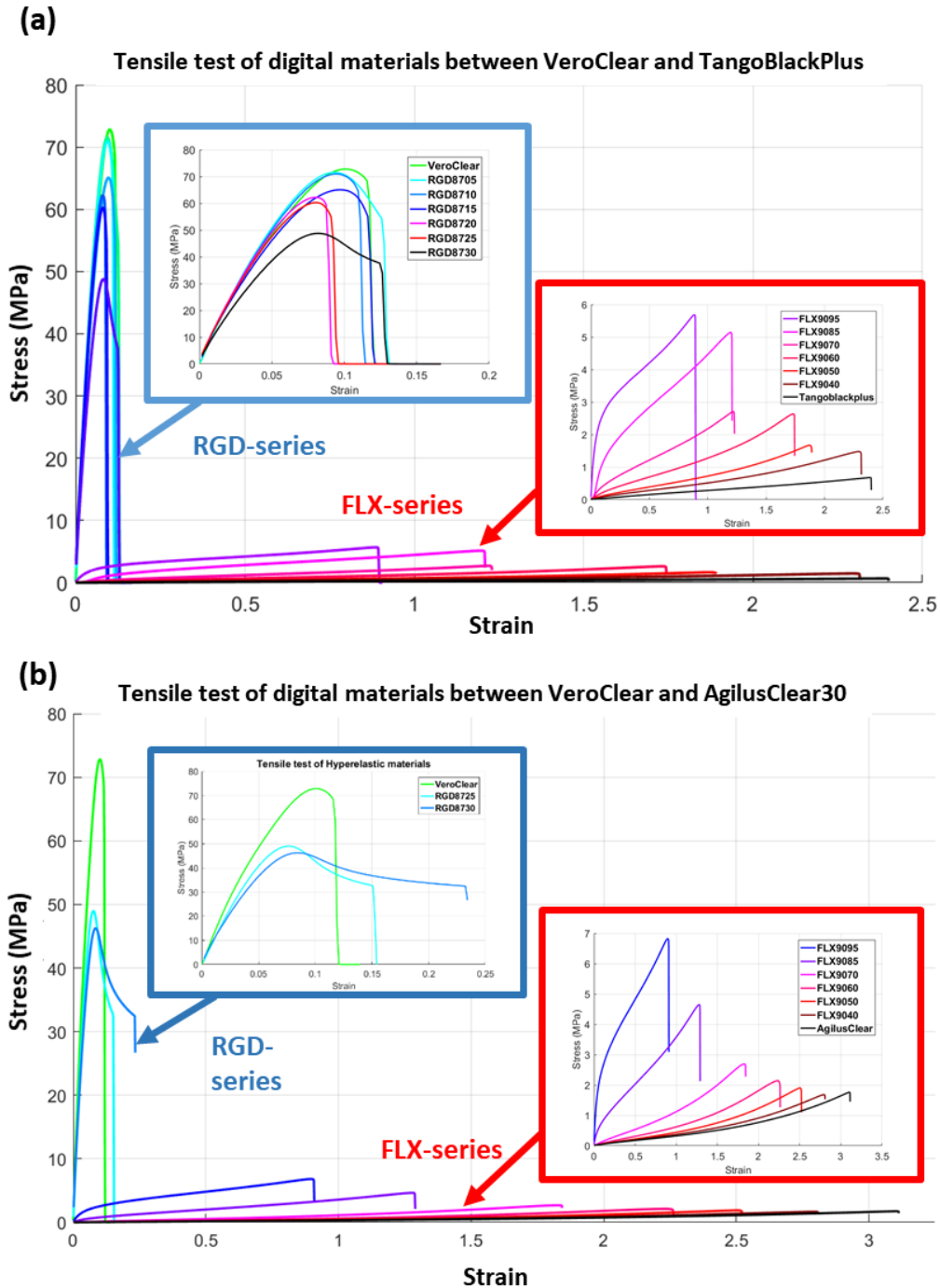
Fig 4.13 Material characterization of digital materials (DM) made by combining two photopolymers in specific concentrations. **(a)** Tensile tests on DM between TangoBlackPlus[TM] and VeroClear[TM]. **(b)** Tensile tests on DM between AgilusClear30[TM] and VeroClear[TM]. High discrepancy is indicated between RGD-series and FLX-series. Blending of two primary materials shows a trade-off relationship between ultimate tensile stress (UTS) and elongation at break. Minimum UTS and elongation at break of AgilusClear30[TM] are higher than TangoBlackPlus[TM].

The digital intermediate has two series, a rigid series closer to VeroClear™ (RGD-series) and a flexible series closer to the elastomers (FLX-series). The high discrepancy is indicated between RGD-series and FLX-series. Tensile tests have been performed for various digital intermediates, which are blended by (i) VeroClear™ and TangoBlackPlus™, and (ii) VeroClear™ and AgilusClear30™. Tensile test results for the DM intermediates are plotted for both blending intermediates by TangoBlackPlus™ and AgilusClear30™ in **Fig 4.13**. By printing individual DM specimens in Type C dumbbell shaped (**Fig 4.14b-c**), uniaxial tensile tests are performed by a uniaxial testing machine (CMT6000, SANS, MTS Systems). The experimental data are compared to the datasheet from Stratasys in **Table 4.3** and **Table 4.4**. It is found that the experimental ultimate tensile stress (UTS) is less than the given UTS provided by the datasheet. However, the experimental elongation at break is higher than the datasheet. It is observed that the 3D printed elastomers in the current laboratory setting are more elastic and less stiff.

Table 4.3 Comparison between tensile test results and Stratasys datasheet for the blending of VeroClear™ and TangoBlackPlus™ in FLX-series

	Ultimate Tensile Strength (MPa)			Elongation at break (%)		
	Datasheet	**Experimental**	**Percentage Difference**	**Datasheet**	**Experimental**	**Percentage Difference**
***FLX980**	0.8 - 1.5	0.6790	−54.73%	170 - 220	240.04	+9.11%
FLX9040	1.3 - 1.8	1.4792	−17.82%	110 - 130	231.49	+78.07%
FLX9050	1.9 - 3.0	1.6708	−44.31%	95 - 110	189.07	+71.88%
FLX9060	2.5 - 4.0	2.6366	−34.09%	75 - 85	174.41	+105.19%
FLX9070	3.5 - 5.0	2.7085	−45.83%	65 - 80	122.91	+53.64%
FLX9085	5.0 - 7.0	5.1444	−26.51%	55 - 65	120.89	+85.98%
FLX9095	8.5 - 10.0	5.6838	−43.12%	35 - 45	90.53	+101.18%

* FLX980 is the technical name of TangoBlackPlus™

Table 4.4 Comparison between tensile test results and Stratasys datasheet for the blending of VeroClear™ and AgilusClear30™ in FLX-series

	Ultimate Tensile Strength (MPa)			Elongation at break (%)		
	Datasheet	Experimental	Percentage Difference	Datasheet	Experimental	Percentage Difference
*FLX2040	2.4 - 3.1	1.76	−43.23 %	220 - 270	310.28	+14.92 %
FLX9740	3.0 - 4.0	1.68	−58.00%	190 - 210	279.14	+32.92%
FLX9750	3.0 - 4.0	1.91	−52.25%	170 - 210	250	+19.05%
FLX9760	3.5 - 4.5	2.14	−52.44%	150 - 170	222.9	+31.12%
FLX9770	4.0 - 6.0	2.69	−55.17%	120 - 140	182.68	+30.49%
FLX9785	6.0 - 10.0	4.65	−53.50%	70 - 90	127.61	+41.79%
FLX9795	10.0 - 14.0	6.82	−51.29%	50 - 70	89.56	+27.94%

* FLX2040 is the technical name of AgilusClear30™

The experimental results showed deviations from the standard datasheet provided by Stratasys. In this research, we chose to use the material properties based on the experimental results to perform FEA. In **Fig 4.14a**, it shows a trend that DM specimens with more VeroClear™ composition caused an increase in UTS and a decrease in elongation at break. The blending of two primary photopolymers shows a trade-off relationship between UTS and elongation at break. Instead of providing standard intermediates with evenly distributed material characteristics, Stratasys provided DM intermediates with a high discrepancy in material property. This separates the DM intermediates by two series, which are: **(i)** RGD-series and **(ii)** FLX-series. In our study, AgilusClear30™ and its DM are chosen with its high UTS and elongation at break compared to TangoBlackPlus™.
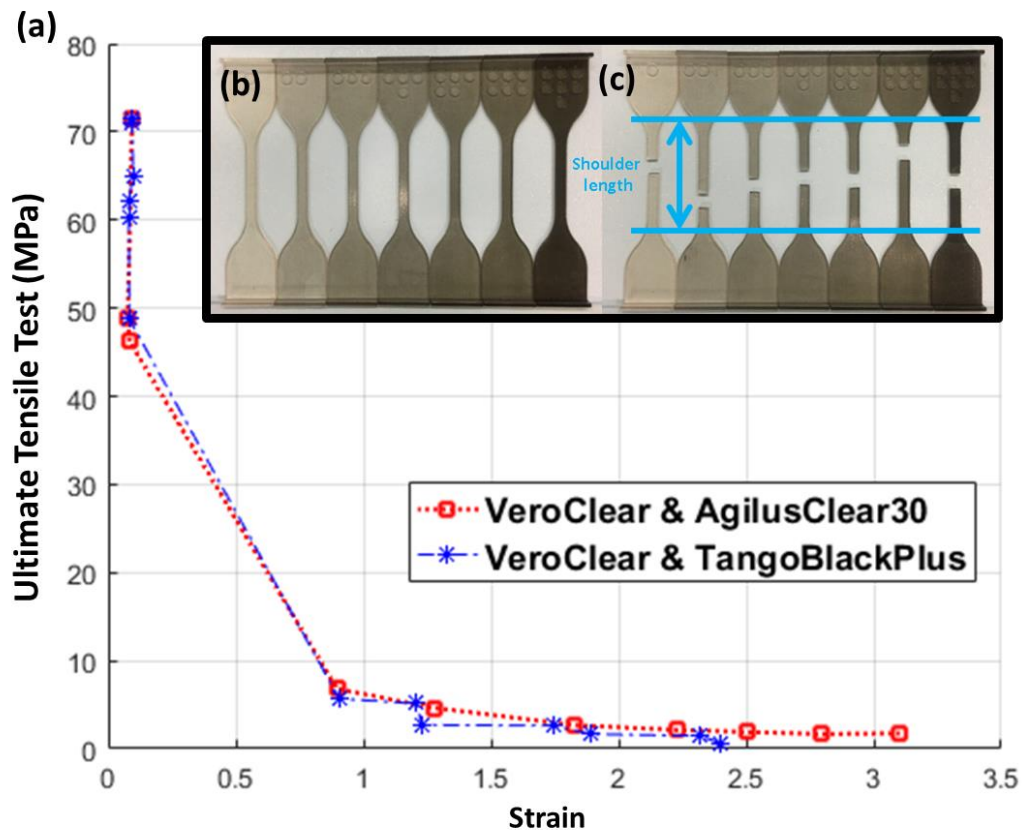
Fig 4.14 **(a)** Trade-off relationship between UTS and elongation at break by two blending combinations. AgilusClear30^{TM} shows higher UTS and elongation at break. **(b)** Tensile test specimens printed in ASTM D412 Type C standard. Digital material printing mode blends photopolymers between VeroClear^{TM} and TangoBlackPlus^{TM} as RGD series. Darker models represent a larger proportion of TangoBlackPlus^{TM}. **(c)** Specimen after tensile tests showing breakage points within shoulder length.

4.5 FINITE ELEMENT MODELING OF REINFORCED SKIN CONSTRAINT

FEA is used as a simulation tool to formulate robotic dynamics according to the strain-stress relationship of the selected elastomer. Finite element (FE) model of the scope structure is tessellated with linear hexahedral (e.g., Abaqus C3D8H). The hyperelastic material is isotropic in nature, which means the unconstrained hyperelastic material will inflate in all directions upon pressurization. To achieve a steering or extension actuation coupling to the hemisphere robotic system, it is necessary to minimize radical expansion and maximize axial elongation. Strain wrapping, or stiffening effect, is considered such that an anisotropic behavior can be modeled. Linear truss element (e.g., Abaqus T3D2) is used to model the

76

strain wrapping constraints that ensure the anisotropic expansion of the elastomeric chambers. The material characteristic is verified by eight hyperelastic models, namely the Arruda-Boyce model, Neo-Hooke model, Yeoh model, Marlow model, Mooney-Rivlin model, 2nd order Polynomial, Ogden model and Van Der Waals model in **Fig 4.15**. The result shows only Arruda-Boyce, Yeoh, and Ogden model predicted a stable model with the similar uniaxial tensile curve. In this research, the Ogden model is used to formulate the 3D-printed hyperelastic material. The strain energy U as a function of principal stretches ε_i for incompressible materials is represented by:

$$U = \sum_{i=1}^{N} \frac{2\mu_i}{\alpha_i^2} \left(\varepsilon_1^{\alpha_i} + \varepsilon_2^{\alpha_i} + \varepsilon_3^{\alpha_i} \right) \tag{4.2}$$

where μ_i and α_i are empirical parameters. Parameters of Ogden model ($N = 3$) are evaluated by Abaqus: $\alpha_1 = 1.4739$, $\alpha_2 = 4.1399$, $\alpha_3 = -0.8090$, $\mu_1 = 4.0196 \times 10^{-2}$, $\mu_2 = 3.4883 \times 10^{-2}$, $\mu_3 = 0.1633$, and $D_1 = D_2 = D_3 = 0$. The units for μ_n and D_n are MPa and MPa^{-1} and α_n are dimensionless.

Six reinforcement constraints are applied to the chamber to maximize the axial chamber extension. The overall design is modeled in the FEA software (i.e., Abaqus) shown in **Fig 4.16**. The applied constraint hinders the radical expansion, hence increasing the effective bending angle of the soft actuating chamber. The simulated model (**Fig 4.16**) illustrates high stress distributed in the positions of skin constraints. The FE model with skin constraint has a maximum strain of 140%, which is within the elongation at break for TangoBlackPlus^{TM}, Ecoflex$^®$ 0050 and AgilusClear30^{TM}. However, the elongation at break is 264% without skin constraints, which exceeds the elongation at break for TangoBlackPlus^{TM} (240%).
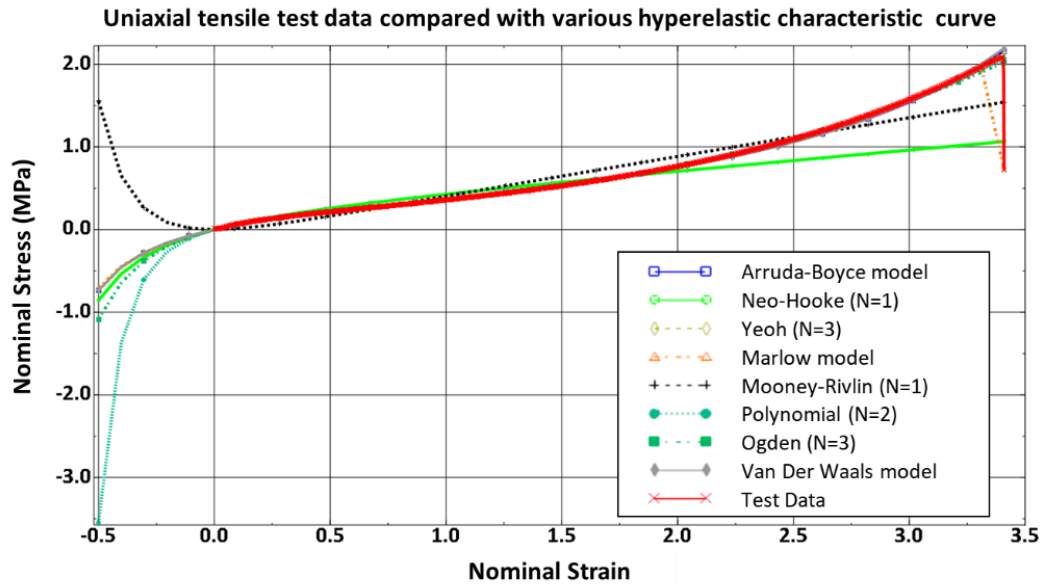
Fig 4.15 Material characterization of AgilusClear30^{TM} evaluated by uniaxial tensile test data (red). Fitting curves of hyperelastic models (Arruda-Boyce, Neo-Hooke, Yeoh, Marlow, Mooney-Rivlin, 2nd order Polynomial, Ogden, and Van Der Waals) are plotted. Only Arruda-Boyce, Neo-Hooke, Yeoh and Ogden shows a stable hyperelastic material model in all strains, but Neo-Hooke modeling shows deviation from the actual tensile test data.
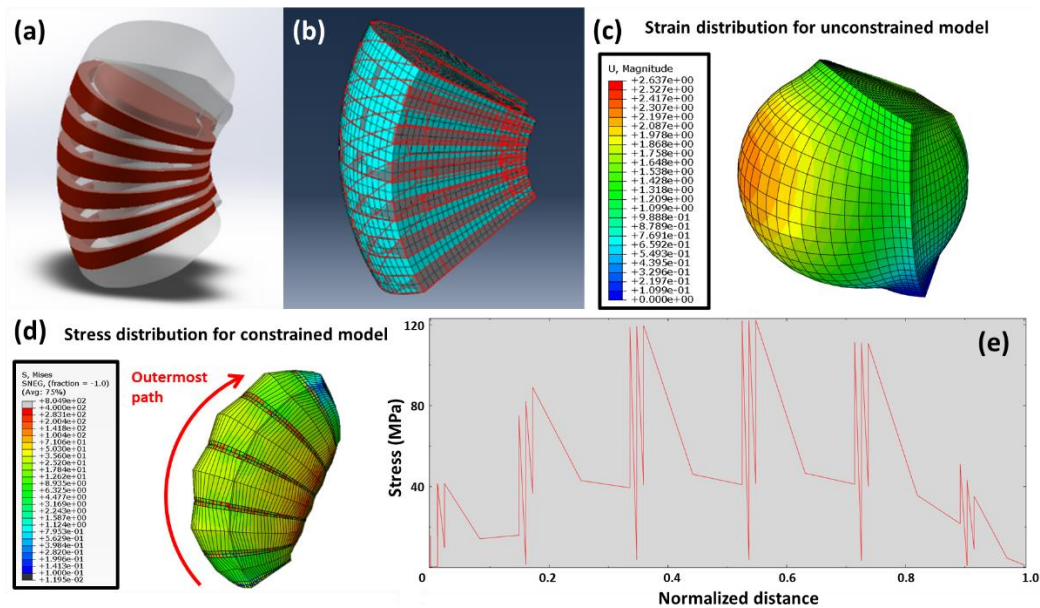
Fig 4.16 **(a)** Soft actuating chamber with skin constraints (red) modeled in SolidWorks. **(b)** Skin constraints applied to the mesh of FE chamber model. **(c)** Unconstrained FE model showing ineffective bending and large strain (263.7%). **(d)** FE model with skin constraint showing stress distribution along the chamber surface. **(e)** Stress distribution along the outermost path on chamber surface. High stresses are indicated in the position of skin constraints.

Moreover, skin constraints with various skin thickness are applied to the elastomeric chamber model. FEA results of the effective bending angle θ_τ against pressure applied u_k to the chamber model are plotted (**Fig 4.17**). Without the

confinement by the constraint, the chamber expands isotropically. The FE model without constraint became unstable when reaching a bending angle of 8º in 0.14 MPa. In contrast, application of the skin constraint stabilized the FE model and effectively increases the maximum bending angle. The bending efficiency ξ is given by:

$$\xi = \frac{\theta_\tau}{u_k} \tag{4.3}$$

The simulation results show the bending efficiency is enhanced by the increasing skin constraint thickness. However, the experienced von Mises stress will also be increased with increasing skin constraint thickness. Therefore, the skin constraint thickness needed to be optimized.
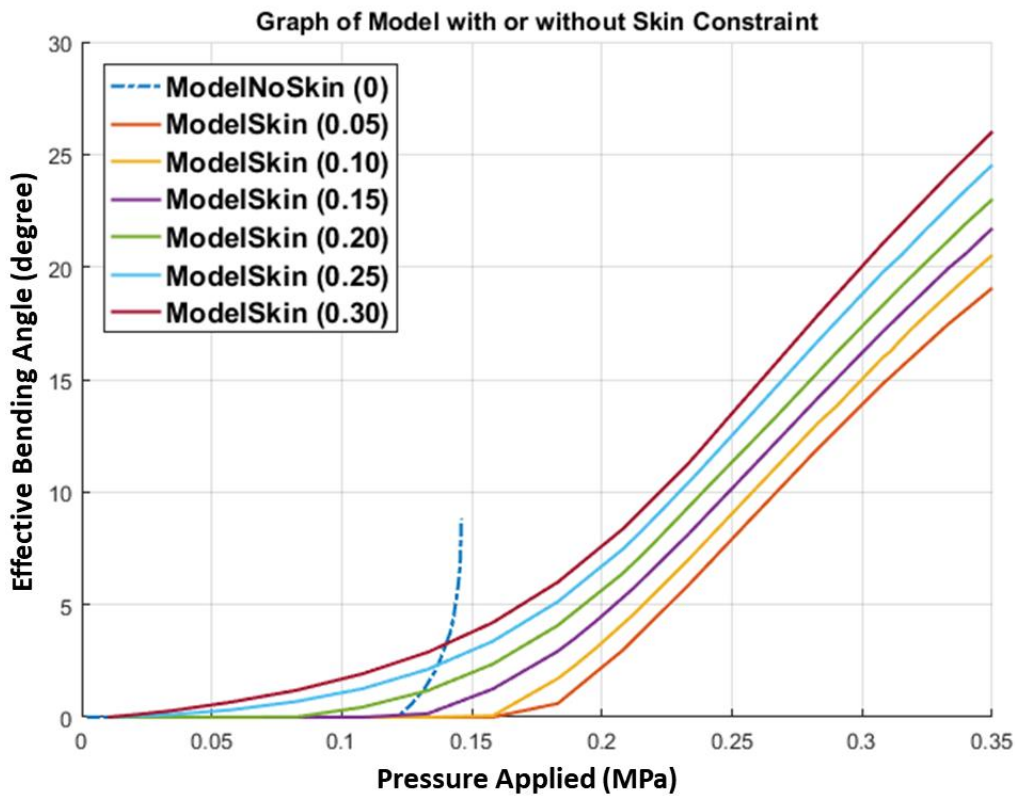
Fig 4.17   FE simulations of skin constraint with various thicknesses (0 - 0.3 mm) on chamber surface. FE model without skin constraint ruptured in 0.145 MPa with a maximum bending angle of less than 10°. Effective bending angles increase with skin constraint thickness.

4.5.1 Evaluation of Skin Constraint

The fRSR prototype is fabricated by the rapid prototyping machine. It is found that TangoBlackPlus^{TM} with the least elongation at break and UTS is ruptured (**Fig 4.17**) upon low pressure (< 0.03 MPa) applied. Therefore, the latest released rubber-like AgilusClear30^{TM} is preferred. It is due to its higher UTS and elongation at break. This material advancement enhances the tear strength and overall elasticity of the soft actuating chamber. Apart from the material limitation of the TangoBlackPlus^{TM}, the FEA simulated prototype in **Fig 4.16** also provides guidance on further robotic miniaturization. As the printed constraint layer has a thickness of less than 0.3 mm, the constraint layer is easy to break and nullify the constraint effect. Another problem is the interlock mechanisms of the skin constraint layer causing the non-uniform thickness of the elastomeric chamber.

4.5.2 Limitation of 3D Printing

The prototype was fabricated by rapid prototyping machine (Stratasys, Connex 3 Objet 350) with a resolution of 600 dpi in the *x*-directions and *y*-directions, and 1600 dpi in the *z*-direction. In another word, the minimum layer thickness in the *z*-direction is 30 μm. Objet 350 has claimed to have a planar accuracy of 200 μm (0.2 mm). However, it is found that there is a limitation to the UV-cured 3D printing methodology, which is a minimum wall thickness required for securing a firm base for the next printing layer. To evaluate the printing capability regarding the minimum wall thickness, various circular shell with a thickness of 0.3 mm to 1.0 mm with a same outer diameter as 2 mm. The calibration model examined with two levels of height (10 mm and 20 mm) as shown in **Fig 4.18**. According to the resulting printing completeness in **Fig 4.18c**, minimum printing thickness for the thin wall is recommended to be printed with more than 0.6 mm.
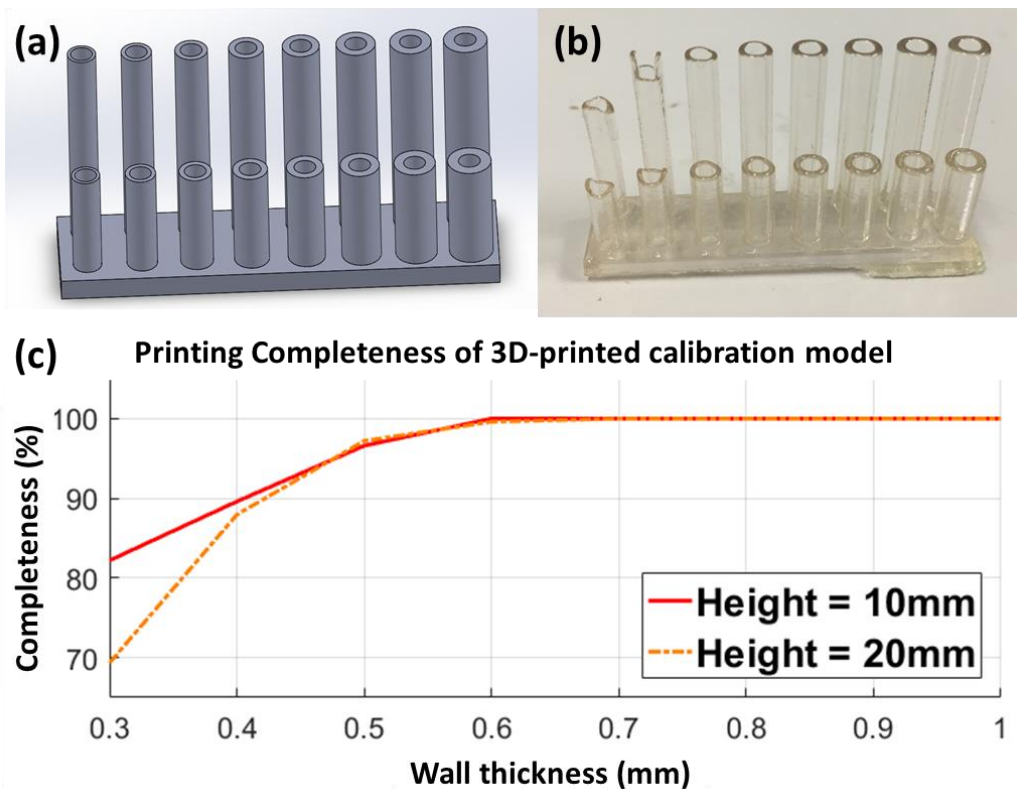
Fig 4.18   3D printed materials test of hollow cylinder wall with various wall thickness (0.3 - 1.0 mm). **(a)** CAD/CAM calibration model showing hollow cylinders with increasing thickness from left to right. **(b)** Actual 3D-printed calibration model showing defects under high height-to-thickness ratio. **(c)** Printing completeness of various wall thickness and printing height (10 - 20 mm). Printing defects are found particularly in thin walls with high heights. This phenomenon is accounted by the instability of uncured resin in high printing layer, causing the loss of resin instead of UV-curing.

4.6   CONCLUSION

In this Chapter, a soft robotic endoscope is designed for navigating the laser fiber to dissect the cancer tumor. This soft robotic actuator composed of hyperelastic material that can morphologically deform to steer the laser collimator to a designated target. The first soft robotic prototype is fabricated by room-temperature-vulcanizing (RTV) silicone rubber molding with an overall dimension of (Ø13 mm × 93 mm). The effect of strain wrapping in the soft robotic system is simulated through FEA. Also, maneuverability is proved by a path following task in an intracavitary space. Feasibility of the soft robotic manipulator with strain wrapping reinforcement is proved with an RMS error of 6 mm. The endoscopic prototype is further miniaturized by 3D-printing technology in **Section 5.2**.

CHAPTER 5
SYSTEM INTEGRATION AND
TELE-OPERATED ACTUATION

5.1 INTRODUCTION

S OFT robotic manipulation system for laser surgery composed of three components, which are: **(i)** fRSR actuator, **(ii)** cRSR actuator, and **(iii)** insertion actuator. Firstly, the fRSR actuator is a fine pan-and-tilt end-effector for laser dissection procedure by steering the laser collimator. Secondly, the cRSR actuator is a coarse bending manipulator for macrobending and targets the fRSR to a specific area for laser dissection. Both RSR actuators require a three-chamber actuation with differential pressure input. Thirdly, the advancement mechanism governs the insertion motion of the laser endoscope. In this Chapter, the advancement mechanism in magnetic resonance (MR) environment will be discussed. Actuation modalities of pressure and volumetric control will be compared. Also, workspace evaluation for RSRs will be performed.

5.2 SPECIFICATION OF CRSR AND FRSR

In **Section 4.5.1**, it is found that the integration interlock design of the reinforcement skin constraint results in non-uniform wall thickness. The uneven distribution of the elastomeric chamber thickness causes the model to rupture by uneven stress distribution over the model. As a result, I proposed to have a cylindrical elastomeric chamber with uniform thickness. The inner diameter and outer diameter are 1 mm and 3 mm respectively. Reinforced springs are applied externally on the surface of the individual cylindrical chamber in **Fig 5.1**.
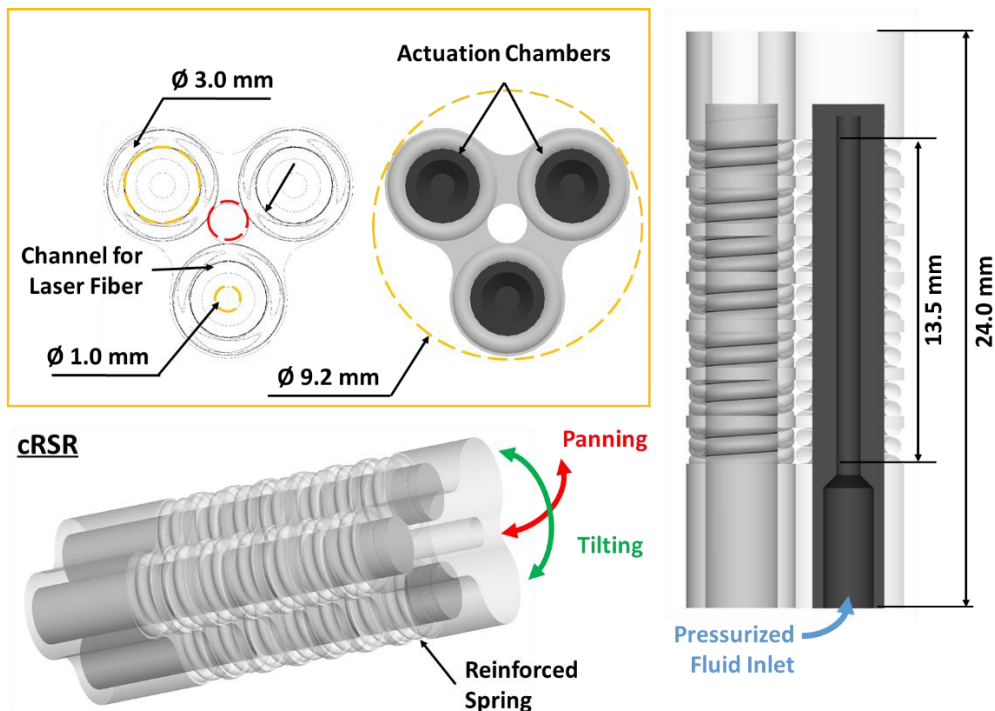
Fig 5.1   Design specifications of cRSR showing critical parameters of chamber. cRSR is strengthened by reinforced spring structure to enhance robustness of actuator. Chamber length and thickness are 13.5 mm and 1 mm respectively. Overall diameter of cRSR reduced to less than 10 mm.

For fRSR, an outer constraint is designed (**Fig 5.2**) to enable robot actuation in confined spaces. For instances, the laser collimator maneuvering is not affected even the fRSR is in contact with the oral, nasopharyngeal (ONP) tissues. In addition, actuation chambers are encapsulated by the outer constraint, which protects from possible leakage of the pressurized fluid. This enhances the robot safety by isolating the actuating system from the external environment. Except hyperelastic chambers are printed by AgilusClear30™, the entire model is printed by MED610™. This hybrid hard, soft robotic device increases the controllability and robustness of the soft medical robot.
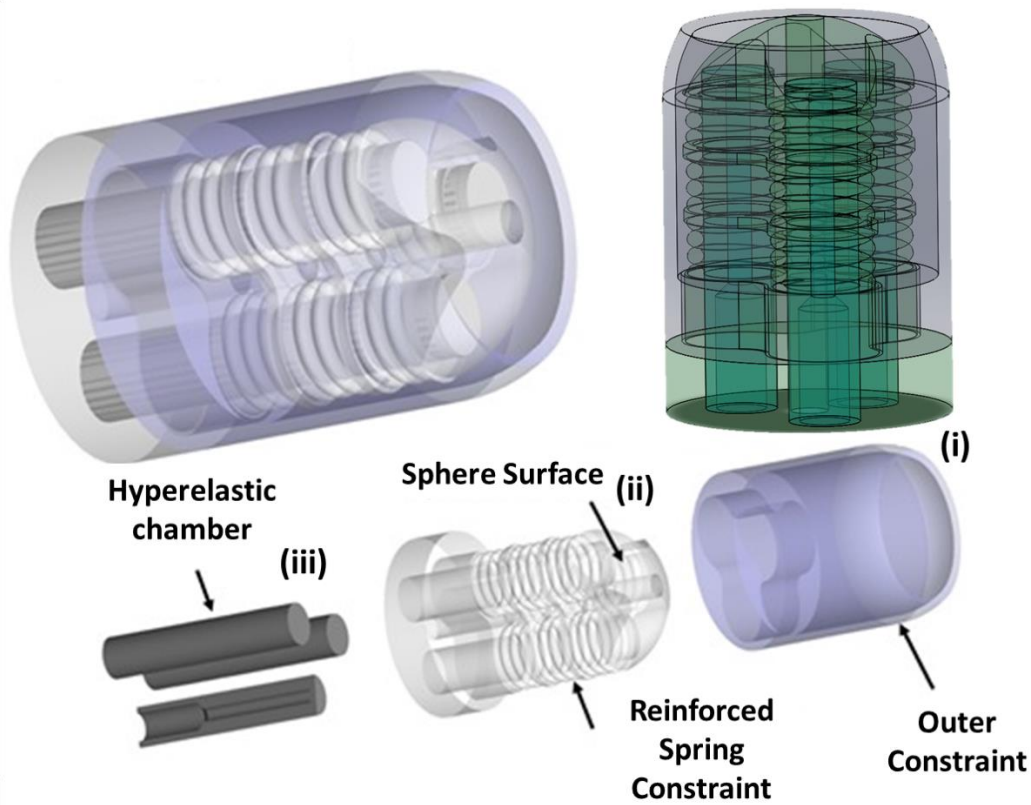
Fig 5.2 Multi-printed fRSR in digital material mode consisted of both rigid and flexible materials. **(i)** Outer constraint and **(ii)** spring reinforced constraint are printed with MED610™. **(iii)** Hyperelastic chambers are printed by flexible AgilusClear30™.

Three cylindrical chambers are reinforced individually by the reinforcement spring, which prohibits the radical expansion. Upon pressurization of the elastomer, the corresponding elastic chamber will elongate individually. The proposed model is designed with partitions to integrate three elongation effects of individual chambers into a coupling bending effect. In **Section 5.2.1**, the effect of the mode of partitions δ on the trend of rigidity and stability will be investigated. Spring reinforced constraint becomes a common feature between cRSR and fRSR. Two actuators are differed by their chamber length l_c in 13.5 mm and 8 mm respectively. In the upcoming simulation, we used 8 mm as the simulation chamber length for comparison. The partition with thickness t_p is separated with a partition distance d_p of:

$$d_p = \frac{l_c + t_p}{\delta} \tag{5.1}$$

84

The rigid constraint is modeled as a plastic material in Abaqus with an elastic modulus of 1000 MPa (MED610^{TM}) calculated by the tensile test mentioned in **Section 4.4.3**. Meanwhile, the elastomer is modeled as a hyperelastic Ogden model evaluated by the uniaxial tensile test data.

5.2.1 Effective Bending Stiffness and Intrinsic Rigidity

In this section, we evaluated the effectiveness of adding partitions by finite element analysis (FEA) (**Fig 5.3**). Finite Element (FE) model of the scope structure is tessellated with quadratic tetrahedron (e.g., Abaqus C3D10H). Two model characteristics outcomes of **(i)** bending angle and **(ii)** maximum von Mises stress are determined to evaluate the effect of partition modes in the reinforced spring model. **Fig 5.3e** shows the effective bending angle decrease with the partition mode, which means the higher pressure is required to overcome the added rigidity to the model. This implies the intrinsic stiffness of the RSR is increased with the addition of partition. Meanwhile, in **Fig 5.3f**, the maximum von Mises stress of the model increases with the partition mode.

For examples, the maximum von Mises stress of mode 0 to mode 5 in 15° bending are 16.20 MPa, 29.59 MPa, 33.76 MPa, 41.70 MPa, 64.97 MPa and 139.49 MPa respectively. Therefore, increasing mode of partition enhances the stiffness of the RSR with the maximum von Mises stress. The von Mises maximum stress experienced by the RSR is nearly doubled when adding partitions. It is worth noting that the mode of partition should not be too large, or the failure will occur in the sharp corner with a high-stress gradient. High model rigidity means the ability to overcome and retain its posture with high bending stiffness.
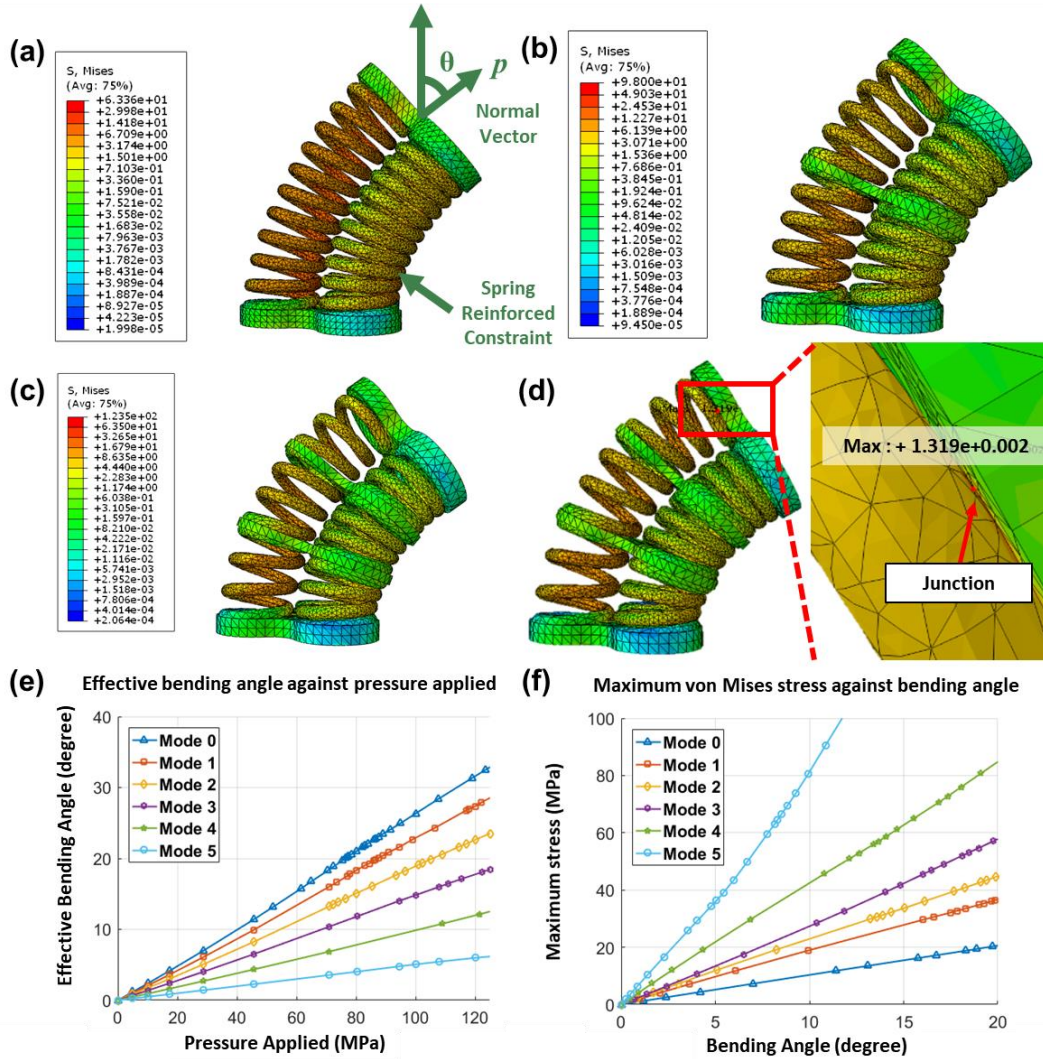
Fig 5.3 Design optimization of cRSR in six partition modes by FEA. Partition modes of **(a)** No partition (mode 0), **(b)** One partition (mode 1) and **(c)** Two partition (mode 2) are illustrated. Notation in cRSR shows normal vector p and bending angle θ. **(d)** Weak point in cRSR in mode 2 showing highest von Mises stress of 131.90 MPa for $\theta = 45°$. **(e)** Bending characteristics against applied pressure stimulated by FEA. Effective bending angle is linearly proportional to the pressure applied and decreases with number of modes. **(f)** Maximum von Mises stress in cRSR model against bending angle stimulated by FEA. Maximum von Mises stress increases with number of modes.

5.2.2 Twisting Effect and Robot Stability

As the RSR comprise of reinforced spring structure, extension with the spring constraint also causes twisting of the overall robotic system. The twisting effect is evaluated by the twisting angle ϕ_t along the bending plane. The results in FEA show the average twisting effect decreases with the partition mode in RSR (**Fig 5.4**). From mode 0 to mode 5, the root-mean-square of the twisting angles are 1.0078°, 0.4821°, 0.4447°, 0.3911°, 0.8998°, and 0.4559° respectively. The design of the partition integrates three individual chambers and causes an increase in stability by

86

sharing the twisting loading to the neighbor chambers. With less twisting effect, it implies that range of robotic fluctuation in nature is minimized. Increase in model stability also implies an increase in model stiffness and reluctance of deformation to the applied forces.
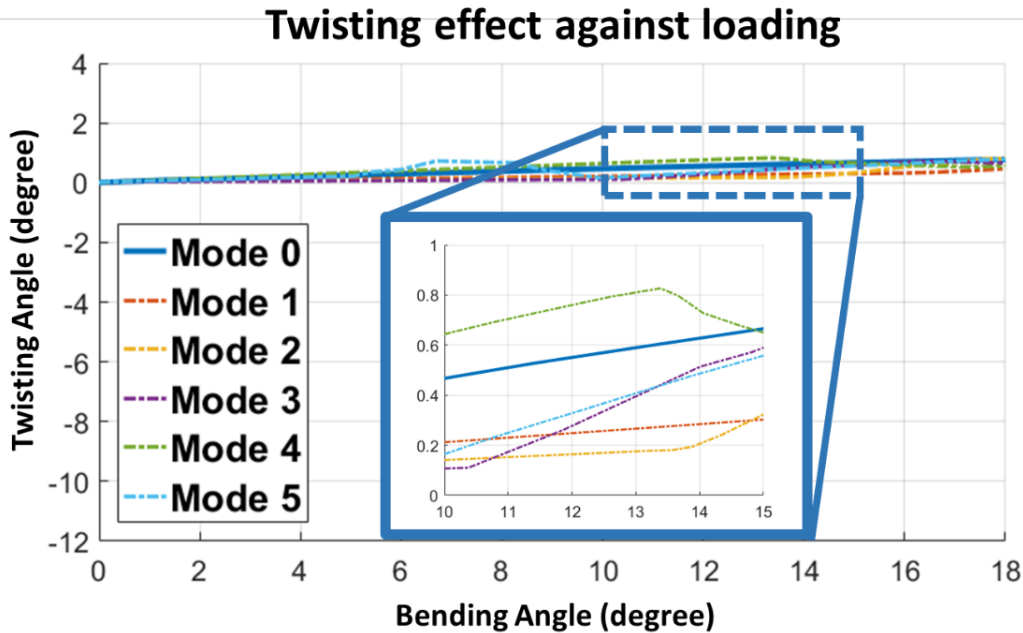
Fig 5.4 Twisting angle ϕ_t of RSR with respect to bending angle θ. Twisting angles are evaluated by deviation angles from the principal bending plane. Six partition modes of RSR are stimulated. Root-mean-square of the twisting angles are 1.0078º, 0.4821º, 0.4447º, 0.5911º, 0.8998º, and 0.4559º. Mode 1 (orange) and mode 2 (yellow) show lower root-mean-square (RMS) twisting angles.

5.3 ADVANCEMENT MECHANISM BY HYDRAULIC ROLLING DIAPHRAGM

Insertion actuator is anchored onto the dental anchorage platform for a static reference. The advancement mechanism is coupled with the long hydraulic transmission system (**Fig 5.5**). This transmission can advance and retreat the robotic endoscope by a combination of pushing and pulling of the rack under magnetic resonance imaging (MRI) system. Advancement mechanism includes rolling-diaphragm sealed hydraulic motor, curved channel, continuum robot segment. The master (in control room) and slave (in MRI room) actuation system consists of two identical pinion-and-rack units to transfer the linear motion to rotary motion (**Fig 5.6a**). The hydraulic power is originated from an electric stepper motor (57BYG250-80, Hongfuda Inc., China) and is transmitted via a pair of semi-rigid long pipes made of nylon. The outer and inner diameters of the tubing are 6 mm

and 4 mm respectively. The length of this pipes pair is 10 meters, which enables tele-operation from the MRI control room. The pipes are filled with incompressible liquid (i.e., water) and are passed through the waveguide in between two rooms.
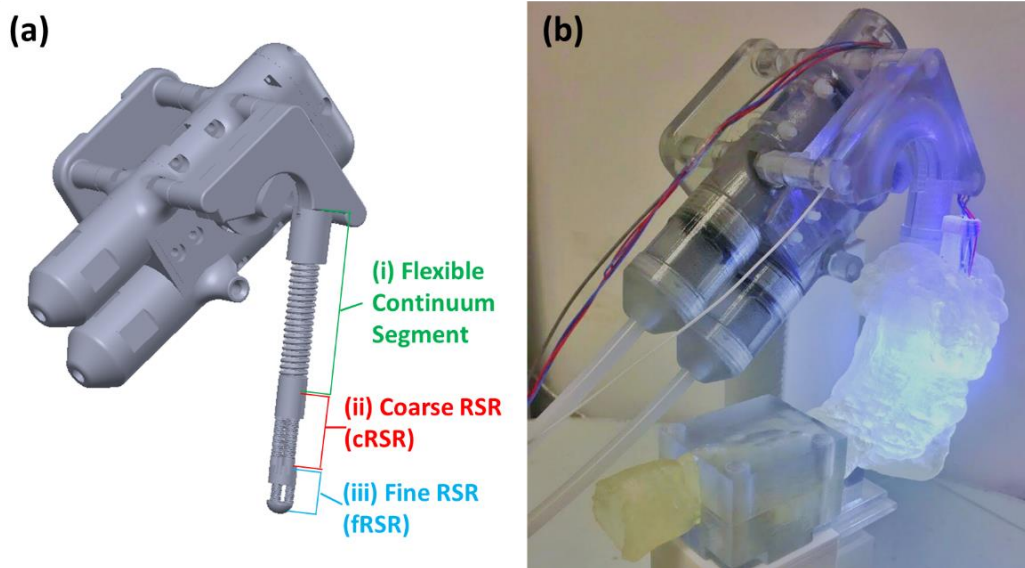
Fig 5.5 **(a)** Schematic diagram of overall robotic system in three segments, which are: **(i)** flexible continuum segment (green) for advancement mechanism. **(ii)** cRSR (red) for coarse steering to the cancerous target. **(iii)** fRSR (blue) for precise aiming of laser collimator. **(b)** Overall robotic system integrated with dental guard anchoring into MR-reconstructed ONP phantom.

Efficiency of the hydraulics transmission heavily relies on the pressure seal. Conventional hydraulic sealing by O-rings has severe sliding friction [139]. Contrarily, rolling diaphragms are efficient in passive fluid transmission with negligible sliding friction [140, 141]. Rolling diaphragms (MCS2018M, FEFA Inc., Germany), which is made of fabric-reinforced molded elastomers, is compatible to be employed in the MR environment [142, 143]. The diaphragm is fixed with the cylinder groove and can act like pressure vessels with flexible sidewalls and a variable volume. Its hat tightly encloses the piston head, frequently flips inside-out and rolls over with the piston to generate linear motion. The length of linear motion depends on the effective stroke of rolling diaphragm.

Compared with the pneumatic actuation approaches [144, 145], the resultant transmission response and power efficiency in hydraulic transmission are much guaranteed. The wall of this rubber diaphragm (**Fig 5.6b**) is fabric reinforced to withstand high fluidic pressure. It has a maximum linear stroke of 20 mm driving the rotary motion of pinion at most by 100.6°. This corresponds to a 39 mm

insertion stroke, which is capable to reach the laryngeal area. The hydraulic pressure was preloaded with about 0.1 MPa to push the piston in close contact with the rolling diaphragm. The preloaded pressure ensures sensitive linear actuation and responsive piston translation, causing the pinion-and-rack gear in steady contact without backlash. It guarantees the insertion stability and accuracy. The resultant rotary motion is converted into a linear insertion motion by a circular guiding track with a bending radius of 20 mm. This structure directs the flexible continuum segment of the overall robotic system to translate in a linear motion. Hysteresis test has been performed for the hydraulic transmission system and hysteresis angle is evaluated as 1.5° by repeatedly rotating clockwise and counter-clockwise by 10 cycles (**Fig 5.6c**).
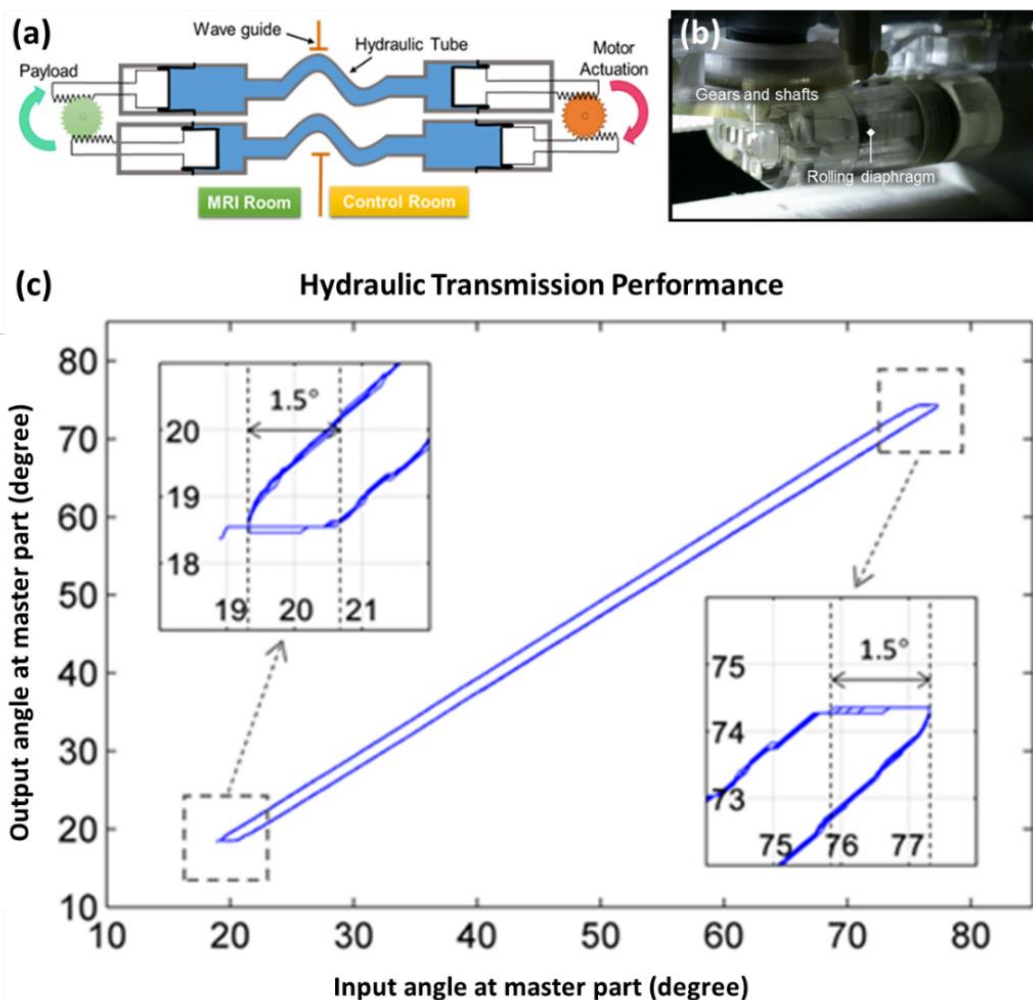
Fig 5.6   **(a)** Design of master-slave hydraulic transmission passing through the waveguide from MRI room to control room. **(b)** Actuation fluid can be tightly sealed by rolling-diaphragms. No sliding friction is involved as using conventional O-ring sealing. **(c)** Hydraulic transmission performance validated based on the angular response and corresponding hysteresis loops. Hysteresis angle is evaluated as 1.5° by repeatedly rotating clockwise and counter-clockwise by 10 cycles.

5.4 ACTUATION SETUP FOR SOFT ROBOTIC ENDOSCOPE

Research has been done for integrating a standalone soft robotic system with miniaturized valve and wireless controller [119]. However, the maximum fluidic pressure only has 70 kPa, which represents low robot stability. In our research, we aimed to use an MR-conditional soft robotic manipulator for tele-operative procedure. In this part, the actuation modalities of RSR system are compared by actuating with pressure and volumetric controls.

5.4.1 Pressure Control by Pressure Regulation Valve

The first approach is to directly control the input pressure for individual chamber. An electro-pneumatic pressure regulator (ITV1050-312L, SMC) (**Fig 5.7a**) is deployed. The range of the pressure control is from +5 kPa to +900 kPa with a step resolution of 5 kPa. The advantage of using a pressure control system is the fast response time for 0.1 s. But this system limits the actuation fluid as a pneumatic input and require a stable pressure source for more than 600 kPa. In addition, the step resolution is limited to 5 kPa which is rough for continuous pressure actuation. Moreover, instead of active retraction of the actuation fluid, this electro-pneumatic pressure regulator only turns on a three-way valve to release the internal system pressure, which causes a delay in actuation.

5.4.2 Volumetric Control with Stepper Motor Control

Other than controlling the pressure input directly, there is another actuation approach to control the volumetric input. In this Section, stainless steel cylinders with a bore diameter of 32 mm are used (CDM2B32-200Z, SMC) and maximum actuation stroke of 200 mm. The fluidic cylinder is mounted onto the linear stepper motor to control the actuated stroke. The volumetric control setup (**Fig 5.7b**) enables to use of hydraulic fluid. However, the relation of the pressure-volume curve for the hydraulic fluid is not linear, a correlation of the stepping position (inputted volume) to the output pressure needed to be rectified. The pressure feedback is obtained by an external pressure sensor (ISA80 Series, SMC) (**Fig 5.7c**)

to map the pressure-volume correlation. A relationship between the stepper positions to the output pressure is plotted (**Fig 5.7d**).
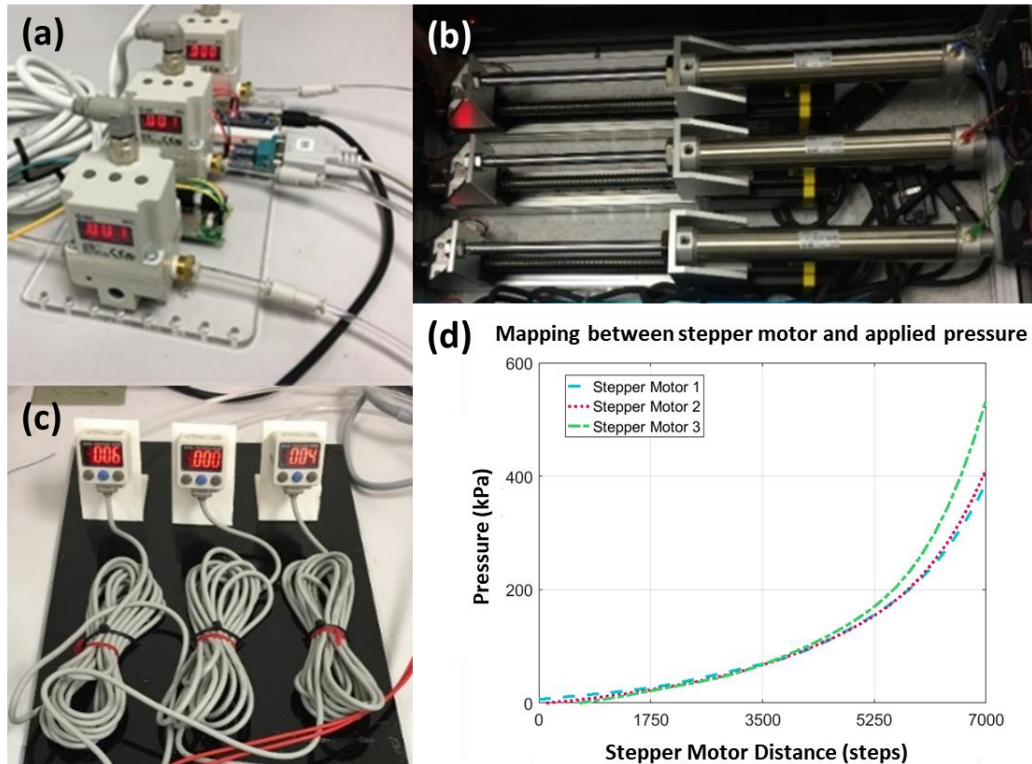
Fig 5.7   Actuation devices for fluidic control. **(a)** electro-pneumatic regulators (ITV1050-312L, SMC) for pressure control. **(b)** Volumetric control mechanism using three pneumatic cylinders (CDM2B32-200Z, SMC) actuated by linear stepper motors. **(c)** Pressure sensors (ISA80 Series, SMC) providing visual and analog feedback for volumetric control system. **(d)** Relationship between stepper motor positions and output pressures of three actuation chambers. Non-uniformity mapping characteristic is related to distinct system volume for individual channel. Total volume of individual chamber depends on the initial cylinder volume, length of transmission tubing and internal chamber volume.

Both pressure and volumetric control actuation setups have their own characteristic. Pressure control system yields a compact setup space, but the pressure is fluctuating in a given set point. Pneumatic actuation system has a slow response time due to the air compressibility and requires a sufficient preloading (around 3000 steps) to yield a linear pressure-volume relationship. However, the preloading for pneumatic actuation causes preloading stress to the entire robotic system. In our research, the laser dissection surgery requires a slow steering speed. Therefore, hydraulic actuation control system is more preferred by its stable pressure output. Using hydraulic actuation fluid reduces the fluidic compressibility and enhances the actuation sensitivity in the low-pressure regime. As the compressibility of water is higher than air, less preloading is required.

5.4.3 Hysteresis of Actuation Fluid

Dynamic performance of soft robot shows a lagging effect during maneuvering. This implies the robot requires time to configure a designated shape or original shape. This lagging effect is called hysteresis. By loading and unloading the input pressure to the actuator, the hysteresis effect is demonstrated by measuring output variables such as strain or bending angle. Hysteresis characteristic curves with two actuation fluids are plotted by comparing the bending angle in **Fig 5.8**.
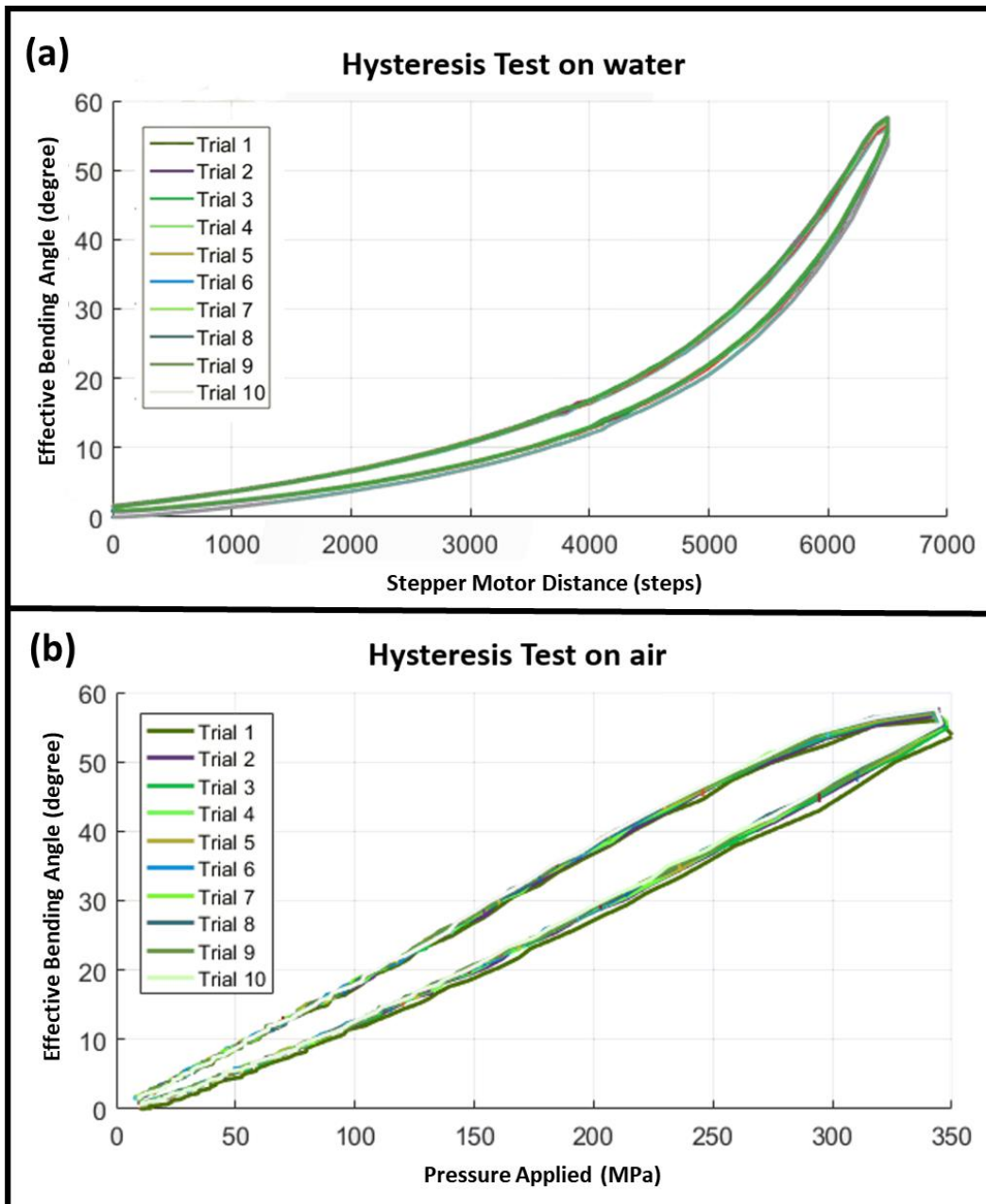
Fig 5.8   Evaluation of hysteresis effect of various actuation fluid. Ten consecutive actuation cycles with 10 seconds/cycle performed by two actuation fluids, namely **(a)** water and **(b)** air. Reduction in hysteresis effect is demonstrated in water with low hysteresis angle of 6°. Hysteresis angle for air is 10° by using the same end-effector with a maximum bending angle of 60°.

Hysteresis is rate-dependent, which is less significant when the pressure varies slowly. Ten consecutive actuation cycles are performed by two actuation fluids, namely water and air. As two systems are recorded by different actuation modalities (i.e., volumetric and pressure control), the test is normalized by using the same end-effector with a maximum bending angle of 60°. The power loss in hysteresis is the inclusive area in-between the loading and unloading curves. Result shows a lower hysteresis effect in water with the smaller inclusive area and maximum hysteresis angles of 6°, compared to maximum hysteresis angles of 10° in air. Power losses in hysteresis are accounted by dissipative effects such as heat or sound.

5.5   KINEMATIC MODELING OF SOFT MEDICAL ROBOT

By selecting water as the hydraulic fluid, the fRSR actuator is controlled to deflect the laser collimator. By applying various pressures to three individual chambers, a panoramic control can be achieved. Experimental setups are built for the validation of RSRs regarding their kinematic and projection workspaces. An electromagnetic (EM) tracking system (Aurora system, Northern Digital Inc.) is deployed to track the position and normal direction of the RSR's tip. In **Section 5.5.1**, both workspaces for the cRSR actuator and fRSR actuator are evaluated. With both position and direction vector, a virtual projection plane can be formulated to evaluate the projection accuracy of the RSRs. A virtual plane is placed in a 15 mm distance away from the laser collimator tip. This mid-range projection distance is less than μRALP (20 mm) [98] to give a conservative estimation of the ONP workspace. Therefore, the experiments concerning accuracy in **Section 6.2**, a projection distance of 15 mm is assumed.

5.5.1 Workspace Evaluation of RSRs

Kinematic workspace of cRSR is first evaluated. The maximum bending angle of cRSR is greater than fRSR due to the design of the outer constraint (**Fig 5.2**). Without the outer cover, cRSR enables to maneuver in an unconstrained bending and offers a maximum bending angle of 120º. By inputting random pressures into cRSR, a hemisphere kinematic workspace is evaluated (**Fig 5.9**).
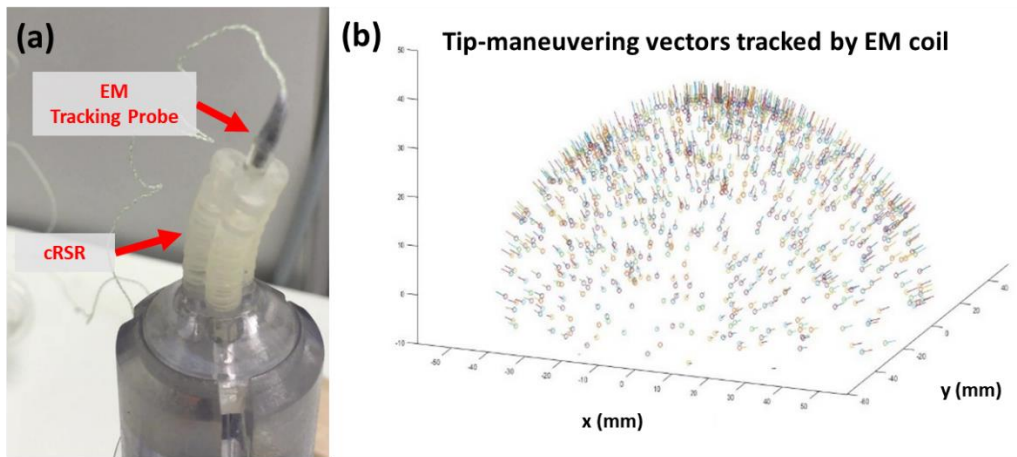
Fig 5.9 Kinematic workspace analysis of cRSR with EM tracking system. **(a)** Experimental setup of hydraulic-actuated cRSR deflecting EM tracking probe. Pitch and roll angles of cRSR are determined by the EM tracking system. **(b)** Side view of tip-maneuvering point cloud showing their corresponding normal direction vector. Scattering point cloud is obtained by applying differential pressures into cRSR.

Projection workspace of the fRSR is also evaluated. Firstly, the principal bending axis is evaluated by actuating three principal chambers individually in 0.154 MPa. Three projection lines are plotted in 120º apart. Secondly, by actuating two adjacent chambers with the same pressure of 0.154 MPa, the projection plane yielded three extra intermediate points and formed a hexagon shape. Finally, by interpolating actuation pressure linearly between 6 points, a hexagon shape in the virtual projection plane is obtained in **Fig 5.10**.
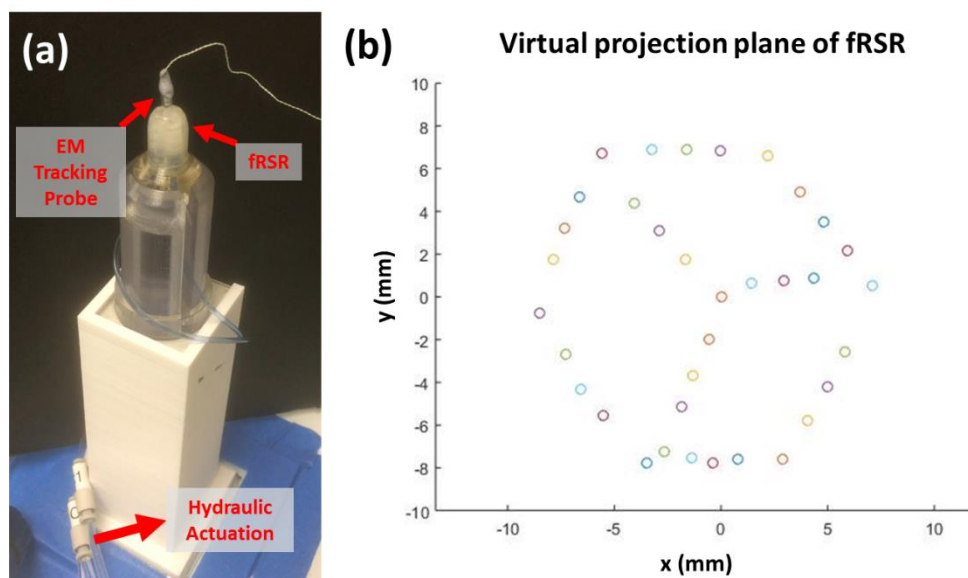
Fig 5.10 Projection workspace evaluation for fRSR with EM tracking system. **(a)** EM tracking probe determining pitch and roll angle of hydraulic-actuated fRSR. Laser projection workspace is calculated by the tracked position and normal vector. **(b)** Projection workspace of fRSR showing hexagon shape in virtual projection plane.

94

This proved the distributed actuation pressure to the projection characteristic is symmetric by the 3D-printed RSR model. However, the combination of applied pressures cannot be accurately predicted by linear interpolation, as there are human errors during fabrication and 3D printing post-processing. Another control modality is required to learn the complex relationship between the actuating input and the robotic kinematics. In **Chapter 6**, we shall discuss the control modality by using a neural network (NN) training.

As the overall constraint limited the maneuvering workspace of fRSR, higher pressure is needed to actuator fRSR compared to cRSR. Thus, fRSR has a greater actuating pressure range and hence gentler pressure gradient, thus offering a higher actuating resolution for the laser targeting performance. Therefore, cRSR is designed as a bending actuator to approximately target the interested region, whereas fRSR is designed as a precise steering actuator to manipulate the laser collimator.

5.5.2 Kinematic Modeling for RSRs

Kinematic model of RSR actuator is represented by the spherical coordinate system (**Fig 5.11**) to simplify the notation in angular representation while providing an identical positional information. In the polar coordinate system, we have a radial parameter ρ, and angular parameters of pitch angle θ and roll angle ϕ:

$$x = \rho \sin\theta \cos\phi \tag{5.2}$$

$$y = \rho \sin\theta \sin\phi \tag{5.3}$$

$$z = \rho \cos\theta \tag{5.4}$$
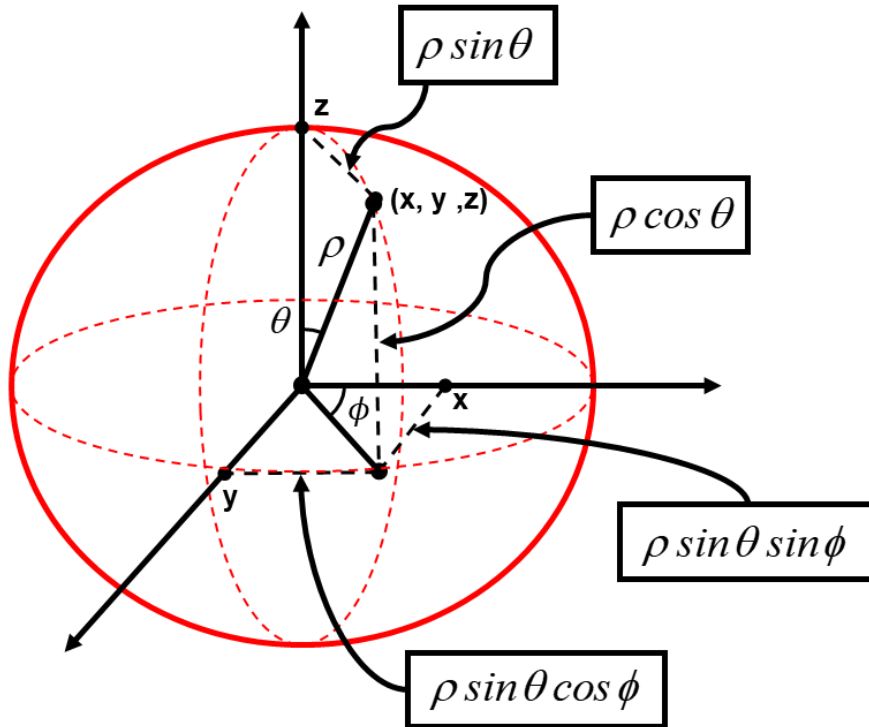
Fig 5.11   Spherical coordinate system represented by radial coordinate ρ and angular coordinate θ and ϕ.

With $0 \le \theta \le \pi$ and $0 \le \phi \le 2\pi$ or equivalent,

$$\rho = \sqrt{x^2 + y^2 + z^2} \tag{5.5}$$

$$\theta = \tan^{-1}\left(\frac{\sqrt{x^2 + y^2}}{z} \right) \tag{5.6}$$

$$\phi = \tan^{-1}\left(\frac{y}{x} \right) \tag{5.7}$$

The RSR with a natural arc length $\hat{l}$ is bent in a pitch angle of θ, is denoted with a bending radius of $1/\kappa$ under constant curvature assumption:

$$\hat{l} \cdot f(\theta) = \frac{\theta}{\kappa} \tag{5.8}$$
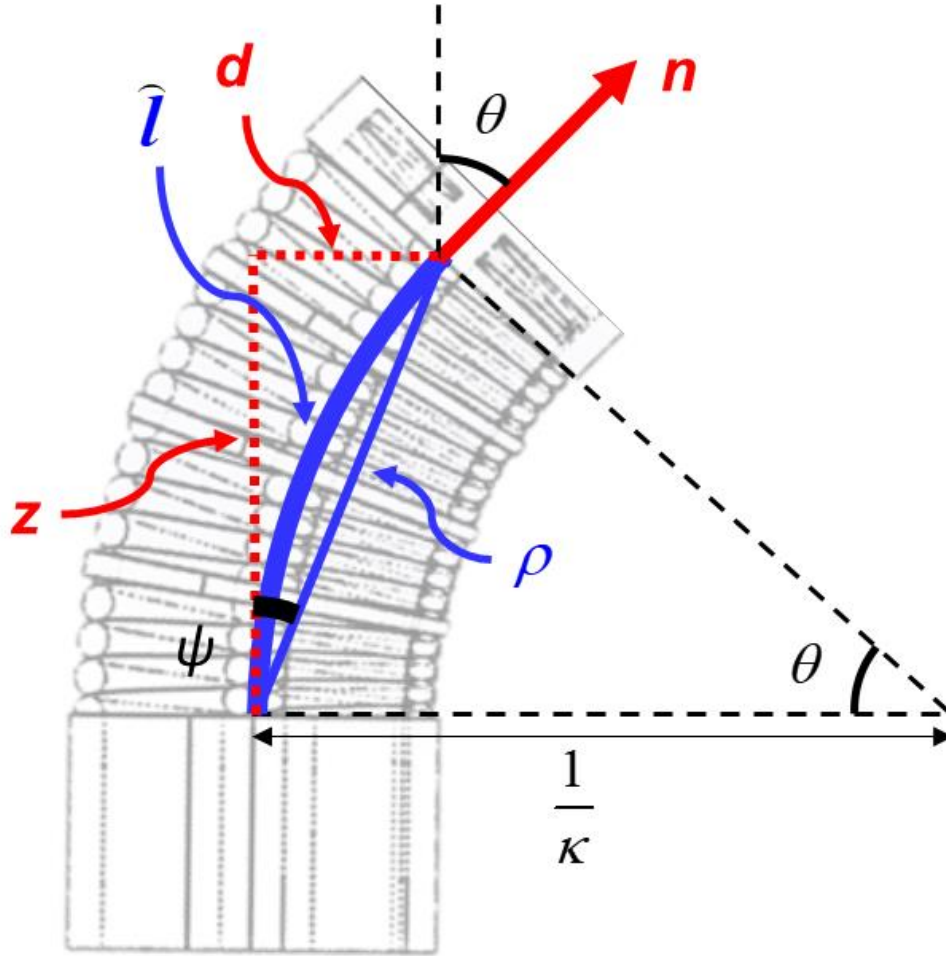
Fig 5.12 Schematic diagram of cRSR showing robot configuration when $\phi = 0$. Bending arc lies on the $x-z$ plane. Arc parameters defined the circular arc using bending curvature κ, chord length ρ, normal vector n, and overall bending pitch θ.

We assumed there is an elongation function with respect to the increasing pitch angle by $f(\theta)$. By the cosine formula, the chord length (or polar distance in spherical coordinate) is represented by ρ:

$$\rho^2 = \left(\frac{1}{\kappa}\right)^2 + \left(\frac{1}{\kappa}\right)^2 - 2\left(\frac{1}{\kappa}\right)^2 \cos\theta$$

$$\rho = \left(\frac{1}{\kappa}\right)\sqrt{2 - 2\cos\theta} \tag{5.9}$$

In **Fig 5.12**, the bending arc of the cRSR is configured in the x-z plane. The roll angle is denoted as ϕ in **Fig 5.11** and the deviation distance is denoted as d, the Cartesian representation of x and y are:

97

$$x = d\cos\phi \tag{5.10}$$

$$y = d\sin\phi \tag{5.11}$$

Substituting **Equation 5.7** and **Equation 5.8** in the following equation gives:

$$d = \rho\sin\psi \tag{5.12}$$

$$d = \frac{\hat{l}\cdot f(\theta)}{\theta}\sqrt{2 - 2\cos\theta}\left(\sin\psi\right) \tag{5.13}$$

By the trigonometry, $\psi = \theta/2$, which gives,

$$d = \frac{\hat{l}\cdot f(\theta)}{\theta}\sqrt{2 - 2\cos\theta}\left(\sin\frac{\theta}{2}\right) \tag{5.14}$$

$$x = \frac{\hat{l}\cdot f(\theta)}{\theta}\sqrt{2 - 2\cos\theta}\left(\sin\frac{\theta}{2}\right)\cos\phi \tag{5.15}$$

$$y = \frac{\hat{l}\cdot f(\theta)}{\theta}\sqrt{2 - 2\cos\theta}\left(\sin\frac{\theta}{2}\right)\sin\phi \tag{5.16}$$

The vertical height z is calculated as:

$$z = \rho\cos\psi \tag{5.17}$$

$$z = \frac{\hat{l}\cdot f(\theta)}{\theta}\sqrt{2 - 2\cos\theta}\left(\cos\frac{\theta}{2}\right) \tag{5.18}$$

The coupling bending effect from three individually reinforced chambers cause elongation and bending at the same time. We cannot assume the workspace is an ideal hemisphere as the elongation effect existed with the length elongation function of $f(\theta)$. By plotting the end-effector position onto a normalized bending plane, the distribution of the scattered sample point is evaluated in **Fig 5.13**. With the scatter point in the normalized bending plane, we assumed the elongation function is directly proportional to the factor of pitch angle θ, where:

$$f(\theta) = k_e \left(\frac{\pi + \theta}{\pi} \right) \qquad \textbf{(5.19)}$$

A regression curve is fitted with a linear factor k_e of 0.45. However, due to human error for the post-processing of 3D printing. This causes non-identical performance for each spring reinforced chamber and requires calibration each chamber. This variation of model property results in difficulty in predicting the model kinematics mathematically. In **Chapter 6**, we will discuss a data-driven control modality by using NN training.
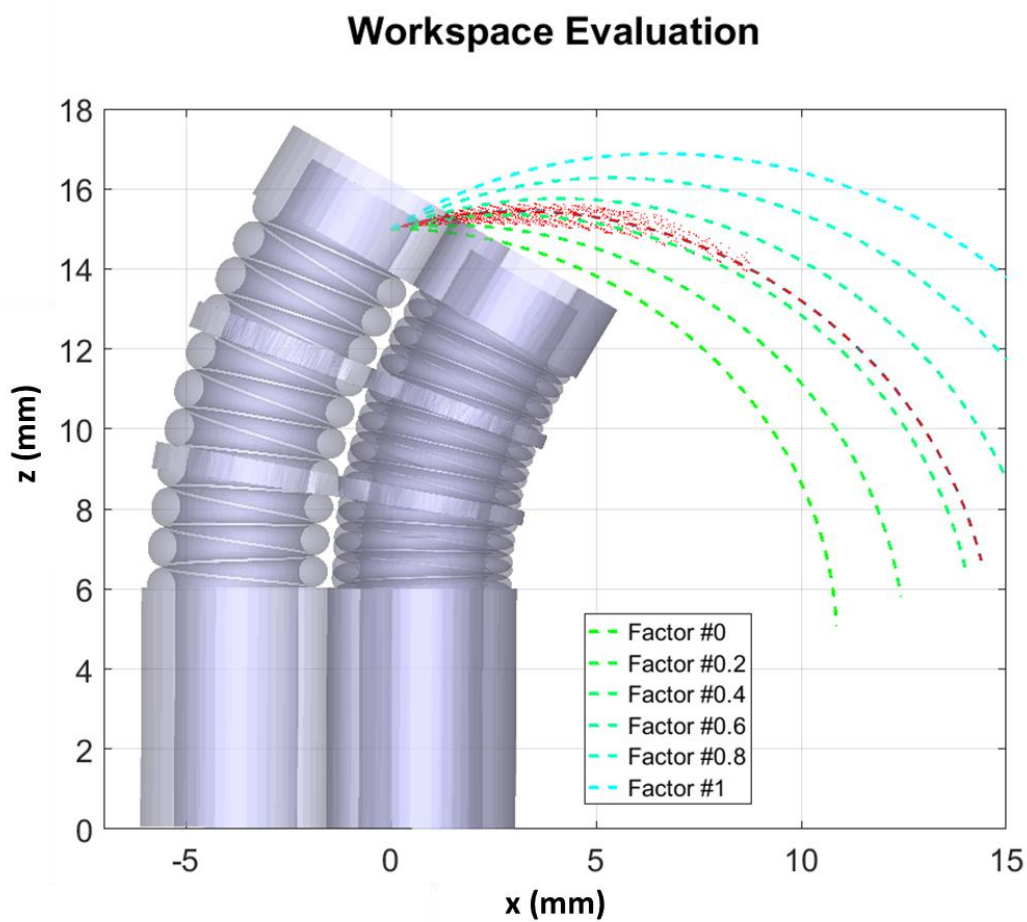
Fig 5.13   Workspace evaluation of cRSR by EM tracking position. Scattered point (red) are normalized along *X-Z* plane. Prediction curves in **Equation 5.18** with various elongation factors k_e are plotted (green). Natural length of cRSR is 15 mm. Best fit regression curve (red) showing a linear elongation factor $k_e = 0.45$.

5.6 CONCLUSION

In this Chapter, the overall soft robotic endoscopic system for MRI laser surgery is integrated with three components, which are: **(i)** fRSR actuator, **(ii)** cRSR actuator, and **(iii)** insertion actuator. Miniaturized RSR actuators (<Ø12 mm) is further optimized by the addition of partition structure. The optimal number of partitions (or modes) is stimulated by FEA and evaluated by the intrinsic rigidity and robot stability. Advancement mechanism is also designed to govern the insertion motion of the laser endoscope. The actuation setup modalities are tested and compared. Hydraulic volumetric control is adopted by the lowest hysteresis effect. Lastly, the kinematic model is formulated and workspace evaluation for the RSR is performed. It is found that the overall arc length of RSR increases with the pitch angle by a linear factor k_e of 0.45. However, the regression curve cannot accurately predict the RSR tip position for robotic control. The control methodology is data-driven and will be discussed in next Chapter.

CHAPTER 6

NEURAL NETWORK TRAINING

AND ROBOT PERFORMANCE

6.1 INTRODUCTION

I N this Chapter, I aimed to demonstrate the proposed control framework of the tele-operated RSR by following pre-defined trajectories. Path following task is admissible to various soft robotic applications. A robust robotic control provides precise targeting of the high-power laser to perform tissue ablation or dissection. In **Section 6.1.2**, the control correlation mapped by a neural network (NN) function in MATLAB is deployed and evaluated. The forward and inverse kinematics are formulated. The modality of data acquisition is discussed to obtain a high correlation between NN training input and output. The performance of both cRSR and fRSR are examined by their accuracy, reliability, and MR-compatibility. Finally, an *ex-vivo* laser dissection task is performed under magnetic resonance imaging (MRI).

6.1.1 Forward Kinematics of RSRs

With the complicated hyperelastic property of AgilusClear30^{TM}, the robotic control of the actual prototype cannot be accurately predicted by the kinematics modeling. Paramount to surgical safety, having a decent control performance in the presence of a confined and dynamic environment is also essential. Therefore, much research effort [146-149] has been paid for deriving analytical models with the aim to describe or predict the robot kinematic/dynamic behavior [150], akin to controlling conventional rigid-link robots. However, these analytical models are complex due to the intrinsic non-linear hyper-elastic property of the soft elastomeric materials, which constitute the robot body. Any additional control dimensionality of the soft robot would further exacerbate the complexity of such kinematic equations [147]. In this research, the control modality for RSR is data-driven. In **Fig 5.9**, a hemispheric point cloud shows the kinematic workspace with the corresponding normal vectors. Each point on the point cloud denotes the static configuration of the robot is measured by the 6D EM-based positional tracking device (NDI Medical Aurora). In time step k, the combination of chambers' pressures u_k is:

$$u_k = \left[u_1, u_2, u_3, ..., u_{N_c} \right]; \ u_k \in \mathbb{R}^{N_c} \tag{6.1}$$

where N_c is the number of chambers in the overall system. The actuation pressure is recorded by pressure switches with a range of -100 kPa to $+1000$ kPa (ISA80 Series, SMC). For each unique robot configuration in time step k, the tip position $p_k \in \mathbb{R}^3$ and the unit normal vector $n_k \in \mathbb{R}^3$ of the end-effector are collectively represented by a robot configuration $\upsilon_k = [p_k, n_k]^T \in \mathbb{R}^6$.
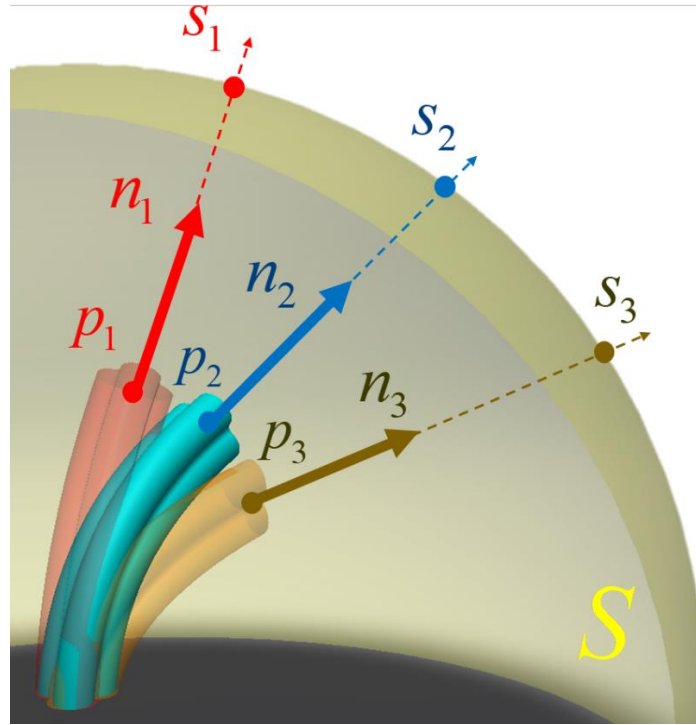
Fig 6.1   Soft robot configurations under various inflation pressures. Corresponding targeting point s_k on intracavity surface S (yellow) showing position of manipulator end-effector at p_k along the unit normal vector n_k, where $k = 1,2,3$.

In order to smoothly navigate the targeting point on the intracavity task space S, all of the deformation mappings are transformed into the task space (**Fig 6.1**). By projecting the principal axis of manipulator end-effector to the intracavity surface S, the intersection point s_k is given by:

$$s_k = p_k + n_k t \tag{6.2}$$

where t is a scalar projection distance to the intracavity task space S. To provide intuitive human-robot interaction during navigation, we have established reliable visual guidance that accommodates visual-motor re-alignment. It is achieved by attaching a virtual camera coordinate L at the end-effector coordinate with its principal axis aligned with its Z-axis of the robotic tip (**Fig 6.2**). A virtual camera view then visualizes the pre-defined trajectory and intracavity surface S in the image coordinate. This visual guidance realigns the visual-motor mapping of Jacobian matrix and hence enhances the hand-eye coordinate of operators. As they can issue desired incremental end-effector motion in the planar image coordinate, which simplifies the control complexity by reducing the required control input into a two-dimensional vector $\Delta y \in \mathbb{R}^2$ in the image plane.
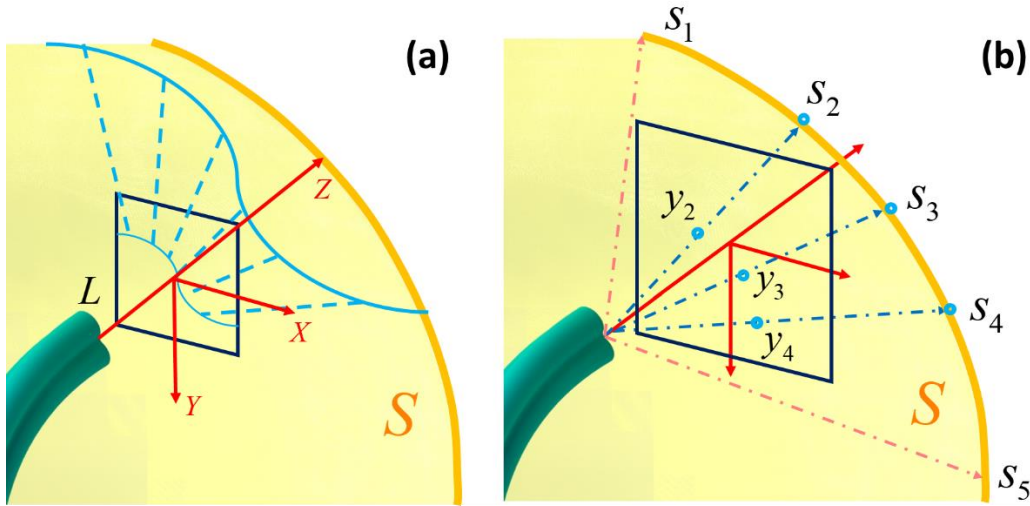
Fig 6.2 Illustration of virtual camera view provided to operators during tele-operative navigation. **(a)** Estimation of Jacobian matrix for motion mapping with respect to the image coordinate **L**. **(b)** Neighbor targeting points s_2, s_3, s_4 on intracavity surface **S** (yellow) projecting to camera coordinate **L** (red) as y_k. Camera coordinate is used for local kinematics linearization. Other targeting points s_1, s_5 are neglected, as they are out of the kinematics field of view.

As illustrated in **Fig 6.2**, we assumed there is a kinematics field of view (FOV) of the current camera coordinate **L**. Z-axis in camera coordinate **L** is projected in a particular actuation pressures to the intracavity surface **S** (**Fig 6.2a**). This projection vector passes through a virtual image plane as:

$$y_k = [d_x, d_y]^T \in \mathbb{R}^2 \tag{6.3}$$

A set of local kinematics mapping $M = (y_k, u_k)$ can hence be obtained. By differencing the control pressure u_k with the previous time step *k-1*, the change in pressure is given by Δu_k in step *k*:

$$\Delta u_k = u_k - u_{k\text{-}1} \tag{6.4}$$

The end-effector is displaced by Δy in camera coordinate **L** corresponding to the change of pressure Δu. The linear kinematics model can be formulated by a Jacobian matrix that linearly maps the actuation pressure to targeting point displacement Δy with respect to the origin of the image plane:

$$\Delta y = J \Delta u \tag{6.5}$$

Each row of the Jacobian matrix is found by least square fitting method as formulated below at every control iteration.

$$\min_{J_1} \frac{1}{2} \left\| \begin{bmatrix} u_0^T \\ u_1^T \\ \vdots \\ u_h^T \end{bmatrix} J_1^T - \begin{bmatrix} d_{x1} \\ d_{x2} \\ \vdots \\ d_{xh} \end{bmatrix} \right\|_2^2 \quad , \quad \min_{J_2} \frac{1}{2} \left\| \begin{bmatrix} u_0^T \\ u_1^T \\ \vdots \\ u_h^T \end{bmatrix} J_2^T - \begin{bmatrix} d_{y1} \\ d_{y2} \\ \vdots \\ d_{yh} \end{bmatrix} \right\|_2^2 \qquad \textbf{(6.6)}$$

where $J_i \in \mathbb{R}^{1 \times h}$, h is number of mapping samples, and $\| \cdot \|_2$ is the L-2 norm operator

for the vector.

6.1.2 Learning-based Feedforward Control of RSR

To simplify the modeling process, the piecewise constant curvature (PCC) assumption is one of the widely-used techniques [146, 147, 149, 151] to obtain close-formed solutions [152, 153]. This enables real-time kinematic control of curvature discrepancy to attain the desired pose [154] and to perform dynamic motion primitives [155] for fluidically-driven soft continuum robots. The parameters that govern the analytical models can also be estimated online [156]. Other model-based methods have been proposed without taking the PCC assumption, such as approximation of trunk-like structures to infinite degree-of-freedom (DoF) system [157], and modeling spring-mass modeling techniques [158, 159] which can be incorporated in a hierarchical controller for generating stereotyped motions of an octopus-like manipulator [158]. Recently, the Cosserat theory [160] of elasticity has been used to predict underwater motion of a cable-driven, octopus-like soft robot [161] by deducing its geometrically exact formulations. Yet, external disturbance to the robot, such as gravity, payload and external interaction, can promptly invalidate those assumptions. These over-simplified assumptions would substantially degrade the model's reliability in real applications. Inevitably, the analytical model needs to be revisited after any major change to the robot structure, further diminishing the effectiveness of such an approach.

With the foreseen difficulty of developing the kinematic model, research attempts were made to control the soft, pliable robot using non-parametric, learning-based approaches. The idea is to obtain forward and inverse mappings for kinematics

robot control based on measurement data only. Model-free control methods can also be developed based on direct modeling architecture [162], where the inverse mapping is directly obtained. This mapping depicts the inverse transition model of the robot, which could be a changing function due to the contact between the robot and the environments, such as soft tissue. The use of NN has been proposed to globally approximate the inverse mapping between end-effector and robot actuation [163, 164]. Such an approach can compensate for uncertainties in robot dynamics [163], and has been demonstrated to yield even more reliable solutions when compared to using an analytical model of a cable-driven soft robot [164]. Previous studies of NNs mostly consider simplified scenarios, such as a non-redundant manipulator and contact-free situation [163, 164].

Although redundantly actuated robotic systems can be controlled in lower dimensionality in a hierarchical manner, it may require pre-defined movement patterns for specific task goals [158]. Moreover, there has been a great demand on using machine learning approaches to address the change in inverse mapping of the hyper-elastic robot upon contact [91]. A Jacobian-based model-free controller has shown its capabilities to manipulate a planar cable-driven continuum robot in an environment with static constraints [165]. Stable feedforward control [166, 167] has been done without sensory feedback with a self-stabilizing controller. In the MATLAB NN toolbox, there are three kinds of non-linear regression algorithm, namely Levenberg-Marquardt training, scaled conjugate gradient and Bayesian regularization. Levenberg-Marquardt and scaled conjugate gradient generalization algorithm automatically stops when indicating an increase in mean-square error (MSE) of validation samples. Both algorithm results in a quick artificial NN with high variance. However, the variance in Bayesian regularization approach has the smallest among three algorithms. This algorithm typically spends more training time, but can result in a better generalization for difficult, small or noisy datasets and stops according to adaptive weight minimization. In our research, the NN training takes place pre-operatively, there are adequate time to perform non-linear regression algorithm by Bayesian regularization to yield a controller with high accuracy.

The training data acquisition protocol is described as followed. Firstly, the actuation pressures for three principal chambers are inputted individually. The tip position p_k and unit normal vector n_k are recorded by the electromagnetic (EM) tracking probe. Secondly, intermediate angular points are linearly interpolated with a same pitch angle. A virtual projection plane in a 15 mm distance away from the initial end-effector tip. After datalogging a set of cloud data, inverse kinematics is calculated with the mapping between the actuation pressures u_k and the corresponding projected position y_k on the camera coordinate L.
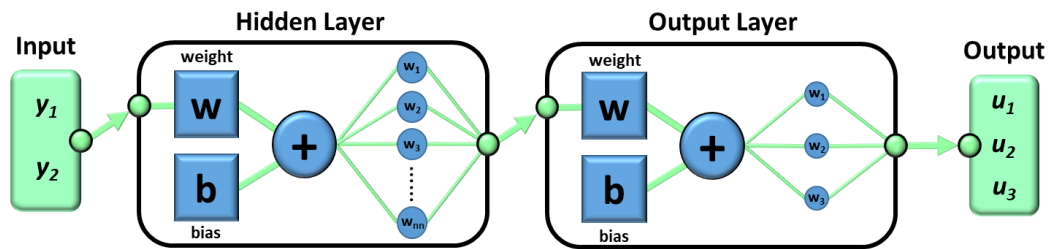
Fig 6.3 Schematic Diagram of the artificial NN by MATLAB fitting tool. Complexity of fitting network depends on the number of neurons *nn*. Each neuron holds different weighting value that construct a generalization network for datasets.

Sample projection points ($N = 72$) are traced with pitch angles θ of 10º, 20º and 30º (**Fig 6.4**). The inverse kinematics of the robotic actuation is then trained by the neural fitting network in MATLAB. With the trained NN function, correlation between the volumetric fluid input and the kinematic characteristics is estimated. By designing a desirable trajectory Δy in the virtual projection plane, the differentiated actuation chamber pressures Δu are calculated. A circular trajectory is modeled in task space and recorded the corresponding actuation pressure by the trained NN function. Preliminary testing is performed by plotting a circular trajectory with the trained NN with the number of training samples (**Fig 6.5**).
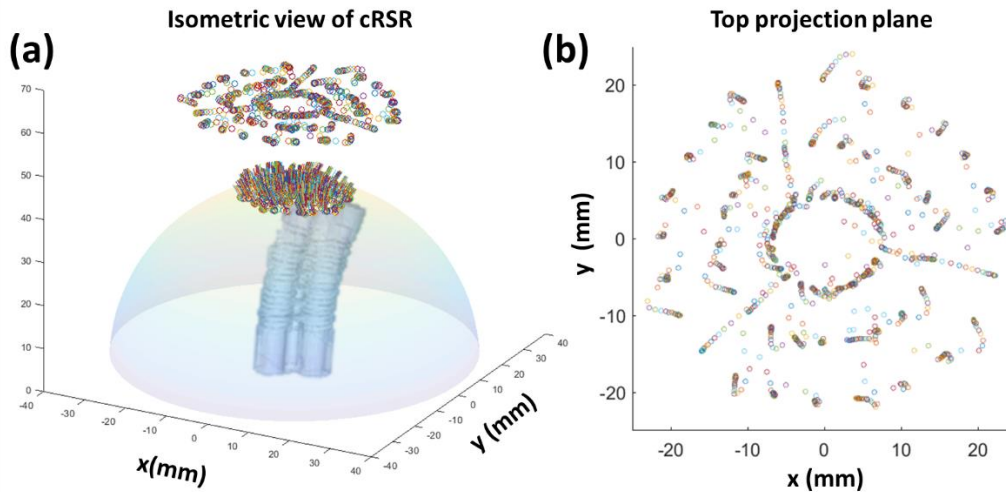
Fig 6.4   Demonstration of data acquisition protocol for RSRs' NN training. **(a)** Tracked positions and normal vectors of cRSR of $\theta = 10^\circ$, 20°, 30° shown in isometric view. **(b)** Virtual projected plane placing in 15 mm apart from the robotic tip. Projection points ($N = 72$) are recorded by an EM tracking system. Projection points with identical pitch angle are separated by 15° in angular distance.

However, the actual trajectory (**Fig 6.5a**) is not accurately projected as a circular trajectory due to two possible reasons, which are: **(i)** hysteresis of the elastomeric material and **(ii)** lack of NN training sample. The hysteresis effect is investigated in **Section 5.4.3** that can be reduced by using hydraulic actuation, but inevitable. As a result, we should increase the sample size of data acquisition for the NN training. Having the simultaneous pressure feedback during the training, we found that the pressure cycle for a circular trajectory can be modeled as a sinusoidal curve shown in **Fig 6.5b**. An absolute sinusoidal curve in **Fig 6.5c** is then modeled with a phase difference of $2\pi/3$, and $u_k \geq 0$. However, when the RSR is trained by the modeled sinusoidal curve, the neural fitting curve found a set of samples that is not fitting to the regressive curve with $R^2 = 0.94716$ in **Fig 6.5d**. It is due to the discontinuity of the sinusoidal curve by the condition of $u_k \geq 0$.

In view of unfitting samples with unsatisfied least square R^2 with pressure discontinuity, we modeled the applied pressure with an offset of half of its maximum amplitude to formulate a continuous sinusoidal curve in **Fig 6.5a**. Moreover, instead of plotting equipotential circles with same pitch angle θ, I proposed to train the RSR with an incremental amplitude in **Fig 6.5b**.
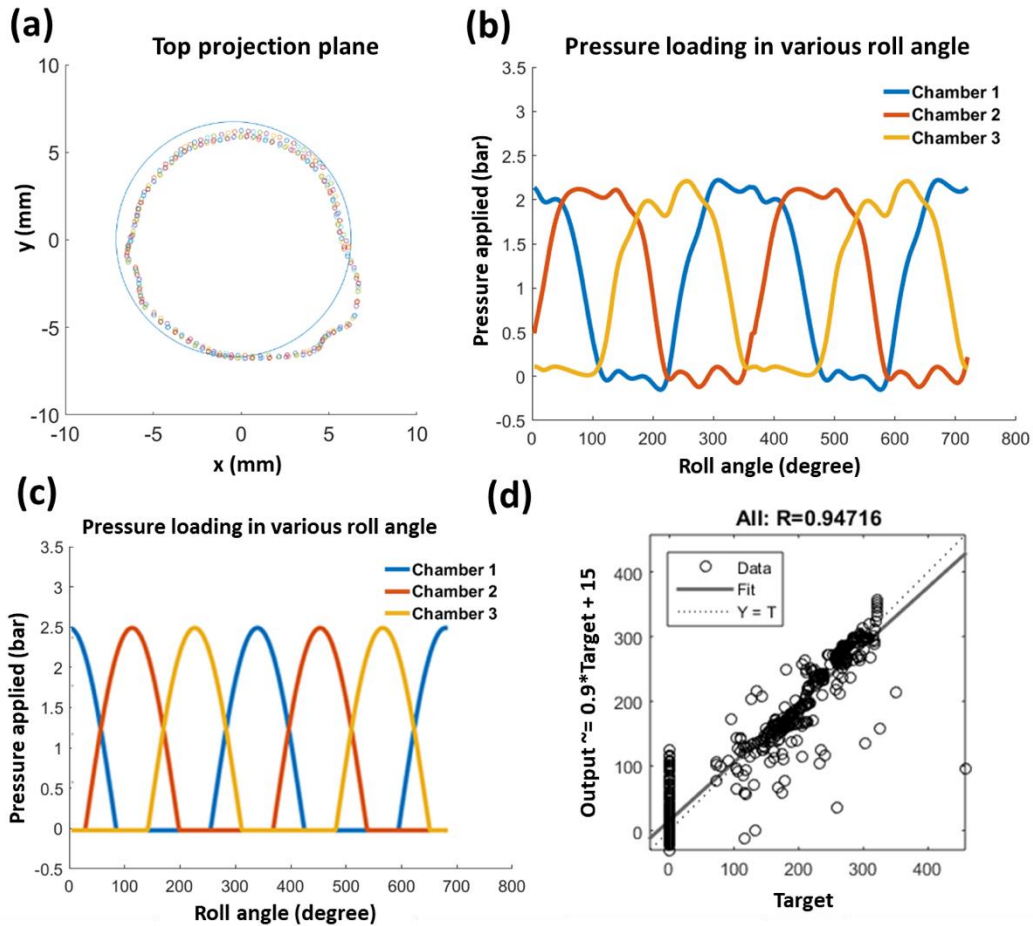
Fig 6.5 cRSR following a circular trajectory trained by NN function. **(a)** Virtual top projection plane illustrating deviations from the desired circular path. **(b)** Pressure feedback from pressure switch of three distinct chambers. Pressure feedback demonstrated a sinusoidal trend with a $2\pi/3$ phase difference from another chamber. **(c)** Modeled sinusoidal curve with discontinuity at zero pressure per half cycle. **(d)** Least square regression fitting of NN training sample versus output prediction with $N = 196$ and $R^2 = 0.94716$. Regression results show mismatch inverse mapping for target = 0 due to discontinuity modeling at zero pressure.
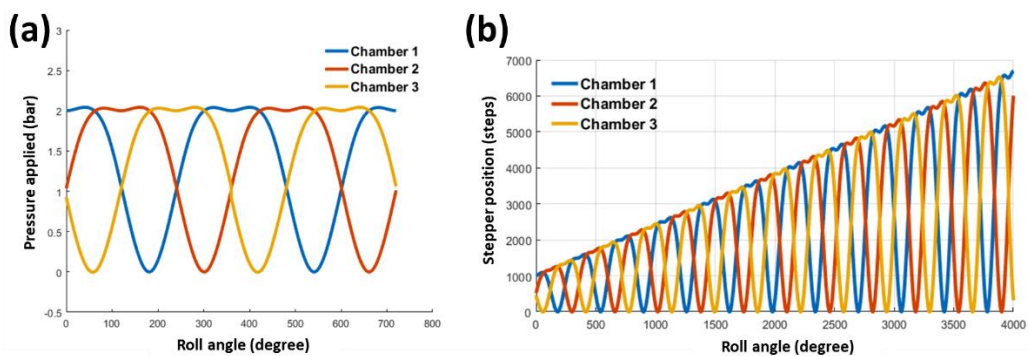
Fig 6.6 **(a)** Sinusoidal actuation pressure curve without discontinuity. **(b)** Step-increasing function of continuous pressure curve. Increasing amplitude of stepper motor position causes gradual increase of laser scanning range in virtual projection plane.

109

Training of RSR projected a semi-triangular cycle with increasing projection diameter shown in **Fig 6.7**. The NN training result in the neural fitting curve shows a promising regressive curve ($R^2 = 0.99982$) by continuous actuation modeling with $N = 3512$ and 20 training neurons.
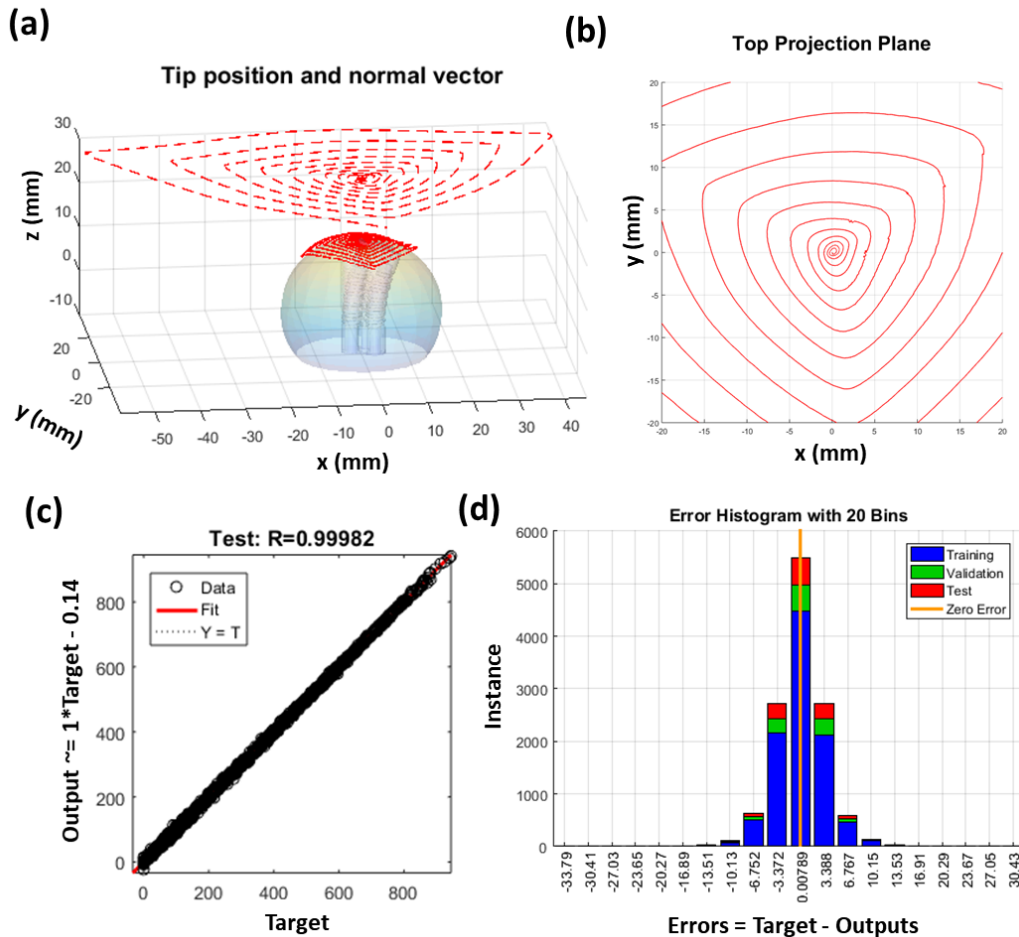
Fig 6.7   **(a)** Isometric view of semi-triangular cycle with increasing projection diameter. **(b)** Top view of virtual projected plane. **(c)** NN training of the fitting sample data versus output prediction with $N = 3512$, $R^2 = 0.99982$. **(d)** Training error histogram with error range less than 1% with respect to the maximum actuation steps. 80% of sample data are used for neural network training, 10% for validation and 10% for testing.

During the NN training process, a triangular shape is obtained due to the bias from three principal chambers. In the NN training, 80% of the sample point is used for data training, 10% is used for validation, and the last 10% is used for testing. Training error range is less than 15 steps among stepping range in a magnitude of 10^4 (less than 1% error). With the trained NN, an inverse kinematics controller is used to deduce the input actuation pressures for the desired trajectory. With the promising training prediction that is validated by the NN tools in MATLAB, experimental validation of RSR is necessary as the effect of hysteresis is yet to be

eliminated. In **Section 6.2**, the accuracy and reliability of RSRs are examined by path-following tests with various projection patterns other than circles (i.e., spiral and polygon). The cRSR and fRSR are integrated to test the laser dissection effect to validate the correlation of the task space with the EM tracking coordinates. The robotic control is a feedforward control by the trained NN function. Assumed the 6D EM tracking probe has a similar mechanical property with the gradient-index (GRIN lens collimator, the desired dissection margin is measured and registered by the 6D EM-based positional tracking probe (Ø0.8 mm × 9 mm). The robot feedforward controller is calibrated in task space with respect to the EM tracking coordinates. Proximity and differentiation angle from the EM marker to the desired dissection is captured to evaluate the targeting accuracy. In this section, the continuous actuation model in **Section 6.1.2** is employed to the fRSR. After tracking by the EM marker, the process is repeated by replacing the 6D EM tracking probe into the GRIN lens collimator. The correlation is determined by the similarity of the experimental laser dissection pattern (**Fig 6.8a**) and in the virtual projection plane (**Fig 6.8b**). The pattern found to be fitted in **Fig 6.8c** and proved the EM Tracking probe has a similar mechanical property with the GRIN lens collimator.
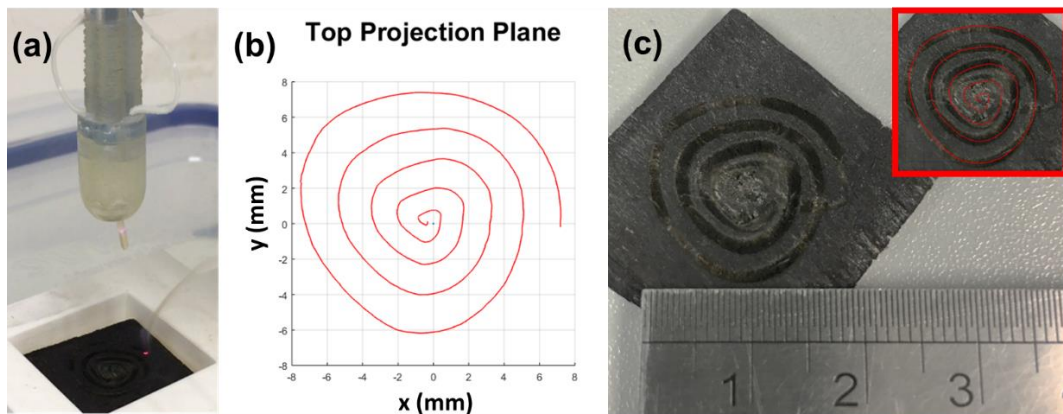
Fig 6.8   **(a)** Actuation of fRSR with 808-nm 2W laser. Laser collimator is deflected and controlled by fRSR. Laser ablation is performed on the black color-dyed wood. **(b)** Virtual projection pattern acquired by inputting step-increasing continuous pressure function to fRSR actuator. Positional information is measured by EM tracking probe. Recorded position calculated as a virtual laser dissection pattern on the top projection plane. **(c)** Overlapping virtual projection pattern to the actual ablated pattern showing similar laser cutting pattern.

6.2   PERFORMANCE OF RSRS

The performance of the two segments of the actuator is evaluated individually. We used spiral trajectories as a path following task to evaluate the performance of RSRs and compared with µRALP. The cRSR with a projection plane distanced in 15 mm have the same scanning area of 20×20 mm^2 as the µRALP with a bending angle of 30º. Resultant chamber pressure is similar to the pressure model in **Fig 6.5**.

6.2.1   Accuracy of cRSR

A 20 mm spiral trajectory with 1 mm pitch is modeled in the virtual projection plane (**Fig 6.8**). The accuracy of the robot is calculated by the mean tracking error and root-mean-square (RMS) error with respect to the desired spiral trajectory. In 10 cycles of spiral path following task, the mean error is 0.5926 ± 0.3835 mm. Moreover, it is found that the tracking error increases with the bending angle. cRSR has a sub-millimeter deviation error and enables to have a coarse aiming to the cancerous target.
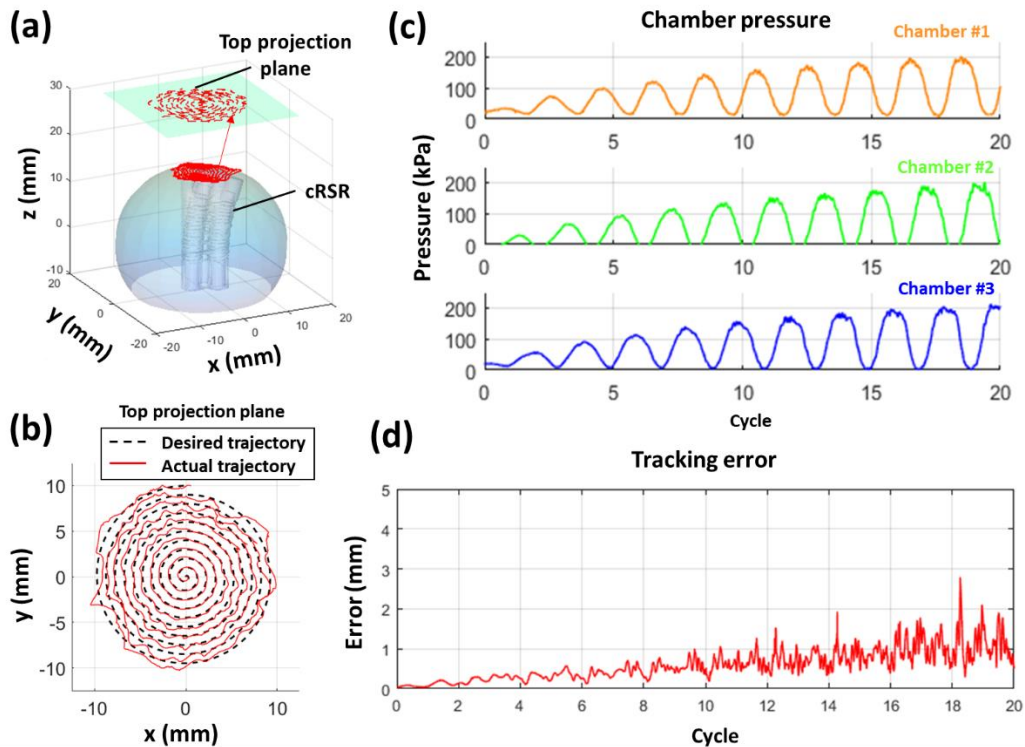
Fig 6.9   **(a)** Isometric view of cRSR following spiral trajectory. **(b)** Top projection plane comparing 20 mm spiral trajectory with the actual path. **(c)** Three chamber pressures showing $2\pi/3$ phase difference and increasing amplitude in pressure along 20 cycles. **(d)** Path deviation error in planar distance of the projection plane with mean error of 0.5926 mm and root-mean-square error of 0.3835 mm.

112

6.2.2 Accuracy of fRSR

As the cRSR is approximately aimed at the tumor region, fRSR shall be accounted for the overall precision of the system once the cRSR set in place. Therefore, the projection scanning area for fRSR should be less than cRSR, but with higher accuracy. The size of the oral cancer tumor identified by MRI has a mean of 4.04 mm and 3.08 mm in length and width respectively [168]. The fRSR with a projection plane distanced in 15 mm have a scanning area of 8×8 mm^2 with a bending angle of 20º. As a result, we proposed to use a spiral with 1 mm-pitch and a maximum diameter of 8 mm as a path following task for the fRSR (**Fig 6.10**), which covers the 4 mm tumor from either side. In 3.5 cycles of spiral path following task, the mean error is 150.0 ± 83.5 μm.
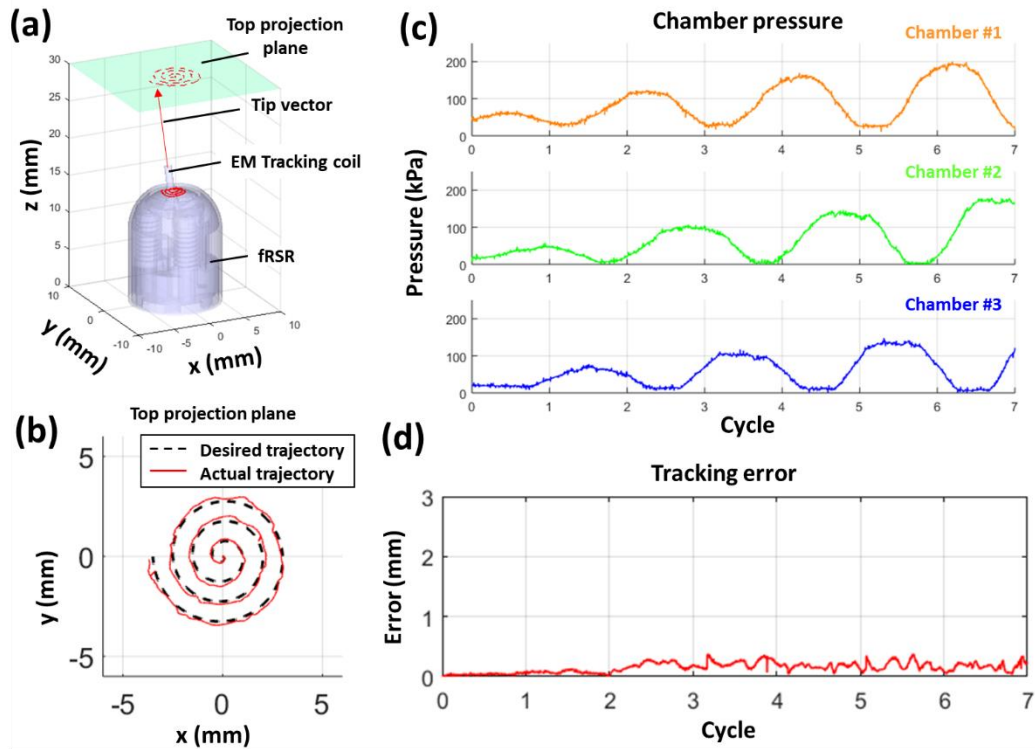
Fig 6.10   (a) Isometric view of fRSR following a spiral trajectory. (b) Top projection plane comparing 8 mm spiral trajectory with the actual path. (c) Three chamber pressures showing $2\pi/3$ phase difference and increasing amplitude in pressure along 7 cycles. (d) Path deviation error in planar distance of the projection plane with mean error of 150.0 μm and root-mean-square error of 83.5 μm.

6.2.3 Reliability of RSR

Having a sub-millimeter tracking error for both cRSR and fRSR, we should also evaluate the repeatability of the robot to follow the same desired path in numerous cycles. In this experiment, we propose to use a polygon-shaped trajectory for path following test, which is different from the semi-spiral training pattern. A pentagon trajectory is employed as the testing trajectory with five interior angles. The 108° internal angles caused a discontinuity in trajectory and can also evaluate projection accuracy. By choosing a non-multiple number to principal chambers, asymmetry pattern of the actuation pressure is arisen, meaning the portion of actuation pressure for each chamber in one cycle is differentiated (**Fig 6.11**).
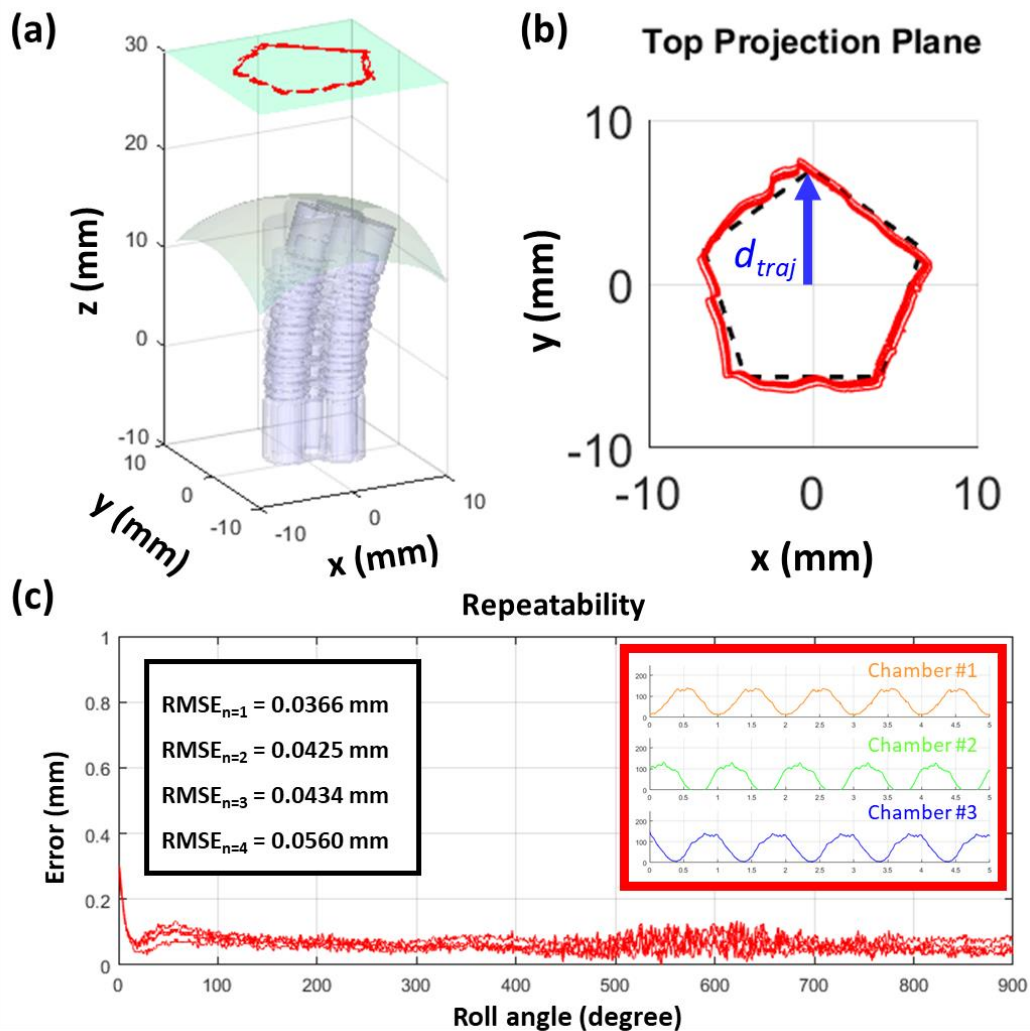
Fig 6.11   **(a)** Isometric view of cRSR following pentagon trajectory. **(b)** Top projection plane comparing actual path with the desired trajectory distance of d_{traj} = 8 mm. **(c)** Repeatability of RSR evaluated by comparing the difference with first drawn trajectory. Root-mean-square errors for four repeated polygon paths are evaluated as a mean precision error of 44.6 ± 8.2 μm.

The reliability of cRSR is calculated by the difference in projection distance with respect to the first drawn trajectory. Even for the polygon shape trajectory with sharp corners, the repeatability task demonstrated the mean precision error of 44.6 ± 8.2 μm. This shows a highly repeatable path with sub-millimeter deviation from the previous cycles. Two path-following experiments have ensured an accurate and precise laser dissection operation.

6.2.4 Laser Dissection Test on *ex-vivo* Tissue

The trained cRSR and fRSR are assembled to test on the laser dissection effect on the *ex-vivo* pig tongue tissue. Various patterns were selected such as circle and square (**Fig 6.12**). In this actual laser tests, the targeting accuracy was visually evaluated by tracing the ablation effect along the black color-dyed margin in the phantom tumor and evaluated in the MR images in **Section 6.3**.
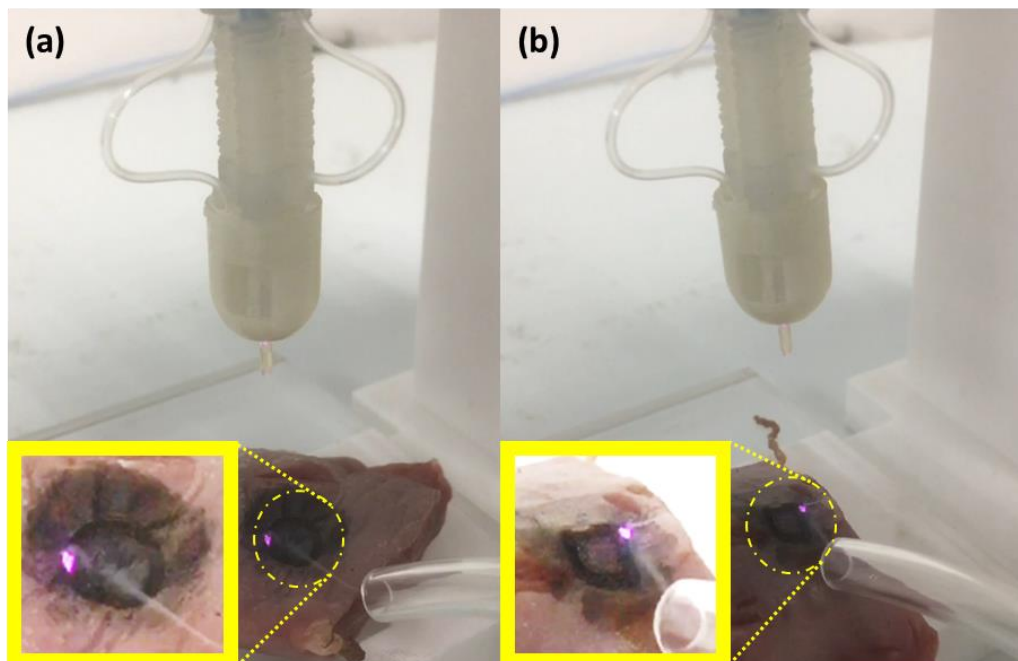
Fig 6.12   Laser dissection test on *ex-vivo* pig tissue with air evacuation tubing. Path following by cRSR of two laser dissection patterns of **(a)** circle and **(b)** square.

Optimal control parameters are set to coordinate the bending and insertion motion of the overall endoscope. Laser dissection effect will be evaluated in the subsequent MRI trials. In the *ex-vivo* test, two projection patterns are set, which are circle and square. With an 808-nm visible laser, a black color-dyed pig tissue is required to enhance the absorption efficiency. The laser dissection trace showed a circular track and a square with slight deformation. The deformation of the projected trajectory is

due to the irregular surface of the *ex-vivo* tissue. By further studying MR thermometry in the future and gaining real-time coordinate mapping from MRI system, the correlated actuation pressure u_k can be fine-tuned during a surgical operation.

6.3   FEASIBILITY TEST IN MRI ENVIRONMENT

In order to evaluate the MR-safety of the robotic slave system in the MRI room, the material composition shall be intrinsic non-ferromagnetic. cRSR and fRSR actuators are 3D printed by resin. Hydraulic transmission tubing is made of clear polyurethane (PU) tubing (TU0212C-20, SMC). Laser fiber and the GRIN lens collimator is made of silica and glass respectively. All of the components are chemically inert and non-ferromagnetic. However, the MR-compatibility test of the RSRs are evaluated by measuring the signal-to-noise ratio (SNR) on the MR images. MR-compatibility test was conducted in a 1.5T MRI scanner (SIGNA™ HDxt, GE Healthcare, USA) at room temperature of about 20°C. The MRI unit is located at the Hong Kong Jockey Club for Interdisciplinary Research, Queen Mary Hospital.

6.3.1   Signal-to-Noise Ratio (SNR) Test

The MR-compatibility of the robot system is evaluated by the SNR test, comparing the noise artifact ratio in the overall image with the control phantom. SNR testing used a T1-weighted gradient echo (GRE) and T2-weighted fast spin echo (FSE) sequences for each stage.

The protocol of SNR testing has four stages. First, a rectangular SNR phantom was placed at the isocenter of the scanner, which provides a baseline image without the presence of the robot. Upon introducing the robot right beside the phantom, MR images were obtained under three robot operating conditions. The four stages are classified as follow, show in **Fig 6.13**:

(i)	**Control**:	No Robot is introduced;
(ii)	**Static**:	Robot is introduced and remains powered off;
(iii)	**Powered**:	Robot remains still, but the hydraulic/electric power is on;
(iv)	**Operating**:	Robot is in full operation.

MR image artifacts caused by the presence of robot were quantified based on the American Society for Testing and Materials (ASTM) standard test method [169] and is MR-safe for the robotic system. These artifacts will appear as white pixels in the binary map (FSE Artifact). No artifact was observed within the phantom area. As defined by the ASTM-F2119 standard, it indicated the operation of robot-generated zero artifact.

(i) Control Image   **(ii)** Robot in Static   **(iii)** Robot Powered   **(iv)** Robot Operating
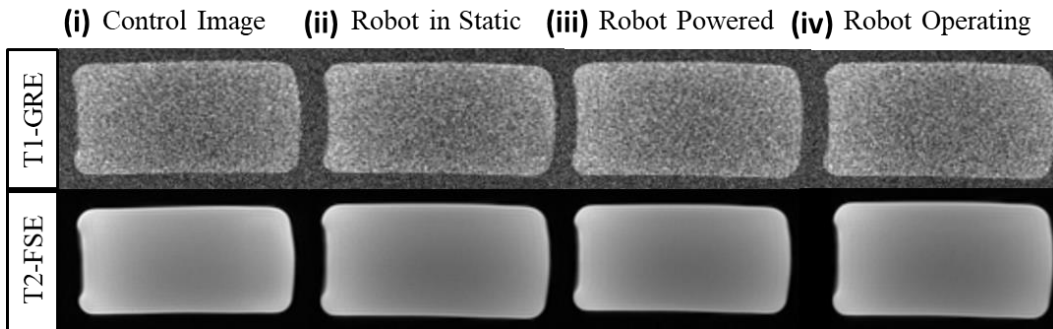
Fig 6.13   MR images of four robot operating conditions and binary map for artifact analysis: **(i)** control image with a rectangular SNR phantom, **(ii)** robot in static without power, **(iii)** robot in static with power on, and **(iv)** robot in motion and operation with power on.
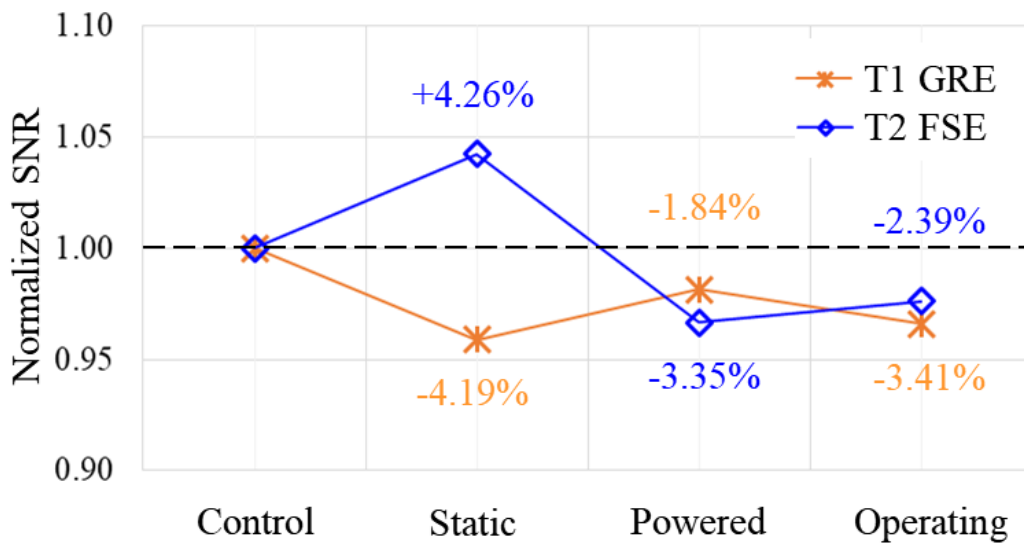
Fig 6.14   SNR test in T1-GRE and T2-FSE. Artifact is defined as more than 30% intensity variation compared with baseline zero artifact phantom. Both MRI sequences have shown less than 5% normalized deviation in artifact percentage calculated by signal-to-noise ratio.

As the results shown in **Fig 6.14**, SNR loss is within 4% even with the robot in full motion, which is less than a 30% difference in pixel intensity. In SNR tests, the signal is normally lost rather than gained, but there is an increase in SNR for T2-FSE in static condition. Possible reason of this relatively-large SNR may be due to the aluminum coupler in laser collimator. This can be improved by the proper

selection of a totally MR safe laser collimator and any other supplementary tools. In conclusion, the robotic slave system is MR-conditional with zero artifact as defined by the ASTM-F2119 standard.

6.3.2 MRI localization by wireless microcircuit

During the operation, the Cartesian MR coordinate of the robotic system was calibrated by MRI-based wireless inductive coupling microcircuit. Three radiofrequency (RF) microcircuit were embedded in the dental guard to provide active 3D tracking. RF markers were located for a distance (> 20 mm) from the cancerous target. Therefore, the blooming effect by the RF markers will not affect the MR image quality in the target region. In addition, these markers were presented during SNR tests with normalized SNR < 30%, that proves their MR-compatibility. To selectively activate the RF microcircuit, 3D GRE imaging was used with lower flip angle of 2°. As a result, the background signals can be minimized by this dedicated excitation sequence with low flip angle. Resultant MR image (**Fig 6.15**) shows three tiny bright spots indicating the location of the wireless markers. In contrast to the background signal at a 1340-pixel circular area with an average intensity of 658, the signal intensities of the tracked markers were 3195, 6348 and 7129.
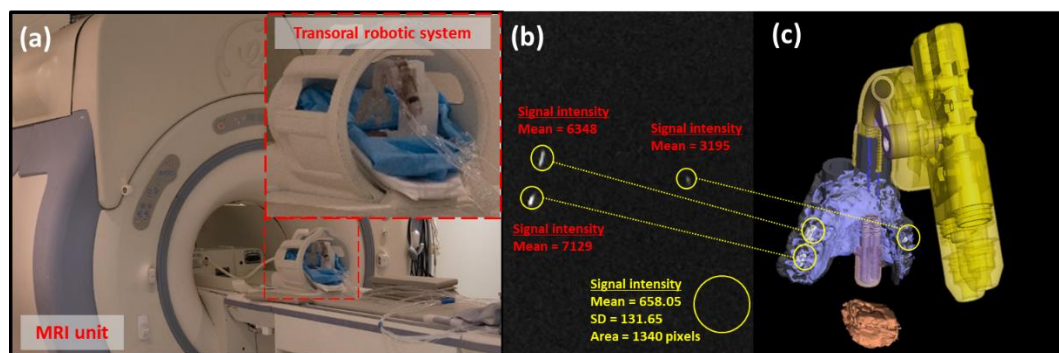
Fig 6.15   **(a)** Transoral robotic system (slave) inside MRI unit in Hong Kong Jockey Club for Interdisciplinary Research, Queen Mary Hospital. **(b)** MR images showing intensity signal by MRI-based marker scanned at 1° flip angle. **(c)** Dental guard (purple) and *ex-vivo* tissue (orange) reconstructed by MR images. Robotic system (yellow) is overlaid onto the reconstructed scenario.

MRI localization takes place in the beginning of the whole operation by 3D GRE, which provides the relative position of the cancerous region with respect to the robotic system. This pre-operative MRI enables the reconstruction of the whole oral,

nasopharyngeal (ONP) workspace as a baseline. During the laser dissection, only a few principal MR frames are reconstructed and updated to visualize the temperature mapping. As the result, the laser targeting position is located by MR thermometry.

6.3.3 Laser Dissection Test under MRI

After proving the MR-compatibility of the robotic system by SNR test, we further performed a laser dissection test in the MR environment with the *ex-vivo* pig tongue (**Fig 6.15**). The robot is controlled tele-operatively via a 10-meters hydraulic tubing passing through the waveguide of the control room. Thirty-cycle ablation was carried out in total and the ablation time was ten minutes. To monitor the ablation progress, MR imaging was performed to update the physiological changes of target lesion, as shown in **Fig 6.16a-d**. A smooth circular slot can be observed in the images. Dexterity and precision of the presented robotic manipulation has been demonstrated.

A circular pattern is inputted for the laser trajectory with a diameter of 8 mm. The *ex-vivo* tissue is dissected with an 808-nm laser with 3.6 W. As the absorption efficiency of illustration 808-nm laser is low, the *ex-vivo* tissue is black-dyed to enhance laser energy absorption. A higher wavelength 1470-nm laser is more favorable to be used in the future. Laser dissection task is repeated for 3 times, with 10 circular loops per cycle in 90 seconds, causing a total laser dissection period of 270 seconds. Since 3D T1-GRE were performed for every 10 loops, comparing the laser incremental dissection effect stage by stage.

With the 3D reconstructed images by InVesalius, it is found that the circular track has a diameter of 7.627 mm to 7.785 mm in *x*-direction and *y*-direction in **Fig 6.16e**. After 30 circular laser dissection, the *ex-vivo* tissue has an incision depth of 1.215 mm. However, the incision power and depth vary by the configuration of the 10 meters laser fiber, which changes during setup of the robotic system. The incision depth is determined post-operatively by MRI scan, but the incision depth could also be determined intra-operatively by the MR reconstruction.
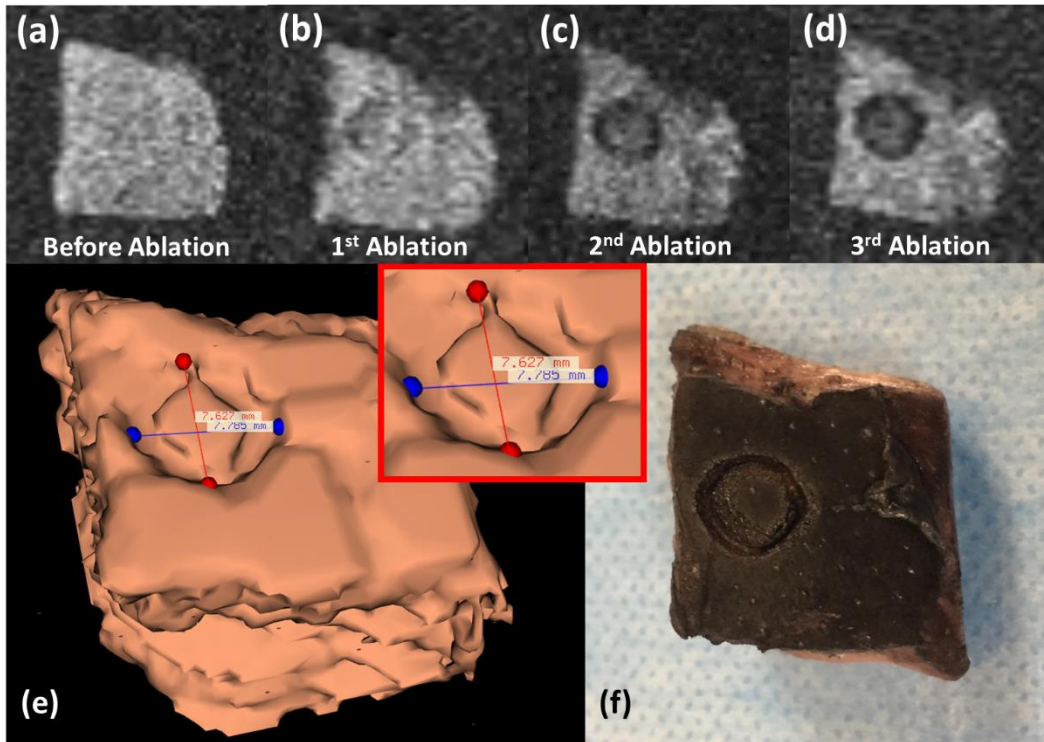
Fig 6.16 Evaluation of laser dissected *ex-vivo* pig tissue via DICOM reconstruction software. **(a)** Control image before ablation. **(b)** Ablation with 10 loops. **(c)** Ablation with 20 loops. **(d)** Ablation with 30 loops showing a circular dissection trace on ex-vivo tissue under MRI. **(e)** 3D reconstructed *ex-vivo* pig tissue dissected by a circular pattern. Laser dissection diameters in two axes are 7.627 mm and 7.785 mm in the *x*- and *y*-direction respectively. **(f)** Black-dyed pig tongue enhanced laser absorption efficiency.

6.4 RESEARCH LIMITATIONS

The 3D printed soft robotic actuators can withstand high pressure compared to the traditional soft robotic tentacles with hydraulic actuation. The NN training network shows a promising correlation for the positional targeting with the stepper motor position (pressure applied) to the robot. However, it is found that the NN mapping relationship only kept accurate within 12 hours, beyond which the output actuation is less than the input control. For example, the desired circular trajectory with diameter d_{traj} of 8 mm will be dissected as a circle with less than 8 mm in diameter. The main reason is due to the pressure relaxation because some part of the robotic system has pressure under ambient pressure. Therefore, air is drawn into the transmission tubing by pressure difference and becomes air bubbles. Most importantly, the mapping is no longer held by the previously trained NN network, as the fluid volume is varied with respect to the stepper position. With the air bubbles, the volumetric mapping is changed. The problem of inhomogeneous actuation fluid over time can be alleviated by the following measure. It can be done by setting a higher preloading pressure, such that the robot is pressurized in every part. No negative pressure is accumulated, and air bubbles introduction can be avoided. However, the robotic system is withstanding a constant preload stress in a normal state, and the lifespan of the robot is reduced.

Another limitation is the current accessed MRI unit does not have the MR thermometry function that the laser projection site is not visible in the MR images. As a result, we could only have a feedforward control for validating the robot performance, but not a close-loop control under MRI. The last limitation is the source of funding and the long procurement process for the A.R.C. laser device. Therefore, we used 808-nm laboratory-based laser instead of 1470-nm laser with favorable laser dissection effect. Even though we can use a black color-dyed phantom to enhance the absorption of the tissue, it does not truly reflect the absorption behavior of the tissue.

6.5 CONCLUSION

In this work, a spring-reinforced soft robot (RSR) with detailed design and analysis workflow is presented. Using additive manufacturing technology, the robot composed of the non-ferromagnetic and non-conductive component. MRI compatibility test has also been performed to validate the minimal imaging interference during robot operation. The entire robotic system passed SNR test with no artifact and can be claimed to be MR-conditional.

Finite element analysis (FEA) was conducted to study and optimized the robotic parameters and to predict the rigidity and stability. The steady, smooth and consistent motion control of this long, thin and flexible continuum robot has been validated. The robotic positional information is measured by 6D EM tracking system and mapped by an NN machine learning algorithm. The flexible and dexterous cRSR and fRSR are assembled into a two-segment design for active steering. cRSR segment has longer chambers for coarse angular bending, max. ±60°. While fRSR segment fully covered by a rigid outer constraint is designed to steer the laser collimator at ±30° within the confined operating space. This 4-DoF robotic system is coupled with the hydraulic advancement mechanism to add an extra insertion DoF to form a 5-DoF actuation system. Even the RSR only has 2-DoF (pitch and yaw) compared to surgical tool of da Vinci Surgical System, the robotic compliance of soft robotic endoscope lowers the navigation requirement in the ONP workspace. Moreover, reliability of the inexpensive 3D printed actuator has not been compromised and has demonstrated sufficient accuracy and precision with average errors of 150.0 ± 83.5 μm and 44.6 ± 8.2 μm respectively. The fabrication is easy and can be accomplished by directly 3D printing using digital materials. It is low-cost and disposable for the ease of medical sterilization.

The robotic system is equipped with flexible laser fiber to deliver laser power in a non-contact manner with high *PD*. Unlike disposable ball-tip laser fiber that burns the laser tip after usage, this non-contact laser projection approach protects both the laser collimator and the actuator from high temperature. A patient-specific dental

guard is fabricated as a static anchorage on the patient oral anatomy. In addition, miniaturized RF tracking markers provide positional data in MR imaging coordinates for an MRI-based laser dissection task. Laser dissection progress is monitored by intra-operative MRI. A smooth, homogeneous, circular trace can be readily identified under the MRI, which has demonstrated the capability of the soft robotic manipulator to perform accurate controllable tissue cutting.

6.6 FUTURE WORK

Further studies will be conducted to correlate the MR coordinate system with the actual task space. Moreover, the MR thermometry will be investigated and performed by adjusting the MR temperature-sensitive parameters, such as proton resonance frequency, leading to MR susceptibility with high SNR by a fine change of temperature in the accuracy of $< 1°C$. Also, the laser intensity will have to be tuned so that little temperature rise on the *ex-vivo* mucosal tissue can be measured under the MR thermometry. Online MR estimation of the laser incision depth can also be done to evaluate the degree of tumor dissection. In addition, more FEA will be done to enhance robot robustness and stability. With a higher-end printing technology in the future, 3D-printed actuators can be further miniaturized with thinner wall thickness and reinforcement constraint. By using an elastomeric material with higher ultimate tensile stress (UTS), the force output of the actuator can be improved. Moreover, this soft robotic manipulation system is the first MR safe soft robotic manipulator for transoral tumor dissection. Its compliance and compact design ensure the safe interaction with patient anatomy and flexibly access to the deep ONP lesions. Other than Endotics and STIFF-FLOP, Aer-O-Scope [170] was another commercial colonoscope that enable robotic surgery with safe interaction. Aer-O-Scope relies on an effective locomotion by double balloon propulsion mechanism. These kinds of newly emerging flexible robotic technology prove the viability of soft robotic endoscopic surgery. In the future, the inexpensive 3D printed soft robotic system in this research can be potentially applied to other regions of human body for image-guided intervention via natural orifice, such as upper gastrointestinal tract.

Reference

[1]   Yeh, D.H., Tam, S., Fung, K., MacNeil, S. D., Yoo, J., Winquist, E., Palma, D. A., and Nichols, A. C., *Transoral robotic surgery vs. radiotherapy for management of oropharyngeal squamous cell carcinoma - A systematic review of the literature.* **European Journal of Surgical Oncology**, 2015. 41(12): p. 1603-14.

[2]   Collaborates, G.B.o.D.S., *Global, regional, and national incidence, prevalence, and years lived with disability for 301 acute and chronic diseases and injuries in 188 countries, 1990–2013: a systematic analysis for the Global Burden of Disease Study 2013.* **The Lancet**, 2015. 386(9995): p. 743-800.

[3]   R. J. Sanderson, a.J.A.D.I., *Squamous cell carcinomas of the head and neck.* **British Medical Journal (BMJ)**, 2002.

[4]   Fund, H.K.C. *10 Most Common Cancers in Hong Kong*. 2014   [cited 2016 19 DEC].

[5]   Nisa, L., von Buren, T., Tiab, A., and Giger, R., *Giant plexiform schwannoma of the tongue.* **Case Reports in Otolaryngology**, 2011. 2011: p. 762524.

[6]   Ferlay, J., Soerjomataram, I., Dikshit, R., Eser, S., Mathers, C., Rebelo, M., Parkin, D. M., Forman, D., and Bray, F., *Cancer incidence and mortality worldwide: sources, methods and major patterns in GLOBOCAN 2012.* **International Journal of Cancer**, 2015. 136(5): p. E359-86.

[7]   Ferlay J, S.I., Ervik M, *GLOBOCAN 2012 cancer incidence and mortality worldwide: IARC cancer base No. 11.* **International Agency for Research on Cancer (IARC)**, 2013.

[8]   Frederic Lam, a.M.E., *Data visualization tools that present current national estimates of cancer incidence, mortality, and prevalence.* **International Agency for Research on Cancer (IARC)**, 2012.

[9]   Torre, L.A., Bray, F., Siegel, R. L., Ferlay, J., Lortet-Tieulent, J., and Jemal, A., *Global cancer statistics, 2012.* **Cancer Journal for Clinicians (CA Cancer J Clin)**, 2015. 65(2): p. 87-108.

[10]   Joshi, P., Dutta, S., Chaturvedi, P., and Nair, S., *Head and neck cancers in developing countries.* **Rambam Maimonides Med J**, 2014. 5(2): p. e0009.

[11]   Simard, E.P., Torre, L. A., and Jemal, A., *International trends in head and neck cancer incidence rates: differences by country, sex, and anatomic site.* **Oral Oncology**, 2014. 50(5): p. 387-403.

[12]   Wayne M. Koch MD, M.L.M., Duane Sewell MD, Marianna Zahurak MA, and David Sidransky MD, *Head and neck cancer in nonsmokers a distinct clinical and molecular entity.* **Laryngoscope**, 1999.

[13]   Hashibe, M., Brennan, P., Chuang, S. C., Boccia, S., Castellsague, X., Chen, C., Curado, M. P., Dal Maso, L., Daudt, A. W., Fabianova, E., et al., *Interaction between tobacco and alcohol use and the risk of head and neck cancer: pooled analysis in the International Head and Neck Cancer Epidemiology Consortium.* **Cancer Epidemiol Biomarkers Prev**, 2009. 18(2): p. 541-50.

[14]   William J. Blot, J.K.M., Deborah M. Winn, Donald F. Austin, Raymond S. Greenberg, Susan Preston-Martin, Leslie Bernstein, Janet B. Schoenberg, Annette Stemhagen, and Joseph F. Fraumeni, Jr., *Smoking and drinking in relation to oral and pharyngeal cancer.* **Cancer Research**, 1988.

[15]   Priebe, S.L., Aleksejūniene, Jolanta, Dharamsi, Shafik, Zed, and Christopher, *Oral cancer and*

cultural factors in Asia. **Canadian Journal of Dental Hygiene**, 2008. 42(6): p. 289-293.

[16]   Chang, E.T., and Adami, H. O., *The enigmatic epidemiology of nasopharyngeal carcinoma.* **Cancer Epidemiol Biomarkers Prev**, 2006. 15(10): p. 1765-77.

[17]   Bonilla-Velez, J., Mroz, E. A., Hammon, R. J., and Rocco, J. W., *Impact of human papillomavirus on oropharyngeal cancer biology and response to therapy: implications for treatment.* **Otolaryngologic Clinics of North America**, 2013. 46(4): p. 521-43.

[18]   Attner, P., Du, J., Nasman, A., Hammarstedt, L., Ramqvist, T., Lindholm, J., Marklund, L., Dalianis, T., and Munck-Wikland, E., *The role of human papillomavirus in the increased incidence of base of tongue cancer.* **International Journal of Cancer**, 2010. 126(12): p. 2879-84.

[19]   Smith, E.M., Ritchie, J. M., Summersgill, K. F., Klussmann, J. P., Lee, J. H., Wang, D., Haugen, T. H., and Turek, L. P., *Age, sexual behavior and human papillomavirus infection in oral cavity and oropharyngeal cancers.* **International Journal of Cancer**, 2004. 108(5): p. 766-72.

[20]   Arens, C., *Transoral treatment strategies for head and neck tumors.* **GMS Current Topics in Otorhinolaryngology - Head and Neck Surgery**, 2012.

[21]   Whang, S.N., Filippova, M., and Duerksen-Hughes, P., *Recent Progress in Therapeutic Treatments and Screening Strategies for the Prevention and Treatment of HPV-Associated Head and Neck Cancer.* **Viruses**, 2015. 7(9): p. 5040-65.

[22]   McGurk, M., and Goodger, N. M., *Head and neck cancer and its treatment: historical review.* **British Journal of Oral and Maxillofacial Surgery**, 2000. 38(3): p. 209-20.

[23]   Fenn, J.E., and Udelsman, R., *First use of intravenous chemotherapy cancer treatment: rectifying the record.* **Journal of the American College of Surgeons**, 2011. 212(3): p. 413-7.

[24]   Joensuu, H., *Systemic chemotherapy for cancer: from weapon to treatment.* **The Lancet Oncology**, 2008. 9(3): p. 304.

[25]   Mydlarz, W.K., Chan, J. Y., and Richmon, J. D., *The role of surgery for HPV-associated head and neck cancer.* **Oral Oncology**, 2015. 51(4): p. 305-13.

[26]   Arlene A. Forastiere, a.A.T., *Radiotherapy and concurrent chemotherapy a strategy that improves locoregional control and survival in oropharyngeal cancer.* **Journal of the National Cancer Institute**, 1999.

[27]   Bussink, J., van der Kogel, Albert J., Kaanders, and Johannes H. A. M., *Activation of the PI3-K/AKT pathway and implications for radioresistance mechanisms in head and neck cancer.* **The Lancet Oncology**, 2008. 9(3): p. 288-296.

[28]   Arthur W. Wu, S.K.B., Chi Lai, Mysore S. Veena, Marilene B. Wang, and Eri S. Srivatsan, *Abstract 3316: CD44High head and neck cancer cells demonstrate increased cell growth and chemotherapeutic resistance.* **Cancer Research**, 2010.

[29]   Ajani, J.A., Izzo, J. G., and Lee, J. S., *Chemotherapy and radiotherapy resistance: complexity, reality, and promise.* **Journal of Clinical Oncology**, 2009. 27(1): p. 162-3, author reply 163.

[30]   Chen, A.Y., Zhu, J., and Fedewa, S., *Temporal trends in oropharyngeal cancer treatment and survival: 1998-2009.* **Laryngoscope**, 2014. 124(1): p. 131-8.

[31] Takes, R.P., Strojan, P., Silver, C. E., Bradley, P. J., Haigentz, M., Jr., Wolf, G. T., Shaha, A. R., Hartl, D. M., Olofsson, J., Langendijk, J. A., Rinaldo, A., and Ferlito, A., *Current trends in initial management of hypopharyngeal cancer: the declining use of open surgery.* **Head and Neck**, 2012. 34(2): p. 270-81.

[32] GEORGE CRILE, M.D., *Excision of cancer of the head and neck.* 1906.

[33] George Crile, M.D., and Cleveland, O., *Excision of cancer of the head and neck with special reference to the plan of dissection Based on one hundred and thirty two operations.* **Landmark Article**, 1906.

[34] Rubinstein, M., and Armstrong, W. B., *Transoral laser microsurgery for laryngeal cancer: a primer and review of laser dosimetry.* **Lasers in Medical Science**, 2011. 26(1): p. 113-24.

[35] Ambrosch, P., *The role of laser microsurgery in the treatment of laryngeal cancer.* **Current Opinion in Otolaryngology & Head and Neck Surgery**, 2007: p. 82-88.

[36] Haughey, B.H., Hinni, M. L., Salassa, J. R., Hayden, R. E., Grant, D. G., Rich, J. T., Milov, S., Lewis, J. S., Jr., and Krishna, M., *Transoral laser microsurgery as primary treatment for advanced-stage oropharyngeal cancer: a United States multicenter study.* **Head and Neck**, 2011. 33(12): p. 1683-94.

[37] Michael L. Hinni, M., John R. Salassa, MD, David G. Grant, MD, Bruce W. Pearson, MD, Richard E. Hayden, MD, Alexios Martin, MD, Hans Christiansen, MD, Bruce H. Haughey, MD, Brian Nussenbaum, MD, and Wolfgang Steiner, MD, *Transoral Laser Microsurgery for Advanced Laryngeal Cancer.* **Arch Otolaryngol Head Neck Surgery**, 2007.

[38] Mohamed, N.N., et al., *Comparison between laser- and diathermy-assisted posterior cordotomy for bilateral vocal cord abductor paralysis.* **JAMA Otolaryngol Head Neck Surg**, 2013. 139(9): p. 923-30.

[39] Kebes. *Electromagnetic absorption by water.* 2008 [cited 2017 24 Jan].

[40] Li, R.J., and Richmon, J. D., *Transoral endoscopic surgery: new surgical techniques for oropharyngeal cancer.* **Otolaryngologic Clinics of North America**, 2012. 45(4): p. 823-44.

[41] Solares, C.A., and Strome, M., *Transoral robot-assisted CO2 laser supraglottic laryngectomy: experimental and clinical data.* **Laryngoscope**, 2007. 117(5): p. 817-20.

[42] Koufman, J.A., Rees, C. J., Frazier, W. D., Kilpatrick, L. A., Wright, S. C., Halum, S. L., and Postma, G. N., *Office-based laryngeal laser surgery: a review of 443 cases using three wavelengths.* **Otolaryngol Head and Neck Surgery**, 2007. 137(1): p. 146-51.

[43] Karsten Scholle, S.L., Philipp Koopmann, and Peter Fuhrberg, *2 μm Laser Sources and Their Possible Applications.* **Frontiers in Guided Wave Optics and Optoelectronics**. 2010.

[44] Kathryn M. Van Abel, M., Eric J. Moore, MD, Matthew L. Carlson,MD, Jennifer A. Davidson, PA, Joaquin J. Garcia, MD, Steven M. Olsen, MD, and Kerry D. Olsen, MD, *Transoral Robotic Surgery Using the ThuliumYAG Laser A Prospective Study.* **Arch Otolaryngol Head Neck Surgery**, 2012.

[45] Johan Fagan, a.W.S., *Transoral CO2 laser microsurgery (TLM) for cancer and other pathology of the upper aerodigestive tract.* **Otolaryngology, Head & Neck Operative Surgery**, 2013.

[46]   Wei, W.I., and Ho, W. K., *Transoral robotic resection of recurrent nasopharyngeal carcinoma.* **Laryngoscope**, 2010. 120(10): p. 2011-4.

[47]   Chan, J.Y., Tsang, R. K., Eisele, D. W., and Richmon, J. D., *Transoral robotic surgery of the parapharyngeal space: a case series and systematic review.* **Head and Neck**, 2015. 37(2): p. 293-8.

[48]   Bekeny, J.R., and Ozer, Enver, *Transoral robotic surgery frontiers.* **World Journal of Otorhinolaryngology-Head and Neck Surgery**, 2016. 2(2): p. 130-135.

[49]   Lang, S., Mattheis, S., Hasskamp, P., Lawson, G., Guldner, C., Mandapathil, M., Schuler, P., Hoffmann, T., Scheithauer, M., and Remacle, M., *A European multicenter study evaluating the flex robotic system in transoral robotic surgery.* **Laryngoscope**, 2016.

[50]   Tsang, R.K., and Holsinger, F. C., *Transoral endoscopic nasopharyngectomy with a flexible next-generation robotic surgical system.* **Laryngoscope**, 2016. 126(10): p. 2257-62.

[51]   Mattheis, S., Hasskamp, P., Holtmann, L., Schafer, C., Geisthoff, U., Dominas, N., and Lang, S., *Flex Robotic System in transoral robotic surgery: The first 40 patients.* **Head and Neck**, 2016.

[52]   Olivier Clatz, H.e.D., Ion-Florin Talos, Alexandra J. Golby, Nicholas Ayache, Ron Kikinis, Ferenc A. Jolesz and Simon K. Warfield, *Robust Nonrigid Registration to Capture Brain Shift from Intraoperative MRI.* **Intraoperative MRI**, 2004.

[53]   Olson, S.M., Hussaini, M., and Lewis, J. S., Jr., *Frozen section analysis of margins for head and neck tumor resections: reduction of sampling errors with a third histologic level.* **Mod Pathol**, 2011. 24(5): p. 665-70.

[54]   Fichera, L., Pardo, D., Illiano, P., Ortiz, J., Caldwell, D. G., and Mattos, L. S., *Online estimation of laser incision depth for transoral microsurgery: approach and preliminary evaluation.* **The International Journal of Medical Robotics**, 2016. 12(1): p. 53-61.

[55]   Zhu, M., Z. Sun, and C.K. Ng, *Image-guided thermal ablation with MR-based thermometry.* **Quant Imaging Med Surg**, 2017. 7(3): p. 356-368.

[56]   Rieke, V., and Butts Pauly, K., *MR thermometry.* **J Magn Reson Imaging**, 2008. 27(2): p. 376-90.

[57]   Holbrook, A.B., et al., *Real-time MR thermometry for monitoring HIFU ablations of the liver.* **Magn Reson Med**, 2010. 63(2): p. 365-73.

[58]   PARKER, D.L., *Applications of NMR imaging in hyperthermia an evaluation of the potential for localized tissue heating and noninvasive temperature monitoring.* **IEEE TRANSACTIONS ON BIOMEDICAL ENGINEERING**, 1984. BME-31(1).

[59]   Simon J. Graham, M.J.B., R. Mark Henkelman *Time and temperature dependence of MR parameters during thermal coagulation of ex vivo rabbit muscle.* **Magnetic Resonance in Medicine**, 1998.

[60]   T.R. NELSON, S.M.T., *Temperature dependence of proton relaxation times in vitro.* **Magnetic Resonance Imaging**, 1987.

[61]   Ludemann, L., et al., *Non-invasive magnetic resonance thermography during regional hyperthermia.* **Int J Hyperthermia**, 2010. 26(3): p. 273-82.

[62]   Simpson JH, C.H., *Diffusion and nuclear spin relaxation in water.* **Phys. Rev.**, 1958.

[63]   STEVEN D. WOLFF, R.S.B., *Magnetization transfer contrast (MTC) and tissue water proton*

relaxation in vivo. **Magnetic Resonance in Medicine**, 1989.

[64]   Iain R. Young, J.W.H., Angela Oatridge, Michael V. Prior *Modeling and observation of temperature changes in Vivo using MRI.* **Magnetic Resonance in Medicine**, 1994.

[65]   Abragam, A. and L.C. Hebel, *The Principles of Nuclear Magnetism.* **American Journal of Physics**, 1961. 29(12): p. 860-861.

[66]   John De Poorter, C.D.W., Yves De Deene, Carsten Thomsen, Freddy Stahlberg, Eric Achten, *Noninvasive MRI thermometry with the proton resonance frequency (PRF) method in vivo results in human muscle.* **Magnetic Resonance in Medicine**, 1995.

[67]   Poorter, J.D., *Noninvasive MRI thermometry with the proton resonance frequency method Study of susceptibility effects.* **Magnetic Resonance in Medicine**, 1995.

[68]   Mohammadi, A.M. and J.L. Schroeder, *Laser interstitial thermal therapy in treatment of brain tumors--the NeuroBlate System.* **Expert Rev Med Devices**, 2014. 11(2): p. 109-19.

[69]   Shellock FG, C.J., *MR Safety and the American College of Radiology White Paper.* **American Journal of Roentgenology**, 2002: p. 178:1349-1352.

[70]   International, A.S.f.T.a.M.A., *ASTM F2503 - 05 Standard Practice for Marking Medical Devices and Other Items for Safety in the Magnetic Resonance Environment.* **ASTM International, West Conshohocken, PA**, 2005.

[71]   ROGER GASSERT, E.B., KIYOYUKI CHINZEI, *MRI-Compatible Robotics.* **IEEE ENGINEERING IN MEDICINE AND BIOLOGY MAGAZINE**, 2008.

[72]   Association, N.E.M., *Determination of Signal-to-Noise Ratio (SNR) in Diagnostic Magnetic Resonance Imaging*, in **NEMA Standards Publication MS 1**. 2008.

[73]   Remacle, M., Matar, N., Lawson, G., and Bachy, V., *Laryngeal advanced retractor system: a new retractor for transoral robotic surgery.* **Otolaryngol Head and Neck Surgery**, 2011. 145(4): p. 694-6.

[74]   Wippold, F.J., 2nd, *Head and neck imaging: the role of CT and MRI.* **J Magn Reson Imaging**, 2007. 25(3): p. 453-65.

[75]   Bach, T., Muschter, R., Sroka, R., Gravas, S., Skolarikos, A., Herrmann, T. R., Bayer, T., Knoll, T., Abbou, C. C., Janetschek, G., Bachmann, A., and Rassweiler, J. J., *Laser treatment of benign prostatic obstruction: basics and physical differences.* **European Urology**, 2012. 61(2): p. 317-25.

[76]   Bryce Samson, G.O., Adrian Carter, and Steven R. Bowman. *Optical Fiber Fabrication: Holmium-doped silica fiber designs extend fiber lasers beyond 2 μm*. 2012.

[77]   Simakov, N., Hemming, A., Clarkson, W. A., Haub, J., and Carter, A., *A cladding-pumped, tunable holmium doped fiber laser.* **Optics Express**, 2013. 21(23): p. 28415-22.

[78]   A ZENDEHNAM, M.M., A FARASHIANI, and L HORABADI FARAHANI, *Investigation of bending loss in a single-mode optical fibre.* **Indian Academy of Sciences**, 2010.

[79]   Li, Y., *Impact of Macrobend Loss on the Bandwidth of Standard and Bend-Optimized Multimode Fibers.* 2009.

[80]   Christopher R. Wilson, L.A.H., Joshua D. Kennedy, Pierce B. Irby, and Nathaniel M. Fried,

Miniature ball-tip optical fibers for use in thulium fiber laser ablation of kidney stones. **Journal of Biomedical Optics**, 2016.

[81]   Naoyo Nishida, H.Y., Takashi Nishida, Toshiharu Kamura, and Masamichi Kojiro, *Angiogenesis in cancer.* **Vascular Health and Risk Management**, 2006.

[82]   Dionysopoulos, D., Tolidis, Kosmas, Strakas, Dimitrios, Gerasimou, Paris, Sfeikos, Thrasyvoulos, and Gutknecht, Norbert, *Effects of blue diode laser (445 nm) and LED (430–480 nm) radiant heat treatments on dental glass ionomer restoratives.* **Optics & Laser Technology**, 2018. 99: p. 249-255.

[83]   Jordan P. Farkas, M., John E. Hoopman, CLMSO, and Jeffrey M. Kenkel, MD, *Five Parameters You Must Understand to Master Control of Your Laser Light-Based Devices.* **Aesthetic Surgery Journal**, 2013.

[84]   Hao Su, D.C.C., Weijian Shang, Alexander Camilo, Gregory A. Cole, D. Caleb Rucker, Robert J. Webster, and Gregory S. Fischer, *A MRI-guided concentric tube continuum robot with piezoelectric actuation A feasibility study.* **IEEE International Conference on Robotics and Automation**, 2012.

[85]   Lee, D.-Y., Kim, Jongwoo, Kim, Ji-Suk, Baek, Changyeob, Noh, Gunwoo, Kim, Do-Nyun, Kim, Keri, Kang, Sungchul, and Cho, Kyu-Jin, *Anisotropic Patterning to Reduce Instability of Concentric-Tube Robots.* **IEEE Transactions on Robotics**, 2015. 31(6): p. 1311-1323.

[86]   Su, H., Li, G., Rucker, D. C., Webster Iii, R. J., and Fischer, G. S., *A Concentric Tube Continuum Robot with Piezoelectric Actuation for MRI-Guided Closed-Loop Targeting.* **Annals of Biomedical Engineering**, 2016. 44(10): p. 2863-2873.

[87]   Vogel, V., *Soft robotics: Bionic jellyfish.* **Nat Mater**, 2012. 11(10): p. 841-2.

[88]   Gerhart, G.R., Walker, Ian D., Shoemaker, Charles M., Dawson, Darren M., Flash, Tamar, Gage, Douglas W., Grasso, Frank W., Hanlon, Roger T., Hochner, Binyamin, Kier, William M., Pagano, Christopher C., Rahn, Christopher D., and Zhang, Qiming M., *Continuum robot arms inspired by cephalopods.* **Proceedings of the SPIE**, 2005. 5804: p. 303-314.

[89]   Renda, F., Giorelli, Michele, Calisti, Marcello, Cianchetti, Matteo, and Laschi, Cecilia, *Dynamic Model of a Multibending Soft Robot Arm Driven by Cables.* **IEEE Transactions on Robotics**, 2014. 30(5): p. 1109-1122.

[90]   Nakajima, K., Hauser, H., Kang, R., Guglielmino, E., Caldwell, D. G., and Pfeifer, R., *A soft body as a reservoir: case studies in a dynamic model of octopus-inspired soft robotic arm.* **Front Comput Neurosci**, 2013. 7: p. 91.

[91]   Trivedi, D., et al., *Soft robotics: Biological inspiration, state of the art, and future research.* **Applied Bionics and Biomechanics**, 2008. 5(3): p. 99-117.

[92]   Mao, S., Dong, Erbao, Jin, Hu, Xu, Min, Zhang, Shiwu, Yang, Jie, Low, and Kin Huat, *Gait Study and Pattern Generation of a Starfish-Like Soft Robot with Flexible Rays Actuated by SMAs.* **Journal of Bionic Engineering**, 2014. 11(3): p. 400-411.

[93]   Sareh, S., et al. *Bio-inspired tactile sensor sleeve for surgical soft manipulators.* in *IEEE International Conference on Robotics and Automation (ICRA)*. 2014. IEEE.

[94]   S. Sareh, A.J., A. Faragasso, Y. Noh, T. Nanayakkara, P. Dasgupta, L.D. Seneviratne, H.A.

Wurdemann, and K. Althoefer, *Bio-Inspired Tactile Sensor Sleeve for Surgical Soft Manipulators.* **IEEE International Conference on Robotics and Automation (ICRA)**, 2014.

[95]   Maghooa, F., et al. *Tendon and pressure actuation for a bio-inspired manipulator based on an antagonistic principle.* in **IEEE International Conference on Robotics and Automation (ICRA)**. 2015. IEEE.

[96]   Cianchetti, M., Ranzani, Tommaso, Gerboni, Giada, Nanayakkara, Thrishantha, Althoefer, Kaspar, Dasgupta, Prokar, and Menciassi, Arianna, *Soft Robotics Technologies to Address Shortcomings in Today's Minimally Invasive Surgery: The STIFF-FLOP Approach.* **Soft Robotics**, 2014. 1(2): p. 122-131.

[97]   Farahnaz Maghooa, A.S., Yohan Noh, Kaspar Althoefer, and Helge A Wurdemann, *Tendon and pressure actuation for a bio inspired manipulator based on an antagonistic principle.* **IEEE International Conference on Robotics and Automation (ICRA)**, 2015.

[98]   Renevier, R., Tamadazte, Brahim, Rabenorosoa, Kanty, Tavernier, Laurent, and Andreff, Nicolas, *Endoscopic Laser Surgery: Design, Modeling, and Control.* **IEEE/ASME Transactions on Mechatronics**, 2017. 22(1): p. 99-106.

[99]   Shepherd, R.F., Stokes, Adam A., Freake, Jacob, Barber, Jabulani, Snyder, Phillip W., Mazzeo, Aaron D., Cademartiri, Ludovico, Morin, Stephen A., and Whitesides, George M., *Using Explosions to Power a Soft Robot.* **Angewandte Chemie**, 2013. 125(10): p. 2964-2968.

[100]   De Volder, M., Moers, A. J. M., and Reynaerts, D., *Fabrication and control of miniature McKibben actuators.* **Sensors and Actuators A: Physical**, 2011. 166(1): p. 111-116.

[101]   Ainla, A., et al., *Soft, Rotating Pneumatic Actuator.* **Soft Robot**, 2017. 4(3): p. 297-304.

[102]   Yi Sun, Y.S.S., and Jamie Paik, *Characterization of silicone rubber based soft pneumatic actuators.* **IEEE/RSJ International Conference on Intelligent Robots and Systems (IROS)**, 2013.

[103]   Paez, L., G. Agarwal, and J. Paik, *Design and Analysis of a Soft Pneumatic Actuator with Origami Shell Reinforcement.* **Soft Robotics**, 2016. 3(3): p. 109-119.

[104]   Wang, Z., Polygerinos, Panagiotis, Overvelde, Johannes, Galloway, Kevin, Bertoldi, Katia, and Walsh, Conor, *Interaction Forces of Soft Fiber Reinforced Bending Actuators.* **IEEE/ASME Transactions on Mechatronics**, 2016: p. 1-1.

[105]   Kevin C. Galloway, P.P., Conor J. Walsh, and Robert J. Wood, *Mechanically Programmable Bend Radius for Fiber-Reinforced Soft Actuators.* **16th International Conference on Advanced Robotics (ICAR)**, 2013.

[106]   Joshua Bishop-Moser, G.K., Charles Kim, and Sridhar Kota, *Design of Soft Robotic Actuators using Fluid-filled Fiber-Reinforced.* **IEEE/RSJ International Conference on Intelligent Robots and Systems**, 2012.

[107]   Ramses V. Martinez, C.R.F., Xin Chen, and George M. Whitesides, *Elastomeric origami Programmable paper-elastomer composites as pneumatic actuators.* **Advanced Functional Material**, 2012.

[108]   Nadia G. Cheng, M.B.L., Steven J. Keating, Adam M. Setapen, Katy I. Gero, Anette E. Hosoi, and

Karl D. Iagnemma, *Design and Analysis of a Robust, Low-cost, Highly Articulated Manipulator Enabled by Jamming of Granular Media.* **Robotics and Automation (ICRA), 2012 IEEE International Conference on**, 2012.

[109]   Brown, E., Rodenberg, N., Amend, J., Mozeika, A., Steltz, E., Zakin, M. R., Lipson, H., and Jaeger, H. M., *Universal robotic gripper based on the jamming of granular material.* **Proceedings of the National Academy of Sciences**, 2010. 107(44): p. 18809-18814.

[110]   A. Sadeghi, L.B., and B. Mazzolai,, *Innovative Soft Robots Based on Electro-Rheological Fluids.* **IEEE/RSJ International Conference on Intelligent Robots and Systems**, 2012.

[111]   Jun Shintake, B.S., Samuel Rosset, Herbert Shea, and Dario Floreano, *Variable Stiffness Actuator for Soft Robotics Using Dielectric Elastomer and Low-Melting-Point Alloy Soft state.* **IEEE/RSJ International Conference on Intelligent Robots and Systems (IROS)**, 2015.

[112]   Martinez, R.V., Branch, J. L., Fish, C. R., Jin, L., Shepherd, R. F., Nunes, R. M., Suo, Z., and Whitesides, G. M., *Robotic tentacles with three-dimensional mobility based on flexible elastomers.* **Advanced Materials**, 2013. 25(2): p. 205-12.

[113]   Mosadegh, B., Polygerinos, Panagiotis, Keplinger, Christoph, Wennstedt, Sophia, Shepherd, Robert F., Gupta, Unmukt, Shim, Jongmin, Bertoldi, Katia, Walsh, Conor J., and Whitesides, George M., *Pneumatic Networks for Soft Robotics that Actuate Rapidly.* **Advanced Functional Materials**, 2014. 24(15): p. 2163-2170.

[114]   Majidi, C., and Wood, Robert J., *Tunable elastic stiffness with microconfined magnetorheological domains at low magnetic field.* **Applied Physics Letters**, 2010. 97(16): p. 164104.

[115]   E. Steltz, A.M., N. Rodenberg, E. Brown, and H.M. Jaeger, *JSEL Jamming Skin Enabled Locomotion.* **IEEE/RSJ International Conference on Intelligent Robots and Systems**, 2009.

[116]   Ranzani, T., Cianchetti, Matteo, Gerboni, Giada, Falco, Iris De, and Menciassi, Arianna, *A Soft Modular Manipulator for Minimally Invasive Surgery: Design and Characterization of a Single Module.* **IEEE Transactions on Robotics**, 2016. 32(1): p. 187-200.

[117]   Noh, Y., Bimbo, J., Sareh, S., Wurdemann, H., Fras, J., Chathuranga, D. S., Liu, H., Housden, J., Althoefer, K., and Rhode, K., *Multi-Axis Force/Torque Sensor Based on Simply-Supported Beam and Optoelectronics.* **Sensors (Basel)**, 2016. 16(11).

[118]   J. Fra´s, J.C., M. Macia´s, J. Główka, M. Cianchetti, and A. Menciassi, *New STIFF-FLOP module construction idea for improved actuation and sensing.* **IEEE International Conference on Robotics and Automation (ICRA)**, 2015.

[119]   Gerboni, G., Ranzani, Tommaso, Diodato, Alessandro, Ciuti, Gastone, Cianchetti, Matteo, and Menciassi, Arianna, *Modular soft mechatronic manipulator for minimally invasive surgery (MIS): overall architecture and development of a fully integrated soft module.* **Meccanica**, 2015. 50(11): p. 2865-2878.

[120]   Shuichi Wakimoto, I.K., and Koichi Suzumori, *Development of large Intestine Endoscope Changing Its Stiffness.* **IEEE International Conference on Robotics and Biomimetics**, 2009.

[121]   Felice Cosentino, E.T., Giovanni Rubis Passoni, Elisabetta Morandi, and Alfonso Capria, *Functional*

evaluation of the Endotics System, a new disposable self-propelled robotic colonoscope in vitro tests and clinical trial. **The International Journal of Artificial Organs**, 2009.

[122] Tumino, E., *Endotics system vs colonoscopy for the detection of polyps.* **World Journal of Gastroenterology**, 2010. 16(43): p. 5452.

[123] Faudzi, A.A.M., et al. *Development of bending soft actuator with different braided angles*. in *IEEE/ASME International Conference on Advanced Intelligent Mechatronics*. 2012. IEEE.

[124] Suzumori, K., S. Iikura, and H. Tanaka. *Development of flexible microactuator and its applications to robotic mechanisms*. in *The 1991 IEEE International Conference on Robotics and Automation*. 1991.

[125] Koichi Suzumori, T.M., Hiroshi Watanabe, and Toshiaki Hisada, *Fiberless Flexible Microactuator Designed by Finite-Element Method.* **IEEE/ASME TRANSACTIONS ON MECHATRONICS**, 1997.

[126] Moseley, P., Florez, Juan Manuel, Sonar, Harshal Arun, Agarwal, Gunjan, Curtin, William, and Paik, Jamie, *Modeling, Design, and Development of Soft Pneumatic Actuators with Finite Element Method* **Advanced Engineering Materials**, 2016. 18(6): p. 978-988.

[127] Elsayed, Y., Vincensi, Augusto, Lekakou, Constantina, Geng, Tao, Saaj, C. M., Ranzani, Tommaso, Cianchetti, Matteo, and Menciassi, Arianna, *Finite Element Analysis and Design Optimization of a Pneumatically Actuating Silicone Module for Robotic Surgery Applications.* **Soft Robotics**, 2014. 1(4): p. 255-262.

[128] P. A. L. S. Martins, R.M.N.J., and A. J. M. Ferreira, *A comparative study of several material models for prediction of hyperelastic properties Application to Silicone-Rubber and Soft Tissues.* **Strain**, 2012.

[129] Shahzad, M., Kamran, Ali, Siddiqui, Muhammad Zeeshan, and Farhan, Muhammad, *Mechanical Characterization and FE Modelling of a Hyperelastic Material.* **Materials Research**, 2015. 18(5): p. 918-924.

[130] de Rooij, R., Kuhl, and Ellen, *Constitutive Modeling of Brain Tissue: Current Perspectives.* **Applied Mechanics Reviews**, 2016. 68(1): p. 010801.

[131] Ranzani, T., Gerboni, G., Cianchetti, M., and Menciassi, A., *A bioinspired soft manipulator for minimally invasive surgery.* **Bioinspir Biomim**, 2015. 10(3): p. 035008.

[132] Jingjun Yu, K.W., Guanghua Zong, and Xianwen Kong, *A Comparative Study on Motion Characteristics of Three Two-Degree-of-Freedom Pointing Mechanisms.* **Journal of Mechanisms and Robotics Copyright VC**, 2016.

[133] Paolo Baerlocher, a.R.B., *Parametrization and range of motion of the ball-and-socket joint.* **Deformable avatars**, 2001.

[134] Ivlev, O., *Soft Fluidic Actuators of Rotary Type for Safe Physical Human-Machine Interaction.* **IEEE 11th International Conference on Rehabilitation Robotics**, 2009.

[135] Peele, B.N., Wallin, T. J., Zhao, H., and Shepherd, R. F., *3D printing antagonistic systems of artificial muscle using projection stereolithography.* **Bioinspir Biomim**, 2015. 10(5): p. 055003.

[136] Blanes, C., Mellado, Martín, and Beltran, Pablo, *Novel Additive Manufacturing Pneumatic Actuators and Mechanisms for Food Handling Grippers.* **Actuators**, 2014. 3(3): p. 205-225.

[137] Takuya Umedachi, V.V., and Barry A. Trimmer, *Highly deformable 3-D printed soft robot generating inching and crawling locomotions with variable friction legs.* **IEEE/RSJ International Conference on Intelligent Robots and Systems (IROS)**, 2013.

[138] *Standard Test Methods for Vulcanized Rubber and Thermoplastic Elastomers - Tension*, in **ASTM International**.

[139] Dong, Z., et al. *A Robotic Catheter System for MRI-guided Cardiac Electrophysiological Intervention.* in *ICRA 2016 Workshop on Compliant, Continuum, Cognitive, and Collaborative*. 2017. Singapore.

[140] John P. Whitney, M.F.G., Eric L. Brockmeyer, and Jessica K. Hodgins, *A Low-Friction Passive Fluid Transmission and Fluid-Tendon Soft Actuator.* **IEEE/RSJ International Conference on Intelligent Robots and Systems (IROS)**, 2014.

[141] John P. Whitney, T.C., John Mars3, Jessica K. Hodgins, *A hybrid hydrostatic transmission and human-safe haptic telepresence robot.* **IEEE International Conference on Robotics and Automation (ICRA)**, 2016.

[142] Natalie Burkhard, S.F., Alexander Gruebele, J. Peter Whitney, Roger Goldman, Bruce Daniel, Mark Cutkosky, *A rolling-diaphragm hydrostatic transmission for remote MR-guided needle insertion.* **IEEE International Conference on Robotics and Automation (ICRA)**, 2017.

[143] Lee, K.-H., et al., *MR Safe Robotic Manipulator for MRI-Guided Intracardiac Catheterization.* **IEEE/ASME Transactions on Mechatronics**, 2018. 23(2): p. 586-595.

[144] Z. Guo, T.L.T.L., Y. Chen, H. Su, D.T.M. Chan, and K. W. Kwok, *Novel design of an MR-safe pneumatic stepper motor for MRI-guided robotic interventions.* **Proceedings of The Hamlyn Symposium on Medical Robotics**, 2016: p. 50-51.

[145] Comber, D.B., E.J. Barth, and R.J. Webster, *Design and Control of an Magnetic Resonance Compatible Precision Pneumatic Active Cannula Robot.* **Journal of Medical Devices**, 2014. 8(1): p. 011003.

[146] Camarillo, D.B., et al., *Mechanics modeling of tendon-driven continuum manipulators.* **IEEE Transactions on Robotics**, 2008. 24(6): p. 1262-1273.

[147] Jones, B. and I.D. Walker, *Kinematics for multisection continuum robots.* **IEEE Transactions on Robotics**, 2006. 22(1): p. 43-55.

[148] Mahvash, M. and P.E. Dupont, *Stiffness control of surgical continuum manipulators.* **IEEE Transactions on Robotics**, 2011. 27(2): p. 334-345.

[149] Webster III, R.J. and B.A. Jones, *Design and kinematic modeling of constant curvature continuum robots: A review.* **The International Journal of Robotics Research**, 2010.

[150] Ganji, Y. and F. Janabi-Sharifi, *Catheter kinematics for intracardiac navigation.* **IEEE Transactions on Biomedical Engineering**, 2009. 56(3): p. 621-632.

[151] Jones, B.A. and I.D. Walker. *A New Approach to Jacobian Formulation for a Class of Multi-Section Continuum Robots*. in *IEEE International Conference on Robotics and Automation (ICRA)*. 2005.

[152]   Webster III, R.J., et al., *Closed-form differential kinematics for concentric-tube continuum robots with application to visual servoing.* **Experimental Robotics: The Eleventh International Symposium**, 2009: p. 485-494.

[153]   Neppalli, S., et al., *Closed-form inverse kinematics for continuum manipulators.* **Advanced Robotics**, 2009. 23(15): p. 2077-2091.

[154]   Marchese, A.D., et al., *Design and control of a soft and continuously deformable 2d robotic manipulation system*, in **The IEEE International Conference on Robotics and Automation**. 2014. p. 2189-2196.

[155]   Marchese, A.D., R. Tedrake, and D. Rus, *Dynamics and trajectory optimization for a soft spatial fluidic elastomer manipulator.* **The International Journal of Robotics Research**, 2016. 35(8): p. 1000-1019.

[156]   Wang, H., et al., *Visual servo control of cable-driven soft robotic manipulator*, in **The 2013 IEEE/RSJ International Conference on Intelligent Robots and Systems**. 2013. p. 57-62.

[157]   Chirikjian, G.S., *Hyper-redundant manipulator dynamics: A continuum approximation.* **J. Adv. Robot**, 1995. 9(3): p. 217-243.

[158]   Kang, R., et al., *Design, modeling and control of a pneumatically actuated manipulator inspired by biological continuum structures.* **Bioinspiraton& Biomimetics**, 2013. 8: p. 036008.

[159]   Yekutieli, Y., et al., *Dynamic model of the octopus arm. I. biomechanics of the octopus reaching movement.* **J. Neurophysiol**, 2005. 94(2): p. 1443-1458.

[160]   Giorelli, M., et al., *A two dimensional inverse kinetics model of a cable driven manipulator inspired by the octopus arm*, in **the 2012 IEEE International Conference on Robotics and Automous Systems**. 2012. p. 3819-3824.

[161]   Renda, F., et al., *Dynamic model of a multibending soft robot arm driven by cables.* **IEEE Transactions on Robotics**, 2014. 30(5): p. 1109-1122.

[162]   Nguyen-Tuong, D. and J. Peters, *Model learning for robot control: a survey.* **Cognitive processing**, 2011. 12(4): p. 319-340.

[163]   Braganza, D., et al., *A neural network controller for continuum robots.* **Robotics, IEEE Transactions on**, 2007. 23(6): p. 1270-1277.

[164]   Giorelli, M., et al., *Neural Network and Jacobian Method for Solving the Inverse Statics of a Cable-Driven Soft Arm With Nonconstant Curvature.* **Robotics, IEEE Transactions on**, 2015. 31(4): p. 823-834.

[165]   Yip, M.C. and D.B. Camarillo, *Model-less feedback control of continuum manipulators in unknown environments.* **IEEE Trans. Robot**, 2014. 30(4): p. 880-889.

[166]   Michele Giorelli, F.R., Gabriele Ferri, and Cecilia Laschi, *A feed-forward neural network learning the inverse kinetics of a soft cable-driven manipulator moving in three-dimensional space.* **IEEE/RSJ International Conference on Intelligent Robots and Systems (IROS)**, 2013.

[167]   Thuruthel, T.G., Falotico, Egidio, Manti, Mariangela, and Laschi, Cecilia, *Stable Open Loop Control of Soft Robotic Manipulators.* **IEEE Robotics and Automation Letters**, 2018. 3(2): p. 1292-1298.

[168]   Neetu Punhani, G.R.D., Harsh Mahajan, M Jonathan Daniel, KV Chalapathi, and Abhishek Singh Nayyar, *Tumor size and its relation to cervical lymph node metastasis and its significance as a prognostic indicator for oral squamous cell carcinomas.* **Clinical Cancer Investigation Journal**, 2017.

[169]   Schaefers, G., *Testing MR safety and compatibility: an overview of the methods and current standards.* **IEEE Eng Med Biol Mag**, 2008. 27(3): p. 23-7.

[170]   Pfeffer, J., et al., *The Aer-O-Scope: proof of the concept of a pneumatic, skill-independent, self-propelling, self-navigating colonoscope in a pig model.* **Endoscopy**, 2006. 38(02): p. 144-148.